UNIVERSIDAD AUTÓNOMA DE MADRID
DEPARTAMENTO DE FÍSICA DE LA MATERIA CONDENSADA

Novel Contrast Agents for Multimodal Biomedical Imaging based in Nanotechnology

DANIEL CALLE HERNÁNDEZ

MADRID, 2014

UNIVERSIDAD AUTÓNOMA DE MADRID
DEPARTAMENTO DE FÍSICA DE LA MATERIA CONDENSADA

Novel Contrast Agents for Multimodal Biomedical Imaging based in Nanotechnology

DANIEL CALLE HERNÁNDEZ
Licenciado en Física

Directores

Prof. Paloma Ballesteros García
Prof. Sebastián Cerdán García-Esteller
Prof. Arisbel Cerpa Naranjo
Prof. Juan José Saenz

Tesis Doctoral realizada en el
Instituto de Investigaciones Biomédicas "Alberto Sols" CSIC/UAM

Esta tesis doctoral se ha realizado mediante un contrato predoctoral de la empresa SOLUTEX S.L. con el grupo del Prof. Sebastián Cerdán García-Esteller del Instituto de Investigaciones Biomédicas “Alberto Sols” CSIC/UAM, asociado al proyecto “Nuevos Agentes de contraste para imagen molecular por Resonancia Magnética en Oncología” en el periodo 2009-2013.

A mis padres y a mi hermano.
A Nuria.

Agradecimientos/Acknowledgements

Quiero comenzar agradeciendo al Prof. Sebastián Cerdán la confianza que depositó en mí cuando entré en su laboratorio y que ha permitido la realización de esta tesis doctoral. Durante esta etapa, Sebastián me ha guiado por los caminos de la ciencia, transmitiéndome sus amplios conocimientos para poder entender y trabajar en el mundo de la investigación. Ha sido un maestro excelente y es algo que no olvidaré. Igualmente, quiero agradecerle las continuas luchas por seguir manteniéndome contratado en su laboratorio en estos tiempos difíciles que estamos sufriendo. Por todo ello, mi más sentido agradecimiento Sebastián.

Esta tesis no habría podido realizarse sin el apoyo incondicional de la empresa Solutex S.L. Por eso, mi agradecimiento también a Fernando Moreno, presidente de Solutex, por haber confiado en nuestro laboratorio ofreciéndonos la posibilidad de colaborar con ellos en diversos proyectos científicos y haber apostado por la investigación básica. Quería agradecer también a Gerard Bannenberg el continuo apoyo científico que nos ha aportado en los diversos proyectos, a Iratxe Cano por su eficaz ayuda con las patentes y a todo el equipo de Solutex sin el cual esta tesis y las dos patentes que han surgido no hubieran sido posibles.

Agradecer también al Prof. Juan José Saenz por ofrecerse a codirigir esta tesis y por su ayuda en los diversos trámites que hemos tenido que realizar con el mundo académico. Igualmente, gracias también por ofrecernos a exponer nuestro trabajo en el congreso de nanotecnología TNT.

A la Prof. Paloma Ballesteros por ser la persona que me ha aportado los conocimientos en química necesarios en la investigación de los nanotubos. Gracias igualmente por haberme dado la oportunidad de realizar experimentos necesarios para mi tesis en su laboratorio de la Universidad Nacional de Educación a Distancia.

A la Prof. Arisbel Cerpa por aportarme ideas en el campo del magnetismo de los nanotubos así como ayudarme en la preparación de los nanotubos de carbono.

I also want to express my gratitude to Profs. Gaspare Varvaro and Elisabetta Agostinelli for accepting me in their laboratory in Rome and for the continuous effort in the investigation of the magnetic properties of Carbon Nanotubes.

Thanks also to Prof. Armagan Koçer to accepting me in her laboratory in Gronningen and for the knowledge of liposomes preparation that transmitted me during my stay in The Netherlands.
Quiero agradecer especialmente a Viviana Negri su ayuda con los nanotubos de carbono, ya que sin su trabajo no hubieran sido posibles ni la síntesis ni los análisis químicos necesarios en esta investigación, así como todo el apoyo químico ofrecido con los liposomas. Por esas horas empleadas juntos en intentar entender los resultados que teníamos delante, por todo ello, muchas gracias Vivi.
A Mariola Ramírez y Luisa Bausá del grupo de espectroscopia láser de la Universidad Autónoma de Madrid por haberme dado la oportunidad de realizar las medidas magnetoópticas en su laboratorio. Especialmente gracias a Luis Mateos por, además de ser un gran amigo, ayudarme con dichos experimentos.
También quiero agradecer a la profesora Pilar López Larrubia, por toda la ayuda tanto científica como personal que me ha ofrecido. Gracias por tus consejos y ayudas y por escucharme siempre que he acudido a ti.
A toda la gente del laboratorio de Sebastián Cerdán. Quiero agradecer especialmente a Patricia Sánchez su ayuda en el laboratorio desde el primer momento que empecé a trabajar en el IIB. Sin tu ayuda, Patri, habría estado totalmente perdido los primeros días en el laboratorio. Gracias igualmente por haberme enseñado las diversas técnicas necesarias para el trabajo con los animales. Un agradecimiento especial también para Blanca Lizarbe, por haberme puesto en contacto por primera vez con este laboratorio y así, poder haber realizado la tesis. Gracias también por tu ayuda con los distintos problemas a los que nos hemos enfrentado a lo largo de la tesis. Igualmente gracias a toda la gente que ha pasado por el laboratorio, Ania Benítez, Gerardo Arturo Peláez, Jesús Pacheco, Alexandra Borges, Tiago B. Rodrigues y Ana Belén Martín.
Quiero agradecer en particular al Servicio de Resonancia Magnética, SIERMAC, en especial a Teresa Navarro y María Rodríguez por toda la ayuda que me han brindado en las múltiples horas que he pasado en el laboratorio. Gracias por vuestra ayuda técnica y práctica que me habéis brindado durante todo este tiempo.
Al resto de gente con la que he compartido buenos momentos en el IIB y que han estado ahí cuando he necesitado su ayuda, en especial a Rocío Pérez, Ana Metelo, Miguel Martínez, Nuria Arias, Eva Cañadillas, Aire Salguero, Ana Amor, Cecilia Vieira y Santos Ángel de la Cuerda.

Mi agradecimiento también al personal del Instituto de Investigaciones Biomédicas “Alberto Sols”, al servicio de Tecnologías de la Información, al personal de animalario, al servicio de Imagen Multimodal Experimental, a Paco del servicio de Microscopía por Transmisión de Electrones de la Facultad de Medicina de la Universidad Autónoma, a Carlos Alfonso del CIB y al laboratorio de Síntesis Orgánica e Imagen Molecular por Resonancia Magnética de la UNED. Gracias especialmente a Javier Pérez del Servicio de Imagen Científica, el artista que ha plasmado en imágenes las ideas que a mí se me pasaban por la cabeza.

A todos mis amigos, la gente de Salamanca, los Fisikuchos (y la bandera), a la gente del Diego Álvaro y a todas las nuevas amistades surgidas en Madrid. Por aguantar mis explicaciones sobre mi trabajo aunque muchas veces os sonaran a chino.

A mis padres, Brigi y Joaquín, por haberme inculcado unos valores necesarios para afrontar esta vida y haberme dado la oportunidad de formarme académicamente todos estos años. A mi hermano Jorge, por haber estado ahí cuando te he necesitado y por todos los buenos momentos que hemos pasado juntos. Al resto de mi familia, por haberme animado siempre a seguir adelante en mis proyectos.

Y por último, pero no menos importante, muchas gracias Nuria, por haber estado apoyándome siempre que me surgía alguna dificultad, por aguantar y resolver todas las preguntas sobre biología que te he hecho, por todos esos momentos buenos que me has dado y me seguirás dando en el día a día, gracias.

Al escalar una gran montaña nadie deja
a un compañero para alcanzar la cima solo.
Tenzing

Summary

Clinical imaging modalities have reached a prominent role in medical diagnosis and patient management in the last decades. Different image methodologies as Positron Emission Tomography, Single Photon Emission Tomography, X Rays or Magnetic Resonance Imaging are in continuous evolution to satisfy the increasing demands of current medical diagnosis. Progress in these methodologies has been favored by the parallel development of increasingly powerful contrast agents. These are molecules that enhance the intrinsic contrast of the images in the regions where they accumulate, improving both sensitivity and specificity in the diagnosis. The contrast agent field is also evolving to improve the performance of these molecules using the novel approaches that modern Nanotechnology offers. In this thesis, I will describe novel generations of advanced contrast agents with multimodal imaging applications based in nanotechnology developments. Chapter 1 introduces the different imaging modalities used in clinic and the first generation of contrast agents used. Chapter 2 presents a systematic study and evaluation of a novel nanoparticulate contrast agent useful in Magnetic Resonance Imaging measurements of tumor perfusion and immune response. Chapter 3 describes the development of a new theragnostic composition based in liposomes containing both, a therapeutic molecule and an imaging biomarker. The efficacy of this new formulation is validated using different animal models of colonic inflammation and cancer and a variety of imaging techniques. Finally, in Chapter 4 I develop and implement a new anisotropic contrast agent for Magnetic Resonance Imaging based in the unusual magnetic properties of Carbon Nanotubes. I characterize their magnetic properties and their potential use as advanced anisotropic contrast agents. In summary, in this work I propose, develop and evaluate a second generation of nanoparticulate contrast agents and their potential applications in advanced multimodal imaging.

Resumen

Las distintas modalidades de Imagen Clínica han alcanzado una gran importancia en el diagnóstico médico y en el manejo clínico de los pacientes durante las últimas décadas. Las diferentes metodologías de imagen médica como Tomografía por Emisión de Positrones, Tomografía por Emisión de Fotón Único, Rayos X o Imagen por Resonancia Magnética han estado en continuo desarrollo para satisfacer la creciente demanda de diagnóstico médico. El progreso de estas metodologías se ha visto favorecido por el desarrollo en paralelo de agentes de contraste más potentes y eficaces. Estas moléculas aumentan el contraste intrínseco de las imágenes en las regiones donde se acumulan aumentando tanto la sensibilidad como la especificidad en el diagnóstico. El campo de los agentes de contraste está actualmente en continua evolución aprovechando en las nuevas oportunidades que ofrece la Nanotecnología. En esta tesis, describiré nuevos agentes de contraste con aplicaciones en imagen multimodal basados en recientes desarrollos nanotecnológicos. El Capítulo 1 presenta las diferentes modalidades de imagen usadas en clínica y la primera generación de agentes de contraste. El Capítulo 2 describe el estudio sistemático y la evaluación de un nuevo agente de contraste nanoparticulado útil en medidas de perfusión tumoral y respuesta inmunológica mediante Imagen por Resonancia Magnética. El Capítulo 3 presenta el desarrollo de una nueva composición teragnóstica basada en liposomas que contienen tanto una molécula terapéutica como un biomarcador para imagen médica. La eficacia de esta nueva formulación se comprueba mediante una variedad de técnicas de imagen y con diferentes modelos animales de inflamación y cáncer. Finalmente, en el Capítulo 4, describe el desarrollo y caracterización de un nuevo agente de contraste anisotrópico para Imagen por Resonancia Magnética que aprovecha las extraordinarias propiedades magnéticas de los Nanotubos de Carbono. En el capítulo, se investigan sus propiedades magnéticas y su potencial utilización como agentes de contraste avanzados de naturaleza anisotrópica. En resumen, en este trabajo se desarrolla, caracteriza y evalúa una nueva generación de agentes de contraste nanoparticulados y sus aplicaciones en técnicas de imagen multimodal.

Index

Index of Figures

Index of Tables

Abbreviations

^{1}H HRMAS: Proton High Resolution Magic Angle Spectroscopy

3D: Three dimensions

^{99m}Tc: Metastable nuclear isomer of technetium-99

ADC: Apparent Diffusion Coefficient of water

CBF: Cerebral Blood Flow

CBV: Cerebral Blood Volume

CEST: Chemical Exchange Saturation Transfer

CPMG: Carr-Purcell-Meiboom-Gill

DLS: Dynamic Light Scattering

DOSY: Diffusion-Ordered NMR Spectroscopy

DOTA: 1,4,7,10-tetraazacyclododecane-1,4,7,10-tetraacetic acid

DSS: Sodium Dextran Sulfate

DTPA: Diethylendiamino pentaacetic acid

EPI: Echo-Planar Imaging

Eq: Equation

FDG: ^{18}F-2-Deoxiclucose

FOV: Field of View

LDH: Lactate Dehydrogenase

MR: Magnetic Resonance

MRI: Magnetic Resonance Imaging

MSME: Multi Slice Multi Echo

MTT: Mean Transit Time

NMR: Nuclear Magnetic Resonance

PAA: Polyacrylic Acid

PARACEST: Paramagnetic Chemical Exchange Saturation Transfer

PET: Positron Emission Tomography

PLGA: Poli-lactic-glutamic acid

r_1: longitudinal relaxivity

r_2: transversal relaxivity

r_{2*}: transversal relaxivity with susceptibility

RARE: Rapid Acquisition with Relaxation Enhancement

SD: Standard Deviation

SPECT: Single Photon Emission Computed Tomography

T_1: Longitudinal relaxation time

T_1w: Image weighted in T_1

T_2: Transversal relaxation time

T_2w: Image weighted in T_2

T_{2^*}: Transversal relaxation time with susceptibility

TE: Echo time

TEM: Transmission Electron Microscopy

TLC: Thin Layer Cromatography

TMS: Tetramethyl silane

TR: Repetition time

TSP: Trimetil sylil 2, 2',3, 3' tetradeutero sodium propionate

ω-3 PUFA-EE: Omega-3 polyunsaturated fatty acid ethyl ester

Chapter 1

Introduction

Chapter 1 provides an introduction to the different multimodal bioimaging methods presently used as diagnostic tools in the clinic and the contrast agents currently available to enhance their image quality and information.

1.1. Multimodal Molecular Imaging

Biomedical images originate from the interaction between an electromagnetic radiation and the biological specimen. The electromagnetic spectrum (Figure 1.1) spans from the shortest wavelengths and highest energies associated to the cosmic rays to the longest wavelengths and lowest energies associated to the heating radiation. The γ-radiation, X-rays, ultraviolet, visible and infrared lights, micro- or radiofrequency waves and also heat, lay in between these two extremes.

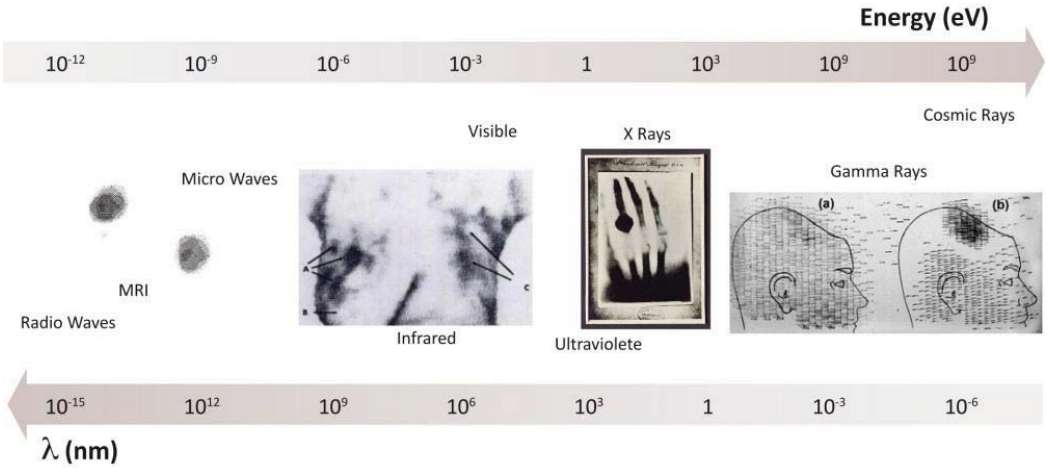

Figure 1.1. The electromagnetic spectrum expressed as energy (top) or associated wavelength (bottom). The middle panel shows some of the initial images obtained from each modality including radiofrequency (MRI) [1], infrared [2], X-Rays [3], and γ-rays (PET) [4].

Nuclear medicine approaches involve the use of highly penetrating γ- and x-ray radiations, generating high sensitivity (10^{-12} M) images with limited resolution (mm). Optical images may become very sensitive (10^{-15}M), as in microscopy, but their penetration capacity within the biological

specimen is limited in vivo (mm) and only, very thin objects or highly superficial processes, can be imaged. Finally, radiofrequency imaging provides excellent penetration capacity and resolution (μm), at the expense of very limited sensitivity (10^{-3}M). Taken together, these considerations suggest that there is no single optimal imaging modality, all of them presenting advantages and limitations. This provides a sound basis to combine the different imaging modalities in a hybrid manner to obtain a single multimodal image including the information derived from the different modalities, thus overcoming the specific limitations of each modality with the advantages of the others [5].

The physical interaction between the radiation and the specimen involves most of the times, its transmittance though the biological medium and the detection of the transmitted radiation across the object with suitable detectors [6]. This is the case of optical imaging and nuclear imaging. The image generated follows then the Lambert-Beer Law

$$I_t = I_0 e^{-\varepsilon\, d} \qquad \text{Eq. 1.1}$$

where I_t is the intensity of the image detected, I_0 the intensity of the radiation source before the interaction, ε is the extinction coefficient revealing the density of the specimen towards the transmitted radiation in a unit of length and *d* the distance travelled by the radiation through the object. In the case of nuclear imaging, the source of radiation is inside the specimen and decays rapidly with time because of the radioactive decay law, so corrections need to be done to account for this

circumstance, particularly in the case of positron emitters with very short half-lives.

In general, a planar image is obtained after detecting the transmitted radiation either with a digital camera in the case of optical imaging, or through a coronal array of highly efficient scintillation detectors in nuclear imaging [6, 7]. The reconstruction process, normally used in X-rays and nuclear medicine approaches, was first proposed by Godfrey Hounsfield and plays a fundamental role in nuclear imaging [8]. Since then a variety of reconstruction algorithms have been proposed with increasing resolution and computing time efficiency [9].

The discovery of Magnetic Resonance Imaging disclosed a completely new imaging strategy, not based on the transmittance phenomenon [1]. Rather, it took advantage of new physical interaction, based in the magnetic properties of biological nuclei in the sample and how they interact with static and dynamic external magnetic fields. The method used non-ionizing radiation and presented improved resolution when compared to nuclear medicine and *in vivo* optical imaging approaches, at the expense of a more limited sensitivity. More details on this method are provided in the next sections.

Despite the intrinsic image contrast determined by the physical properties of the tissues, the use of exogenous contrast enhancing molecules has been generalized in all imaging modalities [10-14]. These molecules are designed to enhance selectively and sensitively the intensity of the images in regions of tissue presenting particular

physiological, cellular or molecular properties, favoring enormously the recent development of the molecular and cellular imaging field [15].

The initial contrast agents were chemicals with subnanometric dimensions active in the different regions of the electromagnetic spectrum. Briefly, periodinated benzenes, Gadolinium chelates and ^{99m}Tc derivatives were among the first contrast agents used in X-ray, MRI, and nuclear medicine, respectively [11, 16, 17]. More recently, nanostructured materials have shown improved resolution and sensitivity properties with respect to the classical chemicals, as well as capacity to operate as multifunctional diagnostic and therapeutic (theragnostic) agents, thus opening a new horizon for the applications of nanotechnology in biomedical imaging [18, 19].

In this thesis I will describe new generations of nanostructured contrast agents with improved performance in Magnetic Resonance Imaging and the potential use as theragnostic drugs. First, I will describe the fundamentals of Magnetic Resonance and Magnetic Resonance Imaging. Second, I will present a new superparamagnetic nanoparticle with improved pharmacokinetic properties, able to generate high quality images of tumoral perfusion. Third, I will investigate the encapsulation in liposomes of superparamagnetic nanoparticles, rhodamine-100 (rhodamine-100 chloride) and / or omega-3 polyunsaturated fatty acid ethyl ester to evaluate their efficacy as a novel anti-inflammatory theragnostic agent. Finally, I will implement the use of single wall and multiwall carbon nanotubes, as molecular anisotropy probes able to encode directionality in MRI images.

1.1.1. Magnetic Resonance Imaging

The Magnetic Resonance Phenomenon

MRI techniques are based on the outstanding physical properties of the Nuclear Magnetic Resonance (NMR) phenomenon, as described by Felix Bloch [20] and Edward Mills Purcell [21] in 1946. This phenomenon is based on the fact that nuclei inside a magnetic field absorb electromagnetic radiation at a specific frequency, emitting the same radiation after the relaxation of the nuclei occurs [22, 23]. The frequency of this radiation depends on the magnetic field applied to the nuclei being excited. Not all nuclei present this phenomenon. It is necessary for the nuclei to have a non-zero spin value (an intrinsic quantum property) which leads in a non-zero magnetic moment (μ) with a gyromagnetic ratio (γ). Thus, a nucleus like ^{1}H presents NMR absorption, while ^{18}O does not present it. Due to the quantum nature of the spin (S), the magnetic moment presents only certain allowed values, depending on the magnetic quantum number *m*. So the z component of the magnetic moment of a nucleus is given by:

$$\mu_z = \gamma S_z = \gamma m \hbar \qquad \text{Eq. 1.2}$$

where $\hbar$ is the Planck constant divided by 2π (the z component refers to the magnetization vector S along the direction of the static magnetic field B_0). If we introduce the nucleus in a magnetic field, the next expression for the energy of this system applies:

$$E = -\mu_z B_0 = -\gamma m \hbar B_0 \qquad \text{Eq. 1.3}$$

For a two spin state ($m = \pm 1\ _2$) nucleus like the ^{1}H, the difference in energy between the stationary state and the excited state is given by:

$$\Delta E = \mu \hbar B_0 \qquad \text{Eq. 1.4}$$

And, since the difference in energy between two nuclear states is given by

$$\Delta E = h\upsilon_0 \qquad \text{Eq. 1.5}$$

the frequency of the radiation needed to excite the nuclei and induce a transition (as well as the frequency of the radiation emitted in the corresponding relaxation process) is given by

$$\upsilon_0 = \frac{\gamma B_0}{2\pi} \qquad \text{Eq. 1.6}$$

Each nucleus presents a characteristic gyromagnetic ratio so the resonance frequency is specific for every nucleus even if placed in the same magnetic field. This characteristic resonance frequency is known as the Larmor frequency.

Once the nuclei have been excited, the magnetization acquired is eventually lost to the surroundings mainly through two magnetic relaxation processes, longitudinal or spin-lattice (T_1) and transversal or spin-spin (T_2) relaxation. The T_1 process (Figure 1.2) determines the

relaxation occurring in the z-axis, while the T_2 process (Figure 1.3) determines the magnetic relaxation in the x-y plane.

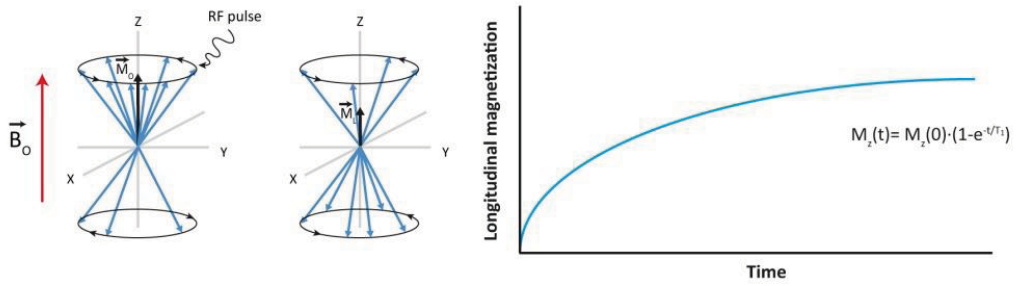

Figure 1.2. Scheme of T_1 relaxation. When the sample is excited with an RF pulse (left), some of the spins change their orientation and energy, resulting in a net decrease of the longitudinal magnetization component (center). When the pulse is turned off, the magnetization recovers to its original equilibrium value (right) with a time constant T_1.

The relaxation processes implies the loss of the magnetization acquired during the excitation process to the surroundings (lattice, in the T_1 process) or to other nuclei (spin-spin, T_2).

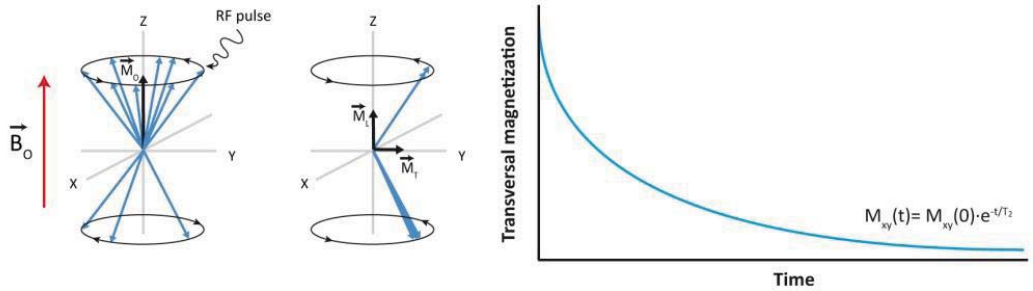

Figure 1.3. Scheme of T_2 relaxation. When the sample is excited with an RF pulse (left), the excited spins precess in phase, resulting in the appearance of net coherent transversal magnetization (center). When the pulse is turned off, the transversal magnetization loses coherence progressively and returns to its zero equilibrium value (right).

Field inhomogeneities may result in additional dephasing of the spins in the x-y plane in a process known as T_{2*}. In the presence of field inhomogeneities, as it happens in biological tissues, T_{2*} is always smaller than T_2.

Magnetic Resonance Imaging

Magnetic resonance imaging obtains images from biological objects by encoding the magnetization of every pixel in the three spatial coordinates x, y and z. This is done through the application of field gradients that encode the z and x coordinates as frequency dependent and the y coordinate as a phase dependence [1]. Briefly, the three dimensional localization of every pixel is encoded using either field or phase gradients

$$\omega_{z,x} = \ B_0 + G_x \ , \ B_0 + G_z \ \gamma \qquad \text{Eq. 1.7}$$

$$\Phi_y = \Phi_0 + G_y \Phi \qquad \text{Eq. 1.8}$$

One of the most commonly used sequences is the spin-echo sequence (Figure 1.4). The sequence consist of two sequential radiofrequency pulses, the first one is used to excite the sample while the second one is used to rephase the protons in the x-y plane (these pulses are separated by a time known as echo time TE/2, where TE is the time between the first pulse and the maximal echo signal). The spin-echo sequence is repeated for every value of the phase encoding gradient with a delay time known as repetition time, TR, used to recover the longitudinal magnetization before the next pulse train.

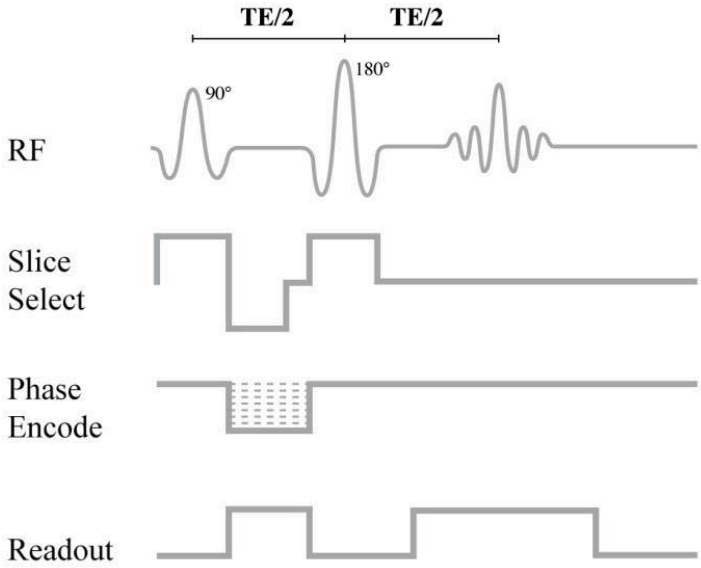

Figure 1.4. Spin-echo sequence. The top trace corresponds to the radiofrequency pulse train (π/2, π, echo) and the lower ones to the slice selection gradient (next to top), the variable phase encoding gradient (middle) and the readout gradient of the echo (bottom trace). TE is the time between the π/2 pulse and the echo and TR is the time between two successive π/2 pulses.

The different echo signals S obtained in the time domain for every value of the phase gradient (k space), are digitized and transformed bidimensionally into a frequency map (the image) using the Fourier Transform theorem:

$$f\ \omega\ = \int_{-\infty}^{\infty} f\ t\ e^{i\omega t} dt \qquad \text{Eq. 1.9}$$

where $f\ \omega$ is the signal intensity in the frequency domain and $f\ t$ the signal intensity (microvolts) in the time domain.

The signal intensity S obtained in every pixel after the Fourier Transformation follows the equation

$$S \propto \rho\, e^{-TE\ T_2} \quad 1 - e^{-TR\ T_1} \quad 2\, e^{TE\ 2T_1} - 1 \qquad \text{Eq. 1.10}$$

where ρ is the spin density, TE the echo time, TR the repetition time , T_1 the longitudinal relaxation time and T_2 the transversal relaxation time [22]. It is possible to weight the signal intensity of the pixel in T_1, T_2 or ρ choosing the proper pulsing conditions. Using, very short TE (much shorter than T_2) and TR values shorter than T_1, the image is said to be dominated by the T_1 relaxation terms, or "weighted in T_1". Using very long TRs (longer than T_1) and TE values in the range of T_2, the image obtained is said to be dominated by the T_2 term, or "weighted in T_2". Finally, using very long TR values (much longer than T_1) and very short TE values (much shorter than T_2), the T_1 and T_2 influences are minimized and the image is said to be weighted in proton density (ρ).

1.1.2. Optical Imaging

Optical Imaging is a technique that permits the measurement of light produced in vivo by fluorescence or bioluminescence mechanisms. It is a non-invasive procedure with low resolution but with high sensitivity [24, 25].

This effect is based in the luminescence effect where some chemical compounds absorb radiation and produce then light of a well-known frequency. A usual chemical compound used in this technique is luminol which in presence of myeloperoxidase or iron complex as catalysts suffers a reaction generating chemiluminiscence [26, 27]. This effect is used in detecting inflammations (Figure 1.5).

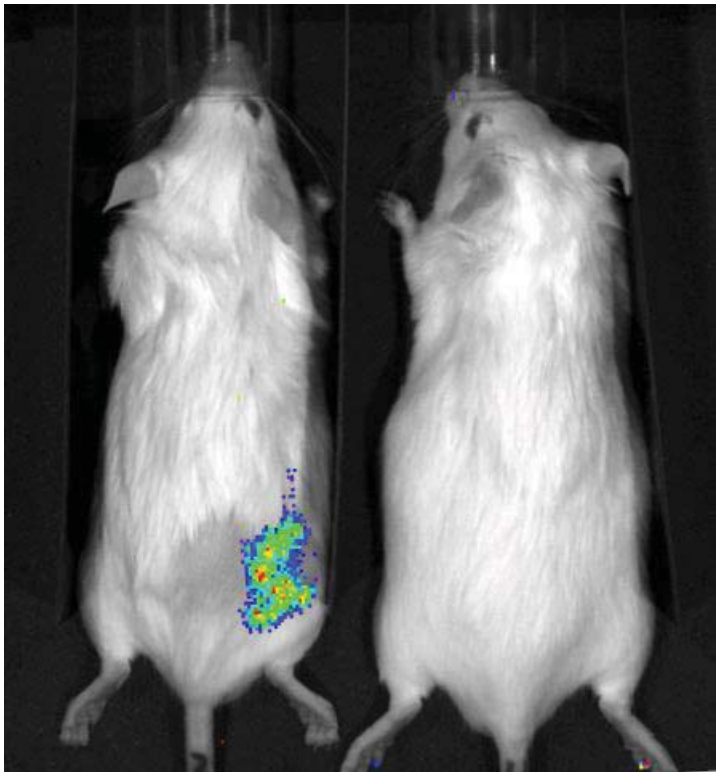

Figure 1.5. Representative bioluminescence images obtained after the administration of luminol. Two mice subjected to sodium dextran sulfate (DSS) intoxication are investigated, one of them injected with luminol (left) and the other one without the optical agent (right). Note how inflammatory disease triggers myeloperoxidase expression in the neutrophils and the formation of bioluminescent derivative of luminol [24, 26].

The optical approach has been reinforced recently with the development of transgenic mice, carrying the luciferase promoter coupled to specific genes activated by inflammation (NFkappaB) or cancer (VEGF) [28, 29]. These mice, express the luciferase gene, every time the coupled gene is expressed, and consequently emit light spontaneously if luciferin is administered [30].

1.1.3. Ionizing Radiation Imaging

X-Rays

The potential use of X-Rays as a tool in clinical imaging was first discovered by Wihelm Röntgen at the end of 19th century [3]. A high energetic electron beam emits radiation when the electrons are stopped. This is known as Bremsstrahlung radiation and has the enough energy to go through biological tissues being more attenuated by tissues containing large quantities of electron dense metals as calcium (as the bones or calcified lesions). So, if the tissue under study is accommodated between the electron beam source and a photograph film, images of bones or other electron dense tissues or implants can be obtained easily. Nowadays, X-Rays devices have evolved to obtain three-dimensional images or applied kinetically “on line” to measure transit times of the contrast agent in fluoroscopy studies [6, 31, 32].

Nuclear Radiation Imaging

The development of new nuclear technologies and accelerators permit the manipulation of the energy levels of the nucleus to release radiations of high energy, known as gamma rays. Gamma rays are more energetic than X-Rays and go through biological tissue with low attenuation. Using cyclotrons it is possible to synthesize radiopharmaceuticals with high tissue specificity, emitting gamma photons only from the target tissue. SPECT (Single Photon Emission Computed Tomography) was the first device developed using this technology. The most common radiopharmaceutical used in SPECT ^{99m}Tc attached to a molecule (normally an antibody) with high specificity causing an accumulation of the radiopharmaceutical in a specific tissue (e.g., tumoral tissue). ^{99m}Tc

emits one photon of 140 keV for each disintegration (the half-life of ^{99m}Tc is around 6 hours) which is recollected and visualized with a gamma camera compound by scintillation detectors, many times based in sodium iodide crystals doped with thallium (NaI(Tl)). A 3D software reconstructs the distribution of the photons allowing the spatial localization of the radiopharmaceutical emitter. PET (Positron Emission Tomography) is another technique of Nuclear Radiation Imaging. In this case, the radiopharmaceutical used emits positrons which are annihilated with electrons emitting two 511 keV gamma photons, in opposite directions. These photons are collected in a detector ring containing specialized gamma cameras (based most frequently on lutetium oxyorthosilicate LSO crystals) which surrounds the object, animal or patient. Because the emission of two photons occurs in opposite directions, the reconstruction software works with the coincidence of the detection to locate the original site of positron emission. The PET technique presents, because of the higher energies involved, higher resolution than SPECT, but remains limited by the shorter half-life of the PET radiopharmaceuticals as compared to SPECT. Both techniques depict very high sensitivity, albeit low resolution, and are heavily used in cell tracking and tumor detection [33, 34] (Figure 1.6).

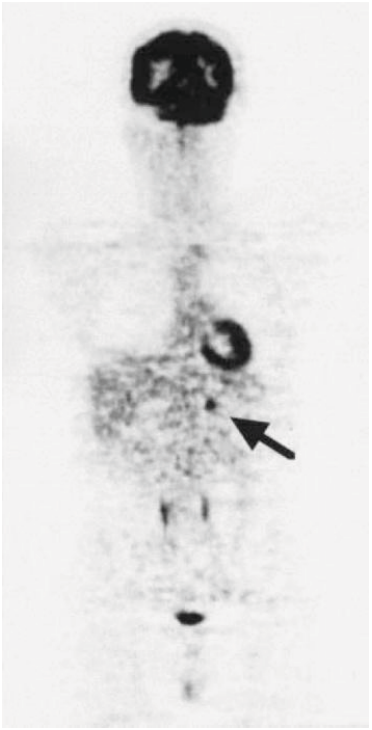

Figure 1.6. Representative PET image of a patient obtained after ^{18}F-2-deoxyglucose administration. Organs that take most contrast are brain, heart or bladder. It is possible to detect clearly a tumor in the liver (arrow) (taken from [33]).

1.2. Contrast Agents

Contrast agents are molecules active in the different frequencies of the electromagnetic spectrum able to enhance in the image particular regions of the imaged subject, in which they accumulate. Their accumulation is able to reveal specific receptor activations, different cellular or molecular processes, the extension of lesions and their pathophysiological properties or the response to therapies. The first generation of contrast agents involved small molecules with diameters much smaller than 1 nm [11].

In the nuclear medicine field, a large variety of SPECT or PET tracers haven been proposed, with dominant applications in oncologic and neurodegenerative diseases. In general, PET or SPECT tracers contain two parts, a targeting moiety providing the selectivity to the imaged process and a radionuclide moiety, containing the radionuclide emitting gamma rays with 140 meV (SPECT) or 511 meV (PET) enabling the detection. The targeting moieties are vectorial reagents, including either small chelates or even peptides, proteins or antibodies with molecular specificity for the desired target [35]. The radionuclides involve mainly ^{99m}Tc, ^{68}Ga, ^{111}In or ^{131}I for SPECT or ^{18}F, ^{11}C, ^{15}O for PET.

A large variety of SPECT probes are commercially available to monitor most frequently perfusion [36], hypoxia [37], inflammation [38], thyroid function [39] or even cerebral activation [40]. Their main advantage is the possibility to use relatively low cost gamma cameras for detection, available in many hospitals and the relatively long half-lives of the SPECT emitters (in the hour range), while their main limitation is the reduced resolution of the SPECT method [5, 6]. This limitation is overcome in large part through the use of PET probes which offer increase spatial and temporal resolution, at the expense of the more expensive PET equipment and the reduced half-life (in the min range) of the positron emitters. ^{18}F-2-deoxiglucose (FDG) is probably the most widely used PET tracer, despite its poor selectivity. FDG is taken up by virtually all tissues in an analogous manner to glucose, but it is not degraded by glycolysis, resulting in FDG accumulation in those regions with enhanced glucose transport. FDG reveals spectacularly the presence of tumors or metastases, regions of cerebral activation or even inflammatory lesions,

providing probably the most successful tracer in nuclear medicine. However, since glucose uptake is a universal process, the use of FDG is hampered by its lack of selectivity, making very difficult to discriminate tumoral from inflamed regions, resulting in a non-negligible number of false positives (up to 30% [41]) and requiring in many cases complementary examinations with other tracers or modalities.

Contrast agents for MRI, involve mainly Gd(III) chelates, able to enhance water relaxation in those tissues where they accumulate [11]. Gd(III) is used because it has seven unpaired, slow relaxing electrons, and depicts the largest magnetic moment among the rare earth series. The ligands most frequently used are linear chelates derived from diethylendiamino pentaacetic acid (DTPA) or cyclic chelates derived from the tetra-aza-macrocycles or cyclen derivatives (DOTA). In all these cases, the ligand provides eight binding sites anchoring the Gd(III), leaving free one the nine chelating sites of the metal, for water contact. The contact between water in the solution or tissue with the Gd(III), and the fast exchange of this water molecule with the bulk solution, reduces very significantly the relaxation times of the tissue, resulting in clearly enhanced image intensity in those regions containing the chelate [11]. The use of other lanthanides as Dy(III), may transform the same chelates in T_2 enhancing probes, due to the inherent T_2 relaxing properties of Dy(III) [42]. Currently there are no specific contrast agents to enhance T_{2*}. In this thesis, I will provide an interesting alternative for this purpose.

MRI includes additionally a large variety of molecules able to enhance image intensity using other mechanisms including mainly magnetization transfer methods [43]. These agents are known as diamagnetic Chemical

Exchange Saturation Transfer (CEST) or Paramagnetic Chemical Exchange Saturation Transfer (PARACEST) agents. These molecules can be customized to reveal important aspects of the lesions including properties of the microenvironment as pH [44], monovalent or divalent ion concentration [45] or temperature [46], among others.

Superparamagnetic iron oxide nanoparticles have been implemented more recently to increase the relaxing capacity of the paramagnetic chelates [47-49]. These particles contain a magnetite core (Fe_3O_4) core, covered most frequently by a dextran or lipid coat. The particles are prepared by alkaline precipitation of mixtures of Fe^{3+} and Fe^{2+} in the presence of stabilizing agents as dextran or oleic acid. These depict enormous relaxivity values, as compared to the Gd(III) chelates, allowing for a significant increase in the sensivity for MRI detection. This is due to the fact that the cooperative alignment of the magnetic moments from the iron ions in the superparamagnetic nanoparticles, results in significantly larger magnetic moments than the additive alignment of the paramagnetic Gd(III) moments. Superparamagnetic behavior results mainly in T_2 enhancement, in contrast with the paramagnetic T_1 enhancement, of the Gd(III) chelates. Little information exist of the T_{2*} relaxing capacity of these particles [23]. In this thesis, I will describe a new iron-based nanoparticle coated with a polymer of acrylic acid, able to generate excellent T_{2*} contrast.

Finally, an ample collection of optical probes emitting fluorescence, luminescence or near infrared radiation, have been described [50-52]. These probes are limited by the reduced penetration in tissues of the optical wavelengths, but are well endowed to image small animals as

mice or cells, using the new generation of CCD (Charge Coupled Devices) cameras and optical scanners. However, the performance of these probes is supported by their excellent selectivity to respond to very specific molecular processes, as protease activation [51], angiogenesis [53] or inflammation [54].

The advent of Nanotechnology has provided a collection of new tools and formulations that may overcome the limitations of the first generation of contrast agents (Figure 1.7). Basically, the use of nanoparticles, decorated with vectorial molecules as antibodies or peptides may increase significantly the molecular selectivity of contrast agents, otherwise non selective, and the use of liposomal formulations may allow to combine probes for different imaging modalities in the same vehicle, or even add a therapeutic molecule. Moreover, these novel formulations are expected to decrease the dose of administered contrast required for successful imaging, since most of the non-selective contrast agents currently administered, go to uninteresting subject regions or become eliminated. Nanotechnology has open then a new era in the contrast agent field, optimizing the detection by imaging of the contrast agent and eventually combining the diagnostic and therapeutic potentials by adding a therapeutic agent to the same nanotechnological platform, to produce the new generations of "theragnostic agents". Figure 1.7 presents some of the most commonly used nanoparticle formulations. Solid nanoparticles (or powders) may be produced of varying sizes, by the spray-drying method, allowing for the encapsulation of drugs and contrast agents for oral delivery, in most cases. To this end

normally, poli-lactic-glutamic nanoparticles (PLGA) are used for oral or rectal administration [55].

Lipid nanoparticles, liposomes [56, 57] and micelles [58], provide excellent platforms to administer combinations of contrast agents and therapeutic principles, in intravenous administrations. In this thesis, I will illustrate this aspect combining the use of a novel iron-oxide nanoparticle with an anti-inflammatory agent, to obtain strong theragnostic agent with anti-inflammatory and antitumoral effects.

Finally, the use of graphene structures has recently been added to the array of nanotechnology platforms, to administer contrast agents, combining imaging probes and therapeutic agents. Gd(III) atoms have been included in fullerenes and carbon nanotubes. However, the magnetic properties of these arrangements and their use as contrast agents, remains nowadays insufficiently characterized. In this thesis, I will describe the magnetic properties of single-wall and multi-wall carbon nanotubes as novel nanoprobes for anisotropic MRI.

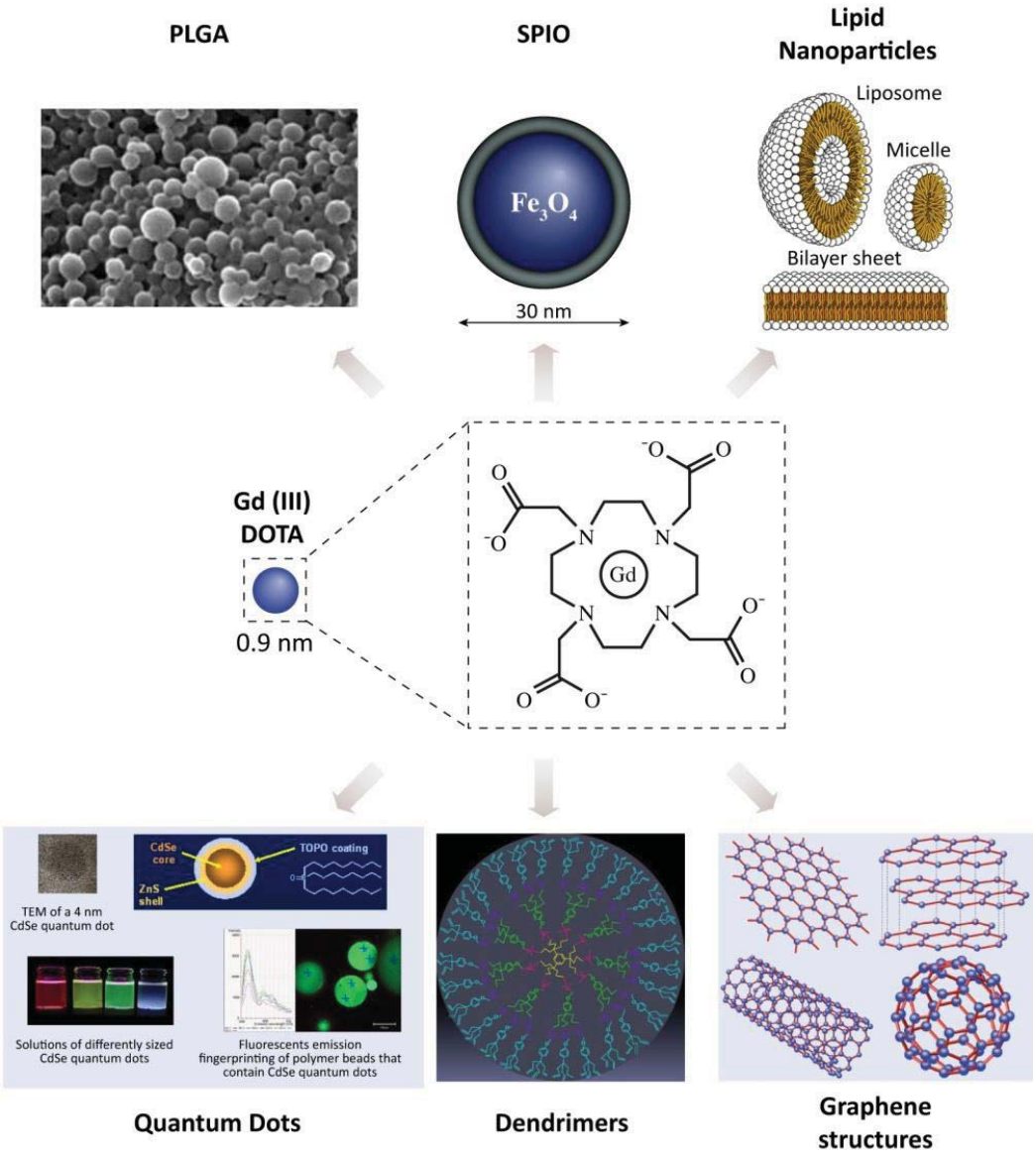

Figure 1.7. The development of recent nanotechnology approaches has driven the creation of new families of imaging contrast agents. Classic contrast agents as Gd(III) DOTA are now competing with newer, more sensitive and more selective, contrast agents based on PLGA nanoparticles (top left), SPIO nanoparticles (top center), Lipid Nanoparticles (top right), Quantum Dots (bottom left), Dendrimers (bottom center)s or Graphene structures (bottom right).

Chapter 2

Nanotex: a novel superparamagnetic nanoparticle to image tissue perfusion by Magnetic Resonance Imaging

Chapter 2 describes the preparation, characterization and evaluation of a novel superparamagnetic nanoparticle as an advanced, low adherence, superparamagnetic contrast agent for Magnetic Resonance Imaging of tissue or tumoral perfusion.

2.1. Introduction

The effect of chelated paramagnetic metals as contrast agents in MRI has been known since the early 1980's [22]. Gadolinium, a paramagnetic metal of the rare earth series, became the optimal candidate because its large magnetic moment, seven unpaired electrons and their long electronic relaxation time. However, its significant toxicity when administered free precluded its use in the clinic. In 1983, the first gadolinium chelate which eliminated the toxic effect of free gadolinium was proposed, opening the opportunity to use it as a safe contrast agent in MRI [11, 59]. Other gadolinium chelates, based on the cyclen structure followed soon after [11, 60]. However, the need of high doses of these paramagnetic agents to obtain significant MR contrast, and the recent appearance of toxic responses in some chelates [61], challenged their use. In the late 80's, new generations of more efficient contrast agents based in the use of superparamagnetic nanoparticles, were described [47]. The first nanoparticles consisted of a nucleus of magnetite (Fe_3O_4) covered by a layer of free or cross-linked dextran. Some of these nanoparticles, as Endorem or Resovist, were shown to depict high relaxing power, be devoid of significant toxic effects and thus, became commercialized and used in the clinic soon after [62, 63]. However, the first generation of superparamagnetic nanoparticles was not free from adverse effects. Despite their enormous relaxing power, these nanoparticles became trapped by the reticuloendotelial system and because of the dextran cover, became unselectively adsorbed over capillary and tissue surfaces, accumulating in tissues after repeated administrations, thus disadvising fast subsequent administrations [64].

In this chapter we propose, characterize and evaluate a new superparamagnetic nanoparticle maintaining the iron oxide core, but covered by a layer of polyacrylic acid. The nanoparticle depicts improved T_{2*} relaxation properties, reduced non-specific adherence in capillaries and tissues, very low splenic accumulation and adequate T_1 and T_2,relaxation properties, supporting its use as an improved superparamagnetic contras agent in MRI, with emphasis in perfusion imaging.

2.2. Materials and Methods

2.2.1. Preparation of the Iron Oxide Superparamagnetic Nanoparticle Nanotex.

Magnetite (Fe_3O_4) nanoparticles were prepared by the co-precipitation [65] of Fe^{3+} and Fe^{2+} ions (molar ratio 2:1, total Fe 0.3M, 25 ^{0}C) with ammonia (29.6%, pH:10) in an inert atmosphere, followed by hydrothermal treatment (80 ^{0}C, 30 min) [66]. The magnetic nanoparticles were washed several times with deionized water and ethanol, and dried at 70 ^{0}C in a furnace for subsequent treatment. For the binding of polyacrylic acid (PAA), 100 mg of Fe_3O_4 nanoparticles were first mixed with 2 ml of buffer A (0.003 M phosphate, pH 6) and 0.5 ml of carbodiimide solution (0.025 g·mL^{-1} in buffer A). After being sonicated for 10 min, 2.5 ml of PAA solution (60 mg·mL^{-1} in buffer A) were added and the reaction mixture sonicated (Ultrasonic bath, JP Selecta, Abrera, ES) for an additional 30 min. Finally, the PAA-coated Fe_3O_4 nanoparticles were recovered magnetically, washed with water twice and dialyzed

against a buffer saline solution. In the following, the resulting nanoparticle is named Nanotex.

2.2.2. Magnetic Relaxation Properties.

The evaluation of magnetic relaxation properties (T_1, T_2 and T_{2*}) of Nanotex was investigated using both, a Bruker Minispec system (Bruker Biospin, Ettlingen, DE) at 1.5 Tesla, a clinical field strength, and with a Bruker Pharmascan scanner (Bruker Biospin, Ettlingen, DE) operating at 7 Tesla [67].

T_1 values at 1.5 T were determined with the progressive saturation sequence [68], TE: 10 ms, TR: 70-12000 ms (at least 9 values). T_1 values at 7T were obtained using a spin-echo sequence with TE: 12.62 ms, TR: 150-6000 ms (7 echoes) using coronal sections (1.5 mm) across a collection of capillaries (1mm diameter) containing, each one, increasing concentrations of Nanotex. Acquisition conditions were; FOV (Field of View) 30 mm, matrix size 256x256 pixels. T_1 values (mean ± SD) were determined in T_1 maps calculated by fitting pixel by pixel the expression $S = S_0 \cdot \ 1 - e^{-TR \ T_1}$ (where *S* is the signal value for each *TR* and S_0 the value for *TR=0*) using the in-house developed program MyMap Analyzer running in a MatLab environment (The Mathworks, Natick, Massachusetts, USA). T_1 values are expressed in ms as mean ± standard deviation.

T_2 values (ms) at 1,5 T were obtained (Minispec, Bruker Biospin, Ettlingen, DE) in the same tubes used for T_1 measurements, using a spin-echo sequence (Carr-Purcell-Meiboom-Gill) independent of spin diffusion with TR: 9000 s, TE: 10-2000 ms (at least 9 values) [68]. T_2 values at 7T were determined (mean ± SD) using a spin-echo sequence with TR: 5000

ms, TE: 12-600 ms (50 echoes), FOV 30 mm, matrix size 256x256 pixels. T_2 maps were calculated from the collection of T_2 weighted images by non-linear fitting of the pixel intensities to the expression $S = S_0 \cdot e^{-TR\ T_2}$ (where *S* is the signal value for each *TR* and S_0 the value for *TR=0*).

T_{2*} maps at 7T were acquired from coronal sections (1,5 mm) across a collection of capillaries (1mm diameter) containing increasing concentrations of Nanotex, using a gradient echo sequence [68], TR: 300 s, TE: 2.3-40 ms (at least 9 values), a FOV of 30 mm, matrix size of 256x256 and a coronal section of 1.5 mm [68]. T_{2*} values were calculated from the T_{2*} maps by non-linear fitting of the pixel intensities to the expression $S = S_0 \cdot e^{-TR\ T_{2*}}$ (where *S* is the signal value for each *TR* and S_0 the value for *TR=0*) using the in-house developed program MyMap Analyzer running in a MatLab environment (The Mathworks, Natick, Massachusetts, USA). T_{2*} values are expressed in ms as mean ± standard deviation.

2.2.3. Citotoxicity

The *in vitro* toxicity of Nanotex in C6 glioma cell cultures was investigated measuring the metabolic reduction of MTT (tetrazolium salt) to formazan, a process which evaluates the potential red-ox and the intracellular oxidative metabolism. The cellular viability is directly associated to the reduction of MTT to formazan, a reaction which only occurs in living cells [69]. MTT test was implemented for C6 incubations with increasing concentrations of Nanotex, and the results expressed as a percentage of cell survival.

2.2.4. Splenic Accumulation

Splenic accumulation [70] of Nanotex *in vivo* was determined by measuring T_{2*} values in spleens isolated from CD1 mice sacrificed one hour after intravenous injection of Nanotex (15 micromol Fe/kg body weight). This dose corresponds to the amount recommended for use in the clinic by commercial nanoparticle manufacturers and has served as a reference dose here. The spleens were isolated from mice killed by cervical dislocation and placed in six well Plexiglas plates allowing for construction of the corresponding T_{2*} maps. The resolution and sensitivity achieved with this method allowed for very precise measurements of T_{2*} in spleen *ex vivo*, not achievable for the spleen *in vivo*.

2.2.5. Pharmacokinetics

To investigate the *in vivo* pharmacokinetics of Nanotex by MRI, we obtained T_{2*} weighted images and the corresponding T_{2*} maps of coronal sections across the thorax and abdomen of Swiss CD1 mice, before intravenous administration of Nanotex and at increasing times after its administration (1, 3, 6, 24, 48, 168 h) [71]. The Nanotex nanoparticles were administered intravenously as an aqueous solution at a dose of 15 micromol Fe/kg body weight. This dose corresponds to the amount recommended in the clinic by commercial nanoparticle manufacturers of Endorem or Resovist, and has served as a reference dose here.

2.2.6. Use of Nanotex in MRI Perfusion Imaging

Microvascular perfusion was assessed by monitoring kinetically by MRI the passage of a contrast agent “bolus” through a body section (bolus tracking method) [72, 73]. Basically, after a very fast injection, the

contrast agent solution moved through the vasculature as a “bolus”, maintaining the initial concentration of the injected solution in the microvasculature, at least during its first passage through each tissue. When the MR imaging plane is reached by the bolus, a decrease in the image intensity is measurable by MRI that is proportional to the concentration of the injected agent [74].

To investigate tissue and tumoral perfusion we used the C6 glioma model [75]. Briefly, male adult Sprague-Daweley rats received 10^6 C6 cells in the caudate nucleus. Tumors developed during the next two weeks until the MRI perfusion measurement took place. The kinetics of contrast agent passage across the imaging plane, where acquired using a Bruker Biospec scanner (7T, Bruker BIOSPIN, Ettlingen, DE) with an echoplanar sequence (EPI), with TE:10.32 ms and TR: 277,51 ms (150 T_{2*} images). A bolus of contrast agent (250 µL of Nanotex, 90 µmoles Fe/Kg) was injected intravenously in the tail vein of Sprague-Dawley adult male rats (n= 6) carrying implanted C6 glioma 10 seconds after the beginning of the acquisition sequence

The kinetics of contrast agent passage through the imaging plane, approaches a gamma function with an initial portion, a point of maximum intensity and a decrease until disappearance. The area under this curve represents the cerebral blood volume (CBV; ml/100g) in the imaging plane. The time between the beginning of passage and the maximum concentration is the mean transit time (MTT), a magnitude that measures the time (s) in which half of contrast bolus has passed through the section. Finally, the cerebral blood flow (CBF) is calculated as

the CBV/MTT ratio, representing blood flow [(ml/100g)/min] through the investigated cerebral section in a pixel by pixel manner [74].

The perfusion values (CBV, CBF and MTT) were obtained using the home made program MyMap Analyzer by the adjustment of the increment of T_{2*} relaxivity (Δr_{2*}) to a gamma function. With this adjustment, the perfusion values are given by the equations:

$$\mathrm{CBV} = \int \Delta r_{2*}(\tau) \cdot d\tau \qquad \text{Eq. 2.1}$$

$$\mathrm{MTT} = \frac{\int \tau \cdot \Delta r_{2*}(\tau) \cdot d\tau}{\int \Delta r_{2*}(\tau) \cdot d\tau} \qquad \text{Eq. 2.2}$$

$$\mathrm{CBF} = \frac{CBV}{MTT} \qquad \text{Eq. 2.3}$$

2.2.7. Evaluation of Nanotex as a CT Contrast Agent

Due to the high electron density of the iron core of Nanotex, we evaluated its potential use as contrast agent in CT (INVEON PET-SPECT-CT, Siemens AG, DE). The CT images were taken with a voltage of 80 kV and a current of 500 µA. The exposure time was 220 ms, acquiring 180 projections with a FOV of 57.2 x 57.2 mm. We obtained an image of X Rays of different concentrations (25%, 50%, 75% and original sample) of Nanotex and compared it with that of a commercial CT contrast agent, Ultravist (300 mg / mL, Bayer, DE) dissolved in water, placed closely in parallel wells of a 96 well plate. The X Ray densitometries obtained were analyzed using the freely available ImageJ package (http://rsbweb.nih.gov/ij/, National Institutes of Health, Bethesda, Maryland, US).

2.3. Results

2.3.1. Preparation and Characterization

The study of the magnetic relaxation behaviour constitutes an essential requirement in the characterization of a new contrast agent for Magnetic Resonance Imaging. Figure 2.1 summarizes the relaxation properties of solvent water in Nanotex suspensions for T_1 (A, C) and T_2 (B, D) at 1.5 Tesla in water (top panels) and serum (bottom panels), in concentrations ranging from 0 to 0.05 mM Fe.

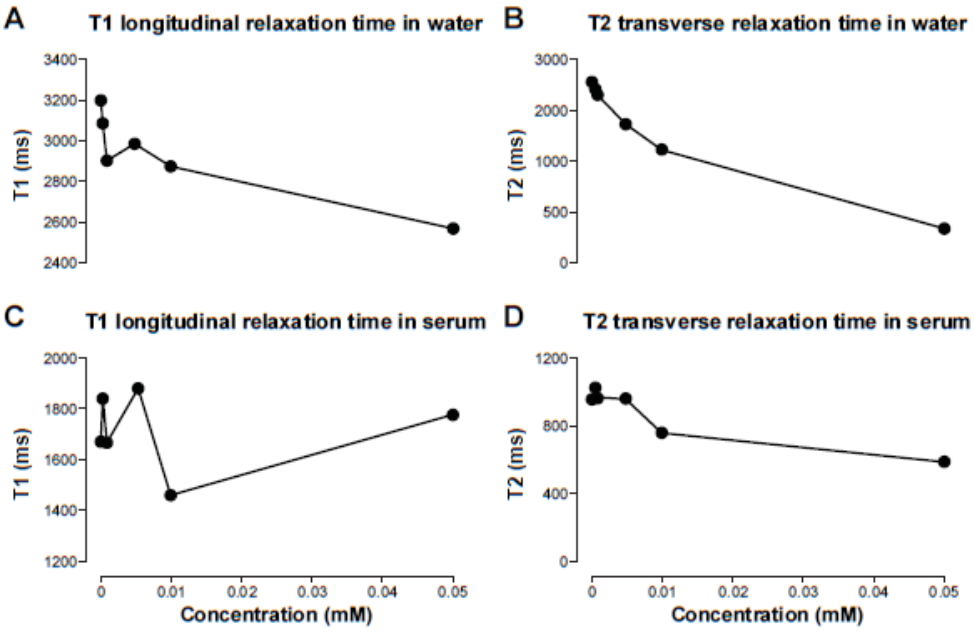

Figure 2.1. Magnetic relaxation properties of water in Nanotex suspensions of increasing nanoparticle concentration at 1.5 Tesla. T_1 (A, C) and T_2 (B, C) relaxation in water (top) or fetal bovine serum (bottom), in concentrations ranging from 0 to 0.05 mM Fe.

Nanotex reduces the values of the different water relaxation times, T_1 or T_2 in a concentration dependent manner. As expected for a superparamagnetic nanoparticle, the reduction is much larger in T_2 than

in T_1.The highest concentration tested reduced T_1 water from 3200 ms to 2600 ms, and T_2 from 2500 ms to 600 ms, respectively. . In the case of serum, a reduction of T_1 from 1800 ms to 1600 ms, and T_2 from 1000 ms to 700 ms is observed. The Nanotex effect on T_2 remains higher than in T_1, but the magnitude is smaller than that observed in pure water. This may be due either to a reduction in the effective amount of water available for relaxation with the nanoparticle in serum (solvation of proteins, carbohydrates and ions in plasma) or to reduction of the free nanoparticle concentration in water due to binding to plasma components.

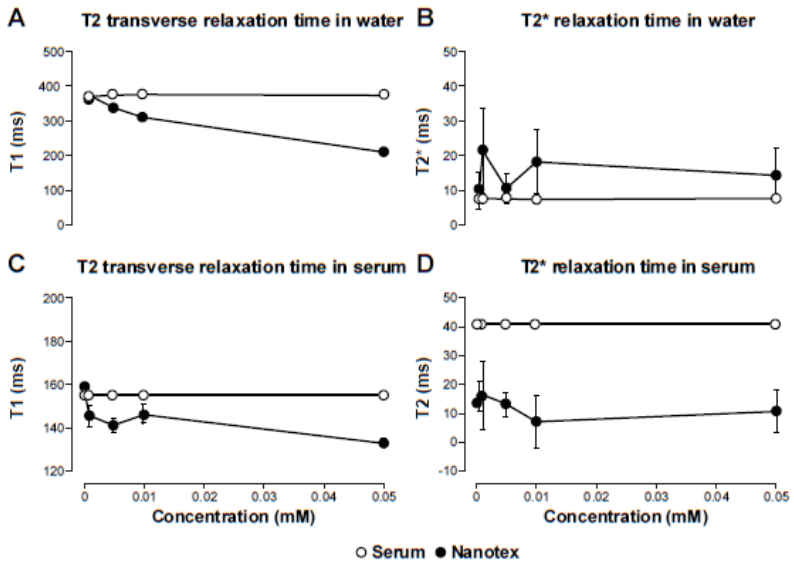

Figure 2.2. Magnetic relaxation properties of water in Nanotex suspensions of increasing Fe concentration at 7 Tesla. T_2 (A, C) and T_{2*} (B,D) relaxation values at 7 Tesla in water (top) and fetal bovine serum (bottom) of Nanotex suspensions in concentrations ranging from 0 to 0.05 mM Fe. Values represent the mean ± SD of the pixels from a coronal plane taken across the capillaries for each condition.

Nanotex reduced the T_2 value of water from 300 ms to 220 ms in water and from 159 ms to 133 ms in serum, respectively. T_{2*} reductions by

Nanotex were to 18 ms in water and 10 ms in serum, respectively. Again, the reductions observed in T_2 and T_{2*}, were smaller in serum than in water, supporting the association of the nanoparticle to serum components in a way that decreases its relaxing capacity. These results were compared with those obtained with a commercial nanoparticulate contrast agent, Endorem (11.2 mg Fe / mL, Guerbet, FR) under the same conditions (Table 2.1).

Table 2.1. Comparison of r_1, r_2 and r_{2*} relaxivity values of Nanotex and Endorem suspensions in water and serum measured at 7 Tesla.

	r_1 ($mM^{-1}\cdot s^{-1}$) [a]		r_2 ($mM^{-1}\cdot s^{-1}$) [a]		r_2* ($mM^{-1}\cdot s^{-1}$) [a]	
Nanoparticle	*Water*	*Serum*	*Water*	*Serum*	*Water*	*Serum*
Endorem	1.1044	0.922	103.55	66.49	298.88	159.93
Nanotex	0.5524	0.4951	88.971	94.163	97.334	119.78

[a] Relaxivity values were determined at 22 ^{0}C as the slope of the linear increase in $1/T_1$, $1/T_2$ or $1/T_{2*}$ values with Nanotex or Endorem concentrations (0 - 0.05 mM [Fe]).

Table 2.1 summarizes the comparative relaxivity values measured in serum or water. The r_1 and r_{2*} relaxivity values of Nanotex were smaller than those of Endorem in water and serum, but r_2 of Nanotex reached a higher value than Endorem in serum. These results imply a significant advantage of Nanotex over Endorem when using imaging sequences weighted in T_2 in vascular imaging.

2.3.2. Toxicity Evaluation in Cell Cultures and *in vivo* Rodent Models

An evaluation of the potential cytotoxic effects of a new contrast agent is necessary to support its safety profile and potential applications in the clinic. The contrast agent should present reduced or absent cytotoxicity

and reduced tissue accumulation, allowing for multiple administrations without significant accumulations in specific tissues as the spleen.

Figure 2.3 shows the results of MTT reduction from C6 cells versus increasing concentrations of Nanotex or Endorem after 1 hour (A) and 24 hour (B) of incubation. Changes in cell viability are hardly detectable throughout the concentration range investigated, suggesting negligible cellular toxicity of Nanotex or Endorem in glioma C6 cell cultures. A positive control (a cytotoxic concentration of hydroxylamine) was employed to confirm that viable cells can be killed, and that cell killing and survival can be detected by the MTT reduction assay.

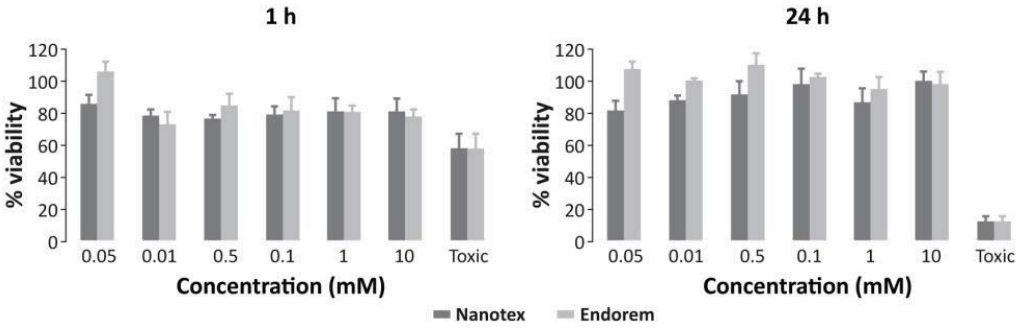

Figure 2.3. Comparative study of cytotoxicity of Nanotex and Endorem. Effect of increasing concentrations of Nanotex and Endorem on C6 cell viability detected by MTT reduction assay, after 1h (left) or 24h (right) incubation. Hydroxylamaine was used as a toxic control.

The next step in the development a new contrast agent development is to assess the *in vivo* toxicity. To this end, CD1 mice were injected with 15 micromol Fe/kg body weight of Nanotex or Endorem. This dose corresponds to the recommended dose in the clinic by commercial Endorem manufacturers and has served as a reference dose here. Figure 2.4 shows representative results of a study of accumulation of these

nanoparticles in spleens isolated from different animals receiving either Nanotex (n=3), Endorem (n=2) or saline (n=1).

Nanotex accumulation was then investigated through the analysis of T2* relaxation in *ex vivo* spleens of CD1 mice one hour after the injection. Accumulation of the nanoparticles in this organ may cause a spleen failure and represent a clear symptom of toxicity. The resolution and sensitivity achieved with this *ex vivo* MRI method allows very precise measurements of T_{2*} in spleen, not achievable for the mouse spleen under *in vivo* conditions.

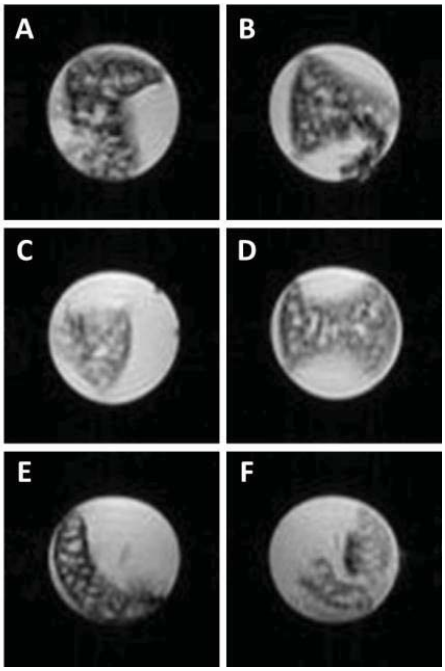

Figure 2.4. Splenic accumulation of different iron oxide nanoparticles as detected by T_{2*} weighted MRI. Six spleens (A-F) from mice, obtained one hour after the intravenous injection of Endorem (A, B), Nanotex (C, D, E) or saline (F). The doses of both contrast agents were 15 micromol Fe/kg body weight.

Figure 2.4 shows representative results of this study of Fe accumulation from injected nanoparticles in the spleen of two animals injected with

Endorem, three animals injected with Nanotex and a control. Note that the spleens from mice receiving Endorem or Nanotex appear darker than the control mouse receiving saline, as expected for nanoparticle accumulation. Moreover, the spleens receiving Endorem appear darker than those receiving Nanotex, revealing relatively lower accumulation of Nanotex than of Endorem.

Table 2.2 provides the quantitative T_{2*} values of isolated spleens before and one hour after intravenous injection of Nanotex or Endorem (15 micromol Fe/Kg body weight). Notably, Nanotex did not induce a significant decrease in splenic T_{2*}, suggesting a very low or non-existent splenic accumulation and negligible biological adherence. However, Endorem induce a decrease in splenic T_{2*} comparable with values measured with another commercial nanoparticle, Resovist (Schering, DE), which induces a splenic T_{2*} value of 2.11 ± 0.2 ms.

Table 2.2. Splenic accumulation of Nanotex and Endorem one hour after intravenous administration of the nanoparticles as detected by the splenic T_{2*} value.

Condition	Splenic T_{2*} (ms)[a)]
Control (saline)	4.78 ± 0.20
Nanotex	4.26 ± 0.26
Endorem	3.51 ± 0.16

[a)] T_{2*} values were determined *ex vivo*, at 7T (Bruker Pharmascan), using the gradient echo sequence in spleens isolated from CD1 mice either before or 1h after nanoparticle administration.

During the *in vivo* studies no appreciable external toxicity signs were observed after the administration of Nanotex, including the administrations of doses double than those recommended commercially. In addition, Nanotex was found compatible with the protocol of anaesthesia used (isoflurane 1-2%), without mortality detected due to the nanoparticle in any of the investigated healthy animals (n= 12).

More specifically, the administration of Nanotex did not induce significant changes in respiratory or heart rate, no external symptoms of hepatotoxicity such as yellowish fur, hair or eyes, bald spots,, hyper- or hypoactivity (sleepiness), aggressiveness, food and water intake disorders, hemiparesis or hemiplegia.

The residence time of the contrast agent in the body is another aspect that needs to be characterized in a new contrast agent. It is preferable a contrast agent with short residence time, being eliminated from the body rapidly, than a contrast agent with long residence time, thus disadvising repetitive accumulations.

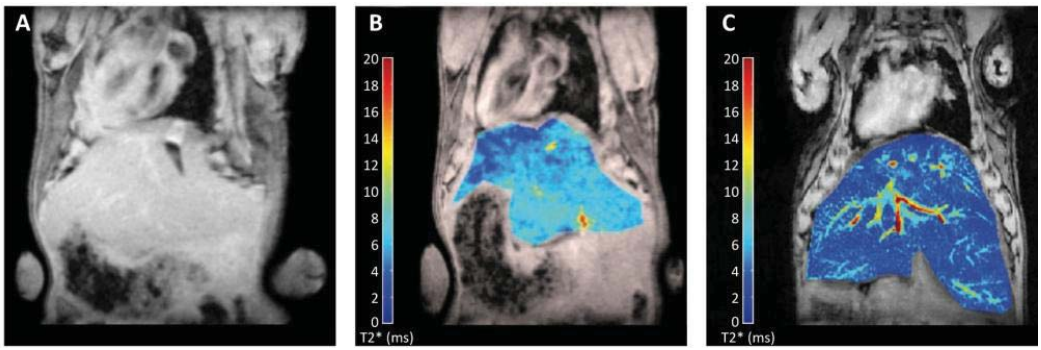

Figure 2.5. Representative T_{2*} MRI of mouse liver *in vivo* before (A) and after Nanotex (B) or Endorem (C) administrations. Representative T_{2*} weighted images (left) of thorax and abdomen of mice and T_{2*} maps obtained 24 h after intravenous administration of Nanotex (center) and Endorem (right) with a clinical doses of 15 micromol Fe /kg body weight.

Figure 2.5 shows representative T_{2*} weighted images across the abdomen and thorax of a control mouse before the administration of nanoparticle suspensions (left), or T_{2*} maps obtained 24 h after intravenous administration of the same dose of Nanotex (center) or Endorem (left). The T_{2*} map (Figure 2.5 center) shows significantly lower values of T_{2*} in the livers of animals treated with Nanotex or Endorem, confirming previous results.

Figure 2.6 summarizes the results of T_{2*} images acquired at different times after , after intravenous administrations of single dose (15 micromol Fe/kg body weight) and double dose (30 micromol Fe/kg body weight) of Nanotex, compared to those obtained after the administration of the same doses of Endorem. Nanotex induced a slight decrease in hepatic T_{2*}, with a fast decline followed by rapid clearance from hepatic tissue. Meanwhile, Endorem depicted a higher decrease in T_{2*} but a significantly slower clearance kinetics. Interestingly, the single dose of 15 micromol Fe/kg body weight Nanotex was cleared completely in approximately 24 hours with an approximately mean half-life ($t_{1/2}$) of hepatic elimination of 10 h. This mean half-life is significantly shorter than that of dextran coated nanoparticles as Endorem, revealing a lower vascular and tisular adherence and allowing for repetitive administration protocols at shorter time intervals.

Notably, the administration of Nanotex at a dose twice the one recommended (30 micromol Fe/kg body weight) demonstrated a significantly improved relaxation effect in the liver, only slightly smaller than that obtained with Endorem (15 micromol/Kg body weight), without appreciable changes in the rapid Nanotex elimination rate from liver.

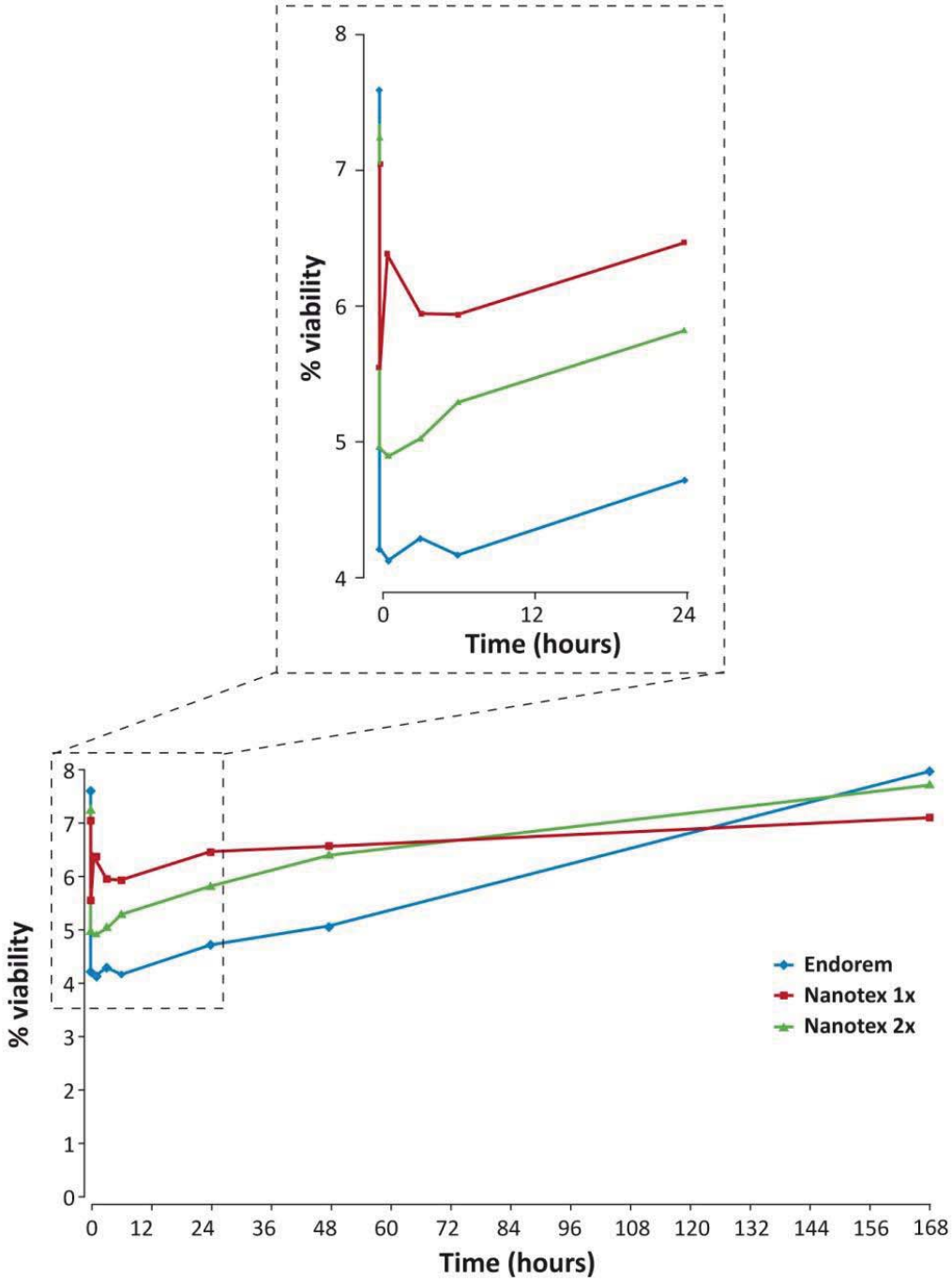

Figure 2.6. In vivo pharmacokinetics of hepatic clearance of Nanotex and Endorem after i.v. nanoparticle administrations. Relative changes in hepatic T_{2*} after injection of a single dose (15 micromol Fe /kg body weight) and double dose (30 micromol Fe/kg body weight) of Nanotex in the tail vein of mice are compared with those induced by Endorem (15 micromol Fe/Kg body weight). The results represent, mean and standard deviation of four animals investigated after administration of the contrast agent. The region between 0 and 6 hours is amplified in the insert for improved visualization of the enhancement effect.

Notably, the administration of the double dose showed no adverse symptoms and all mice survived the study.

In summary, we have shown that Nanotex depicts appropriate relaxation properties, lack of toxic effects and optimal pharmacokinetic properties improving those of Endorem. Taking together, these properties make Nanotex a very competitive superparamagnetic nanoparticle in comparison with the ones currently available commercially. However it remains important to demonstrate a specific application in MRI, where its advantages are more evidently proven in comparison with those of the earlier generation of paramagnetic and superparamagnetic nanoparticles. This is addressed in the next section.

2.3.3. Use of Nanotex in Perfusion Imaging

To this end we selected the MR imaging of tumoral perfusion, an advanced protocol used in the clinic with either gadolinium or iron based contrast agents. We set up the glioblastoma multiform model obtained after implantation of C6 cells, and investigated comparatively if Nanotex, Endorem and Gd(III)DTPA could provide improved information of the performance of the neoangiogenic vasculature of glioblastoma.

Figure 2.7 illustrates the determination of cerebral perfusion parameters using Magnevist, Resovist or Nanotex in rats carrying implanted C6 glial tumours. Briefly, the figure illustrates the fitting of the perfusion gamma function (red) to the kinetics of “bolus” passage of the different contrast agents (blue).

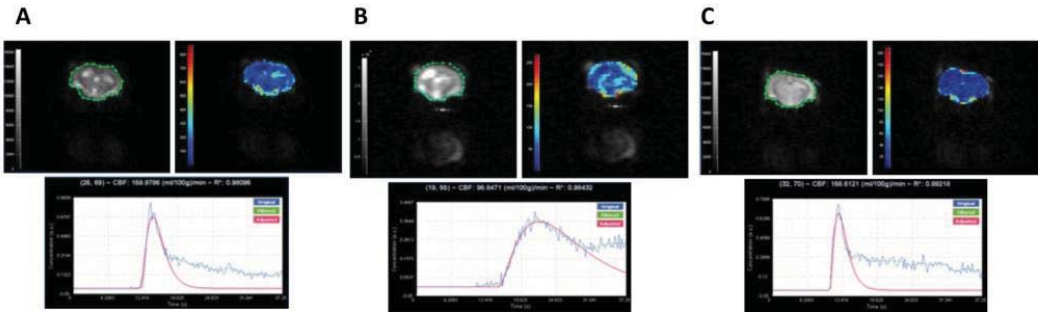

Figure 2.7. Comparative study of tumoral perfusion by the "bolus tracking" method in the C6 glioma model using paramagnetic or superpamagnetic agents. A: Gd(III) DTPA (Magnevist, Bayer, DE), B: Resovist (Bayer, DE) and C: Nanotex (Nanotex, ES).

Note that superparamagnetic Nanotex showed a similar behaviour to that of paramagnetic Magnevist, a behaviour not observed with the commercial superparamagnetic nanoparticle Resovist. Nanotex demonstrates a fast transit time and a virtually complete perfusion recovery after i.v. injection, revealing that Nanotex behaves similarly to Magnevist, does not remain fixed in the neovasculature as Resovist and does not adhere, nor significantly interacts with the endothelium of the glioma neovasculature.

Table 2.3 shows CBF [(ml/100g)/min], CBV (ml/100g) and MTT (s) values of Nanotex (15 micromol Fe/kg body weight) in the brain of rats carrying implanted C6 tumours, as calculated from the non-linear fittings to the gamma function representing the transit of the contrast agent. The results are compared with another nanoparticle, Resovist, and with Magnevist, a contrast agent based in Gadolinium chelates used as contrast agent in MRI.

Table 2.3. Cerebral perfusion parameters determined by the MRI bolus tracking method using Magnevist, Resovist or Nanotex (15 micromol Fe/Kg body weight).

	Value (mean±sd)[a)]		
Perfusion parameter	Nanotex	Magnevist	Resovist
CBF (mL/100g/min)	22.86±4.62	196.97±108.01	69.79±40.01
CBV (mL/100g)	1.41± 0.06	17.97±17.75	9.72±6.92
MTT (s)	3.55± 1.00	5.69±2.21	8.45±4.61

[a)] Perfusion values were determined *in vivo* at 7T (Bruker Pharmascan)from CD1 mice after the injection of Nanotex, Magnevist or Resovist bolus.

Nanotex depicted a shorter mean transit time in tissue than Magnevist and Resovist, probably due to the charged polyacrylic acid cover which avoid the aggregation of nanoparticles between them and with the capillary. Also, the cerebral blood volume is smaller for Nanotex indicating that this nanoparticle does not extravasculate from the blood to the surrounding tissue. On these grounds, Nanotex displays very favourable first passage kinetics and recovery through the cerebral microvasculature.

2.3.4. Use of Nanotex as Contrast Agent in CT images.

Due to the ferric nucleus we thought that Nanotex could be a good candidate as contrast agent in CT images. Figure 2.8 shows the results of the analysis of Nanotex as a X Ray contrast agent. To evaluate this fact, Nanotex was compared with a commercial X Ray contrast agent (Figure 2.8. A) finding that the signal produced by Nanotex was smaller than Ultravist. The posterior analysis with ImageJ indicates that Nanotex shows a signal enhancing effect but smaller than the commercial contrast agent Ultravist (Figure 2.8. B).

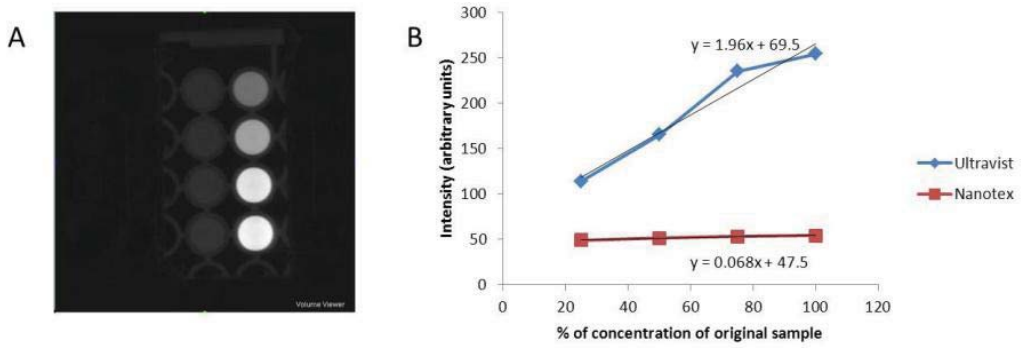

Figure 2.8. Comparison of Nanotex and Ultravist (Bayer Schering, DE) as CT contrast agents. X Ray images of different concentrations of Nanotex (A, left column) shows a contrast effect but lower than a commercial contrast agent, Ultravist (A, right column). B shows the values of intensity at different concentrations and the adjustment of data to a line showing the more intense effect of Ultravist as X-rays contrast agent.

2.4. Discussion

We developed a novel superparamagnetic nanoparticle for magnetic resonance imaging with an inorganic core diameter smaller than 15 nm and a negative surface electrical charge at neutral pH, two important features that contribute importantly to its intrinsic low vascular and tissular adherence *in vivo*. The combination of these properties determines an excellent pharmacokinetic profile with very reduced toxicity and optimal vascular transit times. The new nanoparticle shows only transient retention in the liver, without significant bioaccumulation, thus allowing repeated administration protocols, compatible also with the imaging of hepatic lesions. Reduced accumulation and efficient elimination may permit the frequent repetition of Magnetic Resonance

Imaging studies along time, at much short intervals than those required with currently available commercial [76, 77].

The lower tissue adherence of Nanotex, in comparison with Endorem or Resovist, merits further analysis. Since the iron core is very similar, the difference must necessarily rely in the polyacrylic acid coating. We believe this coating endows Nanotex with a negatively charged surface at neutral pH, favouring repulsion with other Nanotex particles and with the negatively charged phospholipid headgroups and proteins from the surface of endothelial cells. These repulsive interactions are not present in the commercial nanoparticles coated with dextran or cross-linked dextran, which easily adsorb over endothelial surfaces or interact with neighbouring particles most probably through hydrogen bonding. This non-specific interaction may favour the formation of aggregates of Resovist and Endorem with blood cells or within themselves, difficulting their passage through narrow capillaries, a circumstance that would not happen with the negatively charged Nanotex.

The comparison of the magnetic properties of Nanotex with commercial nanoparticles as Endorem or Resovist shows, however, less favourable r_1 and r_2 magnetic relaxivity properties for Nanotex [49]. Nevertheless, Nanotex T_2 relaxation remains adequate for excellent in vivo imaging of the liver and hepatic pathologies. Moreover, Nanotex r_{2*} relaxivity is improved with respect to the commercial nanoparticles, favouring an advantageous use of our nanoparticle with T_{2*} imaging based methods, such as perfusion MRI. In this sense, the excellent r2* values of Nanotex, add to its low adherence properties to configure very clean first passage kinetics, returning completely to baseline, a circumstance not observed

with commercial nanoparticles and only attainable previously with Gd(III)DTPA complex. This collection of properties makes Nanotex an ideal candidate to be used in tissue and tumoral perfusion assays *in vivo* with Magnetic Resonance Imaging, supporting a potential commercial development. A patent has been filed protecting the nanoparticle and its applications [78].

Chapter 3

Magnetoliposomes loaded with ω-3 Polyunsaturated Fatty acids as anti-inflammatory theragnostic agents

Chapter 3 describes the development of a new theragnostic formulation based in liposomes containing both, a ω-3 polyunsaturated fatty acid and an imaging biomarker. The efficacy of this new formulation is validated using a variety of imaging techniques and with different animal models of colonic inflammation and cancer. .

3.1. Introduction

Inflammatory lesions are associated to the most prevalent and morbid pathologies including atherosclerosis [79], neurodegeneration [80] diabetes or obesity [81] and cancer [82], among others. Decreases in the inflammatory phenotype are known to improve the disease progression and the patient´s quality of life, as well as to favour a better recovery [83]. With this aim, a variety of anti-inflammatory drugs have been proposed as adjuvant therapies for the different diseases, including mainly steroidal or non-steroidal treatments [84]. In all cases, anti-inflammatory therapies demand the use of relatively large doses of the active drugs and inevitably end up developing, sometimes too early, a collection of adverse secondary effects that preclude further treatment [85]. On these grounds, methods to improve the efficiency of anti-inflammatory drug delivery to the lesion, therefore increasing its selectivity and efficacy, entail considerable interest as well as potentially vast applications in a wide spectrum of diseases.

Liposomes have been proposed previously as novel nanotechnology formulations to improve drug delivery to a variety of inflammatory diseases [86, 87]. Targeting of the inflammatory region may be achieved using either active or passive approaches. Active targeting involves the use vectorial reagents embedded in the liposomal membrane that recognize epitopes of the target tissue [88]. Passive targeting refers to the passive accumulation of the liposomes in the inflamed regions because of their increased capillary permeability and limited clearance [89]. In both cases it becomes difficult to visualize if the liposomal preparation has arrived to the target tissue and many times, only indirect

measurements of inflammation provide an index of the anti-inflammatory effect. It would become then very useful, to visualize directly and non-invasively the presence of the drug loaded liposomes in the lesion. Liposomes are optimal structures for this purpose, since they can be prepared to contain in their lumen, in addition to the anti-inflammatory drug, a variety of imaging indicators either radioactive, fluorescent or superparamagnetic. This approach is known as image guided drug delivery [90], representing currently the most promising strategy to diagnose and treat inflammatory diseases.

Recently, important anti-inflammatory effects have been reported using preparations of omega-3 fatty acids [91-94], a kind of long chain polyunsaturated fatty acids (PUFAs) mainly present in fish oil and used as dietary supplements. Omega-3 PUFAs allow prolonged anti-inflammatory treatments without the appearance of the deleterious secondary effects of alternative steroidal or non-steroidal drugs [95].

In this chapter we report a successful protocol to encapsulate ω-3 polyunsaturated fatty acid ethyl ester (PUFA-EE) in liposomal preparations containing, in addition, either the Nanotex superparamagnetic nanoparticle or the rhodamine-100 dye. These advanced theragnostic preparations maintain in its integrity the therapeutic potential of free ω-3 PUFA-EE, potentiated with important multimodal imaging capabilities. We demonstrate their anti-inflammatory effects *in vivo*, in animal models of colonic and oncologic inflammation.

3.2. Materials and Methods

3.2.1. Preparation and Characterization of Liposomes

Lipid hydration and extrusion method

Liposomes were prepared essentially using the film hydration method [96]. Briefly, 20 mg of L-α-phosphatidylcholine (Avanti Polar Lipids Inc., Alabaster, Alabama, USA) were dissolved in 2 mL of chloroform (Merck, Darmstad, DE). The solution was placed in a round flask and subjected to rotary evaporation (Heindolph Instruments, Schwabach, DE) for sixty minutes, 280 rpm, 474 mBar and 40 ^{0}C. The lipid film formed after chloroform evaporation was further rotated under the same conditions to remove chloroform traces. Then, the dried lipid lecithin film was rehydrated with 5 mL of water (containing or not the active principle or imaging probe) and rotated 60 minutes at atmospheric pressure and 50 ^{0}C. This process generates a heterogeneous suspension of liposomes of different sizes containing or not the active principles and imaging probes in their lumen as delivered with the hydration buffer. To homogenize the size distribution, the liposomal suspension was extruded eleven times (Northen Lipids, Burnaby, CAN) under nitrogen pressure through a 200 nm membrane (Whatman, GE Healthcare, Fairfield, Connecticut, USA) maintaining the temperature at 50 ^{0}C. The resulting suspension containing homogenous liposomes, loaded or not with the selected imaging agent and ω-3 PUFA-EE, was stored at 4 ^{0}C until further utilization. A schematic description of the process can be seen in Figure 3.1.

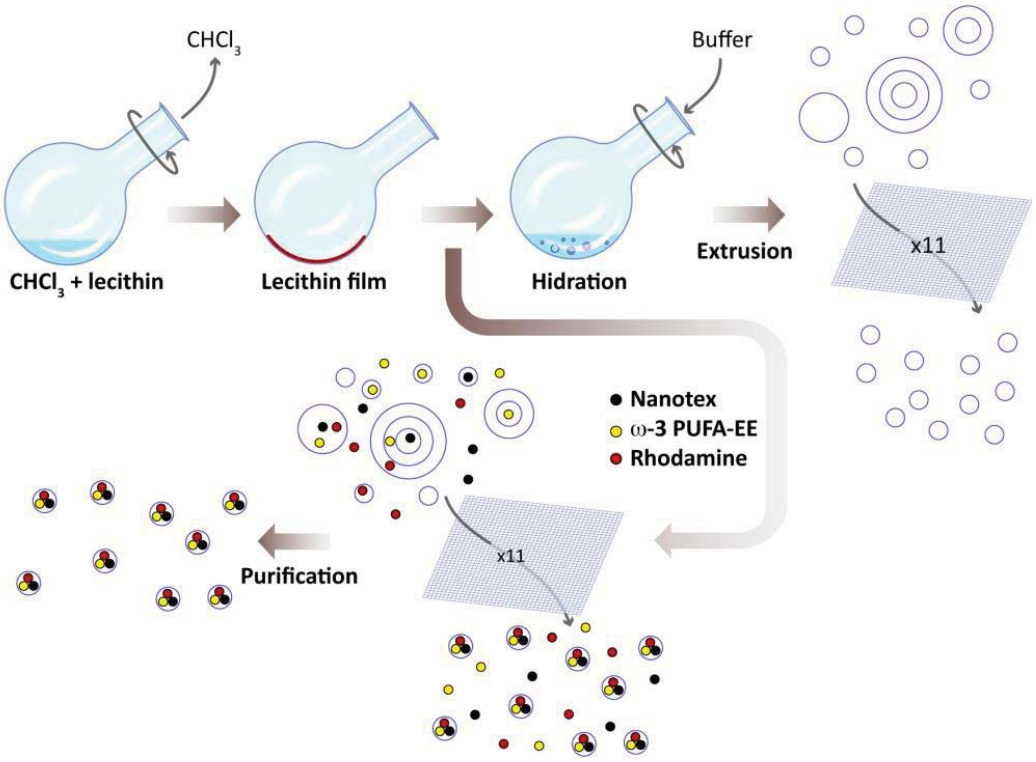

Figure 3.1. Preparation of liposomes. Liposomes are prepared from egg yolk lecithin, containing or not ω-3 PUFA-EE, Nanotex or rhodamine-100 by the film hydration method [96]. A solution of chloroform and lecithin is rotated under vacuum to remove chloroform and deposit a thin lecithin film covering the round bottom flask. Hydration of this film with aqueous buffer results liposomes of different sizes and different number of layers. Nanotex, ω-3 PUFA-EE or rhodamine-100 may be added to the buffer, resulting in their intraluminal encapsulation after liposomal formation. Some residual Nanotex, ω-3 PUFA-EE or rhodamine-100 may remain in the extraliposomal space. Repeated extrusions (x11), result in crude homogeneous suspensions of liposomes loaded or not with added components in their lumen, but also present in the extraliposomal space. These may be removed later after a purification process, normally based in size exclusion chromatography or differential centrifugation through filters of controlled pore size.

We prepared liposomes encapsulating either suspensions of (i) buffer alone, (ii) Nanotex (25 mg Fe/mL, Solutex S.L., Alcobendas, ES) as MRI detectable probe, (iii) Nanotex and ω-3 PUFA-EE (0.1% aqueous volume, Solutex S.L., Alcobendas, ES) as theragnostic anti-inflammatory agents detectable by MRI, or (iv) Nanotex with rhodamine-100 chloride (10

mg/mL, Sigma Aldrich, Barcelona, ES) as a novel agent detectable by hybrid fluorescence and MRI.

Transmission Electron Microscopy

Transmission electron microscopy (TEM) images were acquired in a JEOL JEM1010 100 kV (JEOL Ltd., Tokyo, JAP) from samples of empty liposomes, Nanotex and liposomes loaded with Nanotex, stained with uranil acetate [97].

Dynamic Light Scattering

The size of liposomes was measured by Dynamic Light Scattering (DLS, DynaPro MS/X (Wyatt Inc., Dernbach, DE) essentially as described in refs. [98, 99]. A dilution 1:10 of the original samples in water was placed in a quartz cuvette inside the apparatus to perform the light scattering measurement. Several dilution steps of the original sample were necessary to allow for appropriate intensity of light scattering profile in the sample. The presence of Nanotex in the preparations hampered light scattering measurements in the corresponding preparations, most probably due to the high optic density and reflectance of the solution.

^{1}H High Resolution Magic Angle Spinning (HRMAS)

^{1}H HRMAS spectroscopy was performed using a Bruker Avance 11.7 T instrument equipped with a High Resolution Magic Angle Spining (HRMAS) accessory, interfaced with a Linux driven Paravision IV console (Bruker BIOSPIN, Ettlingen, DE). Briefly, samples were dissolved in 25 µL deuterated water (99.2% ^{2}H, Apollo Scientific Limited, Stockport, UK) or deuterated chloroform (99.8%, Scharlau, Barcelona, ESP) containing 1mM TSP (trimetil sylil 2, 2', 3, 3' tetradeutero sodium propionate) or 1

mM TMS (tetramethyl silane, Scharlau, Barcelona, ES) used as chemical shift references, placed in 50 µL zirconium rotors and inserted in the rotating probe adapted to the magnet. Water suppressed ^{1}H HRMAS spectra ($4^{0}C$, 4000 Hz) were acquired using the Carr-Purcell-Meiboom-Gil sequence with $\pi/2$ pulses, spectral width of 10 kHz, acquisition time of 0.41 sec, D1= 1 sec, 72 π pulses with a separation time τ = 1 ms and processed using 1 Hz exponential line broadening applied in the time domain prior to Fourier Transformation [68].

HRMAS DOSY (Diffusion-Ordered NMR Spectroscopy) spectra of liposomes were acquired in a Bruker AVANCE III of 400 MHz (Bruker BIOSPIN, Ettlingen, DE) using a ^{1}H selective probe and NMR tubes of 5mm. The spin-echo Stejsktahl-Tanner sequence, was used with diffusion intervals of 20, 50 and 100 ms and diffusion gradient strengths from 2% to 95% of the maximal power of the Z gradient (sixteen increments) [68].

Water Relaxivity Measurements

We investigated the effect of magnetoliposomes on the T_1 and T_2 magnetic relaxation properties of the water molecules of the suspension, to assess their potential usefulness as imaging agents for MRI detection. T_1 and T_2 relaxation times of magnetoliposomes were investigated in two different liposomal samples, containing or not the superparamagnetic particle Nanotex (0.5 mg/mL). Dilutions of the original suspensions to 50% and 25% of the initial concentration were used to generate the relaxation vs. concentration profiles. Briefly, T_1 and T_2 values of all samples (37 ^{0}C) were measured using the inversion recovery sequence or Carr-Purcell-Meiboom-Gill (CPMG) sequences using a Bruker Minispec 1.5 Tesla (Bruker BIOSPIN, Ettlingen, DE) [67].

Fluorescence Properties

We investigated the fluorescent properties of magnetoliposomes labeled with rhodamine-100 chloride both *in vitro* and *in vivo* using an *in vivo* IVIS-Lumina system (Perkin Elmer, Waltham, Massachusetts, USA) [100]. *In vitro* and *in vivo* fluorescence images were acquired using a Green Fluorescent Protein filter (GFP, excitation bandpass 445-490 nm, emission bandpass 515-575 nm) and sixty seconds exposition. For the *in vitro* studies, three samples of liposomes containing or not the nanoparticle (25 mg Fe/mL) and the fluorescent dye (10 mg/mL), at different concentrations (18.75 mg Fe/mL, 12.5 mg Fe/mL, 6.25 mg Fe/mL for the nanoparticle and 7.5 mg/mL, 5 mg/mL, 2.5 mg/mL for rhodamine-100) were placed in 96-well plate and scanned. For the *in vivo* studies, CD1 adult mice (30g body weight) were anesthetized in a ventilated chamber with a mixture of oxygen and isofluorane (2%, Isoflo, Esteve, Barcelona, ES) and maintained on it during the scanning period. Images were acquired as indicated above, before and after the i.p. injection (200 μL) of the liposomal preparations.

Ultrafiltration by Centrifugation

The ultrafiltration method separates the sample in two fractions, sediment and ultrafiltrate, by forcing the sample to pass through a filter of controlled pore size, using centrifugal force. For this purpose, we use molecular size filters with a pass of 300 KDa (Vivaspin 6, MWCO 300 KDa, Vivaproducts, Littleton, MA, US). The centrifuge used was J-6B (Beckman Coulter, L'Hospitalet de Llobregat, ES) with centrifugation conditions of 2891 g (3900 rpm, 20 ^{0}C, 1 hour). After the centrifugation, the absorption spectra (200 – 600 nm) of the sediment and the ultrafiltrate was

analysed using multiwall plates in a vertical spectrofluorimeter (Synergy, Biotek, Winooski, VT, US).

3.2.2. In vivo evaluation of anti-inflammatory activity

Animal Models of Inflammation and Experimental Design

All animal protocols were approved by appropriate institutional review panels and follow the guidelines of National advisory bodies in animal welfare.

A convenient model of colonic inflammation was induced in C56BL6 mice through the administration of Dextran Sulfate sodium salt (DSS, Leti, Barcelona, ESP) dissolved (3.5%) in the drinking water during 5 days [101]. Briefly, three groups of mice (n=6) received DSS treatment for five days and were injected in the tail vein (100 µL) with Phosphate Buffered Saline (Group 1), Magnetoliposomes (Group 2) and Magnetoliposomes containing ω-3 PUFA-EE (Group 3) during the first three days. The body weight evolution was followed in each mouse until the fifth day when the animals were investigated by MRI. For this purpose, mice were injected i.p. with 100 µL of Gd(III)DTPA (0.1M) just before coronal T_1 images were acquired from the rectal zone of each mouse. Colonic inflammation was measured by the width of the rectal wall. After the MRI experiment, the administration of DSS was stopped and normal drinking water was administered to all mice, following their weight until 10^{th} of study.

The model of oncologic inflammation was induced in CD1 mice through the stereotaxic implantation of approximately 10^6 C6 glioma cells in the caudate nucleus of the mouse brain [102]. Fifteen days after the implantation the tumor had proliferated reaching sizes ranging from 0.5

to 1.5 cm. Two different treatments were investigated in mice 15th days after the implantations: a first group (n=6) received Magnetoliposomes with ω-3 PUFA-EE and another group (n=6) Magnetoliposomes without fatty acids ester. We investigated additionally a control group (n=6) that received no treatment. Treatments were administered intravenously (unique doses of 100 μL) and the growth of the glioblastoma was monitored by MRI obtaining images weighted in T_1 and T_2.

Magnetic Resonance Imaging

All MRI examinations were performed using a 7 Tesla horizontal magnet (16 cm bore) interfaced with a Bruker AVANCE III radiofrequency console operated through a Linux platform running Paravision V software.

The colon inflammation model was explored with T_1 images using a Multi Slice Multi Echo (MSME) sequence, TE=10.643 ms, TR=521 ms, 3 averages, axial orientation, 22 slices, slice thickness 1.5 mm, interslice distance 1.5 mm, field of view 3.8 cm.

The glioma model was investigated with T_1 and T_2 images. T_2 images were acquired using a Rapid Acquisition with Relaxation Enhancement (RARE) sequence, TE=14.77 ms, TR=2500 ms, 6 averages, axial direction, 14 slices, slice thickness 1 mm, interslice distance 1 mm, field of view 2.3. T_1 images were acquired using a Multi Slice Multi Echo (MSME) sequence, TE=10.643 ms, TR=350 ms, 3 averages, axial direction, 14 slices, slice thickness 1 mm, interslice distance 1 mm, field of view 2.3 cm.

T_1 images were always obtained after the i.p. administration of 100 μL of Gd(III)DTPA (0.1M, Magnevist, Bayer Schering, Berlin, DE) to enhance T_1 contrast.

Positron Emission Tomography

The evolution of colonic inflammation was also followed by PET/CT. The images were taken in a trimodality scanner Inveon (Siemens AG, DE). ^{18}FDG (11 MBq doses) was administered forty five minutes before the CT and PET images were acquired to visualize the distribution of the isotope. For the PET acquisition, we acquired 159 interferograms of 128 x 128 pixels (pixel spacing 0.77 mm, slice thickness 0.796 mm) in a FOV of 83x130mm. The acquisition lasted fifteen minutes and the reconstruction algorithm used was the OSEM2D method with four iterations and correction by decay and scattering. The CT images were taken with a voltage of 80 kV and a current of 500 µA. The exposure time was 250 ms, acquiring 180 projections with a FOV of 83x130 mm. The SUV (standardized uptake value) value was determined with the corrections for isotope decay and animal weight.

Statistical Analysis

Comparisons used the mean and standard deviation of all data from each group and the t-student test to assess significance ($p<0.05$). Statistical analysis was done using SPSS software (IBM, New York, NY, US).

3.3. Results

3.3.1. Dynamic Light Scattering and Transmission Electron Microscopy

The process of liposomal preparation originates a suspension of liposomes with homogenous size. This size was determined experimentally by Dynamic Light Scattering (DLS) and Transmission Electron Microscopy (TEM) techniques.

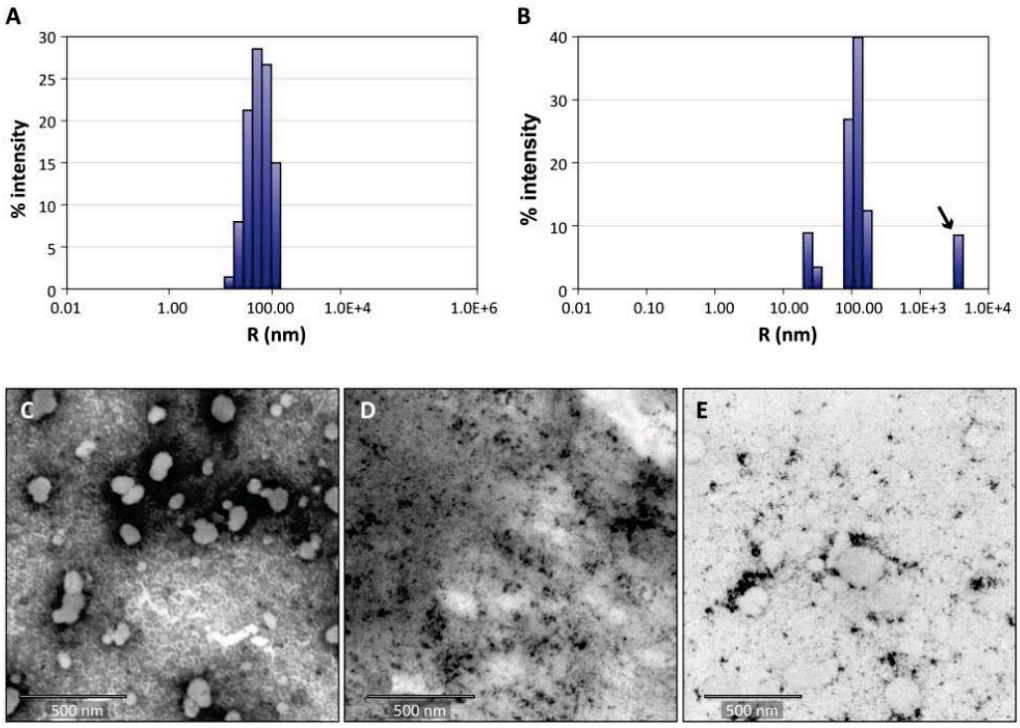

Figure 3.2. Determinations of liposomal size. Top panels: DLS of a suspension of empty liposomes (A) and a suspension of liposomes loaded with ω-3 PUFA-EE (B). Arrows indicate the size of larger aggregates of free ω-3 PUFA-EE (black), eventually moving to the surface of the preparation because of their lower density. Some nanometric goticules of ω-3 PUFA-EE (blue) are observed transiently. Bottom panels shows TEM images of empty liposomes stained with uranyl acetate (C), free Nanotex superparagmagnetic nanoparticle (D), and liposomes loaded with Nanotex (E). Note the presence of extraliposomal Nanotex nanoparticles prior to final purification.

Figure 3.2 (top) shows representative results of size measurements in liposomal preparations containing (2B) or not (2A) ω-3 PUFA-EE as performed with DLS. DLS analysis of liposomes without ω-3 PUFA-EE showed 200 nm diameter vesicles, corresponding well with the 200 nm filter used in the extrusion. The liposomal preparations containing ω-3 PUFA-EE showed, in addition to the expected 200 nm liposomal particles, larger particles of approximately 7000 nm. These particles accumulated, at least partially, with time at the top of the preparation as a lipid layer, and were assigned to non-encapsulated ω-3 PUFA-EE aggregates that piled in the top of suspension and could be easily removed from the preparation before further use. Smaller size goticules of approximately 20-30 nm could also be detected by DLS, but disappeared with time, merging with others and migrating to the surface. The size of the liposomes loaded with Nanotex could not be measured with the DLS technique, since the nanoparticle demonstrated a high degree of reflectance incompatible with the size measurement. We investigated then the size of these preparations using TEM (Figure 3.2, bottom panels). Fig 2C-E show TEM images of empty liposomes, the nanoparticle Nanotex only and liposomes containing Nanotex, respectively. Empty liposomes (150-200 nm) required uranil acetate shadowing to become observable by TEM (2C), while Nanotex (7-8 nm diameter) was directly observable. Liposomes loaded with Nanotex (150-200 nm) showed also appreciable amounts of the superparamagnetic nanoparticle in the extraliposomal space.

3.3.2. Magnetic Resonance Spectroscopy

A brief study of the characteristics of the ω-3 PUFA-EE used became necessary to elucidate the nature of its incorporation into the liposomes. To this end we investigated the properties of ω-3 PUFA-EE using Magnetic Resonance Spectroscopy.

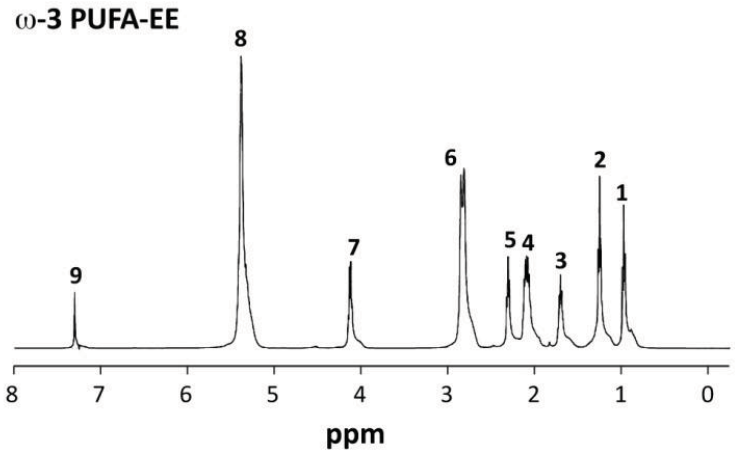

Figure 3.3. ^{1}H HRMAS spectrum (500.13 MHz, 22 ^{0}C, 4000 Hz) of ω-3 PUFA-EE in deuterated chloroform. Assignments in Table 3.1.

Figure 3.3 shows representative ^{1}H HRMAS spectra from a chloroform suspension of ω-3 PUFA-EE, acquired as indicated in Methods. The spectrum shows clearly resolved resonances from the magnetically different protons of the ω-3 PUFA-EE as specified in Table 3.1. It became possible to assign all observed resonances [103, 104].

Once the ^{1}H HRMAS spectrum of ω-3 PUFA-EE was well characterized, it became possible to compare it with the spectrum of empty liposomes and liposomes containing ω-3 PUFA-EE.

Table 3.1.Assigments of ω-3 PUFA-EE resonances indicating the proton group and the corresponding chemical shift.

Resonance	Original protons	ppm[a)]
1	-CH_2-C**H_3**	0.96
2	C**H_3**-CH_2-OOC-R	1.25
3	CH_3-CH_2-CH=C**H**-CH_2-	1.69
4	=CH-C**H_2**-CH_2-CH_3	2.08
5	=C**H**-CH_2-CH_3	2.30
6	-OOC-C**H_2**-	2.83
7	-(C**H_2**)$_p$-(CH=CH)$_m$-(C**H_2**)$_n$-	4.11
8	-(CH_2)$_p$-(C**H**=C**H**)$_m$-(CH_2)$_n$-	5.37
9	Deuterated chloroform	7.28

[a)] Chemical shifts refereed to the deuterated chloroform diluted in the sample.

Figure 3.4 shows representative HRMAS spectra from liposomal suspensions containing (bottom) or not (top) ω-3 PUFA-EE. Note that the bilayer membrane structure of the liposomes precludes the observation of most resonances from the fatty acid chains. This is due to insufficient motional averaging in the NMR timescale because of the restrictions imposed by the bilayer structure of the membrane [105]. Interestingly, only resonances from the choline head group at 3.2 ppm and some methylene resonances from the fatty acyl chains (at 2.9 ppm) are sufficiently mobile to originate observable resonances in the empty liposomal preparation. Interestingly, resonances typical for the PUFA-EE (cf. Figure 3.3) can be easily distinguished in the preparation of liposomes containing fatty acids ester (bottom panel), revealing the incorporation of the fatty acid into the liposome, in a sufficiently mobile form to originate a high resolution NMR resonance.

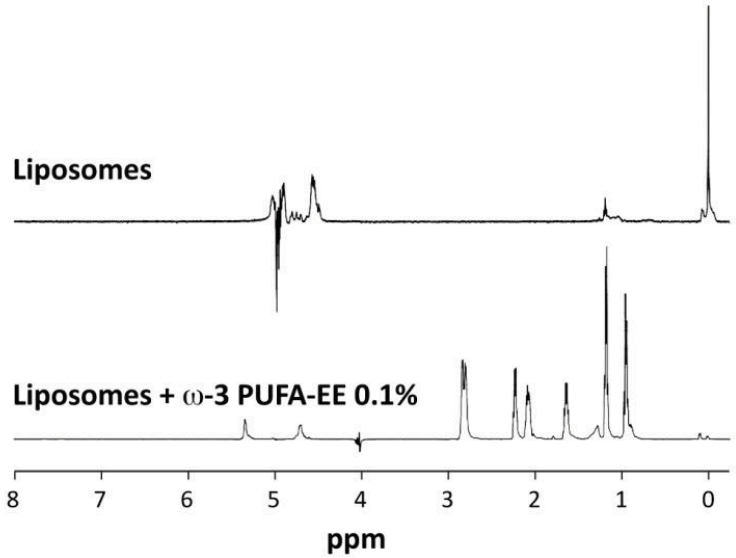

Figure 3.4. ^{1}H HRMAS (550.13 MHz, 4 ^{0}C, 4000 Hz) spectra liposomal preparations. Spectra of aqueous suspensions from empty liposomes (top) and from liposomes loaded with ω-3 PUFA-EE (bottom). Note that the spectrum of the liposomal suspensions loaded with ω-3 PUFA-EE is dominated by the resonances from the more mobile lipid droplets from ω-3 PUFA-EE.

In particular, the methyl groups (resonance 1 of Table 3.1), the methylene group vicinal to the carboxylic group (resonance 7 of Table 3.1) and the methyl groups corresponding to ω-3 PUFA-EE can be clearly resolved in the corresponding liposomal preparation. The observation of these resonances cannot be due to the incorporation of the fatty acid in the liposomal membrane, which would result in an almost complete immobilization of the molecule and disappearance of its high resolution NMR signals. Rather, these ω-3 PUFA-EE reveal the presence of sufficiently small fatty acid goticules in the liposomal preparation, able to originate high resolution signals through motional narrowing. This is confirmed by the DLS measurement (Fig. 3.2.b) which reveals the presence of sufficiently small PUFA-EE nanoparticles of approximately 30 nm diameter. However, either the ^{1}H HRMAS or DLS results do not reveal

if the ω-3 PUFA-EE goticules are present in the intraluminal space of the liposome, in the extraliposomal space of the suspension, or in both.

To investigate this aspect we performed Diffusion Weighted Spectroscopy experiments (DOSY) [106]. This approach measures the Apparent Diffusion Coefficient of water (ADC) in the liposomal preparation. According to the Einstein´s principle the ADC is inversely proportional to the number of molecular obstructions that the water molecule would find along its random mean diffusional path [107]. The measurement of ADC is dominated by the contribution of the extraliposomal volume and if goticules would be present there at a significant proportion, one would expect a decrease in the observed ADC. In contrast, if goticules would be located inside the liposomes, no additional obstructions would be found in the extraliposomal volume and very similar ADC´s would be measured in the presence and absence of ω-3 PUFA-EE.

Figure 3.5 shows the results of DOSY measurements of water diffusion in liposomal suspensions containing or not PUFA-EE. No significant differences can be observed in the water ADCs values between both preparations at the three diffusion times, suggesting that the fatty acids ester droplets do not increase significantly the molecular obstructions to water movements. Since the ADCs are primarily dominated by those of the extraliposomal volume, present results suggest that most PUFA-EE goticules are localized in the intraluminal space or associated somehow to the membrane of the liposomal preparations.

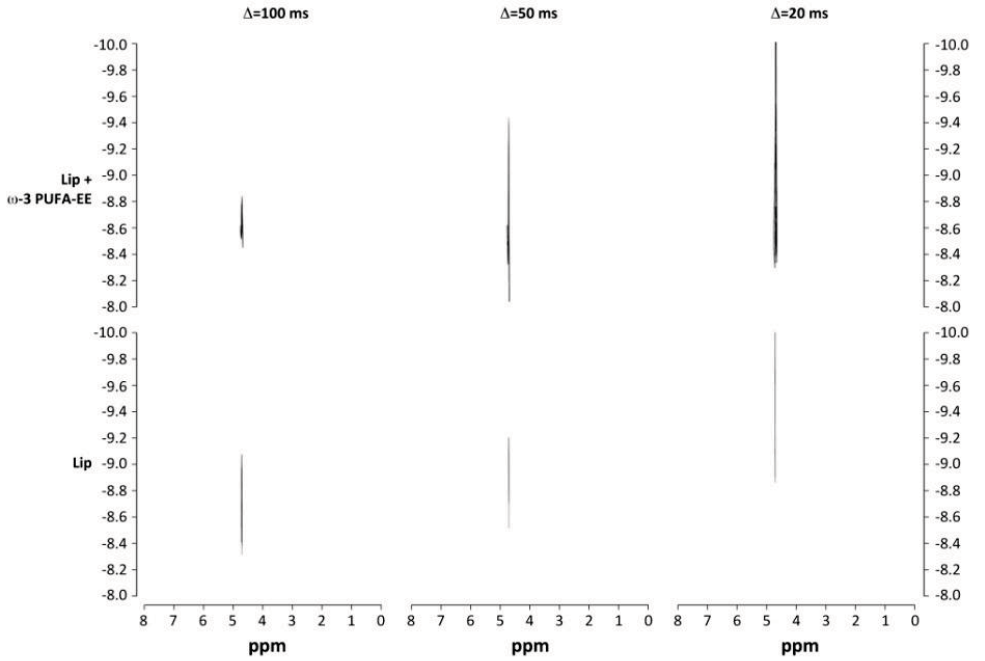

Figure 3.5. ^{1}H HRMAS DOSY (400,7 MHz, 22 ^{0}C) spectra of water diffusion in liposomal suspensions. Spectra were acquired in suspensions of liposomes loaded (top panels) or not (bottom panels) with ω-3 PUFA-EE, acquired with diffusion times of 100 ms (left), 50 ms (center) and 20 ms (right). Note that the presence of ω-3 PUFA-EE does not decrease significantly the water ADC, suggesting primarily an intraluminal location of the goticules.

This could be demonstrated by the ultrafiltration experiments in which the goticules of ω-3 PUFA-EE suspensions passed easily and quite completely the 300 kD filters, while the suspensions of liposomes containing ω-3 PUFA-EE did not appreciably passed through filters of the same dimensions. This confirmed that ω-3 PUFA-EE goticules are predominantly intraliposomal as indicated by the water ADC measurements.

3.3.3. Magnetic Relaxation Properties of Liposomal Preparations

We investigated the T_1 and T_2 magnetic relaxation properties of water molecules in suspensions of liposomes, containing or not Nanotex. Tables 3.2 and 3.3. summarize these results.

Table 3.2. T_1 values of different preparations (0.5mg Fe/mL, 0.25 mg Fe/mL and 0.125 mg Fe/mL) of liposomal suspensions containing or not Nanotex.

Suspension type / concentration	T_1 (ms)[a)]		
	0.5 mg/mL	0.25 mg/mL	0.125 mg/mL
Liposomes without nanoparticles	2161.7 ± 154.6	2207.3 ± 107.9	2955.0 ± 7.1
Liposomes whit nanoparticles	17.373 ± 0.006	34.17 ± 0.06	64.1 ± 0.1

[a)] T_1 values were determined at 1,5 Tesla (22^0C, Bruker Minispec, Rheinstetten, DE) using the inversion recovery sequence.

Table 3.2 shows the values of T_1 water relaxation time in liposome suspensions containing or not Nanotex in three successive dilutions of the maximal initial concentration. It can be observed that the T_1 relaxation value is shortest for the higher Nanotex concentration and increases approximately linearly when suspensions are diluted, giving a relaxivity value r_1 of 6.26 $mM^{-1}{\cdot}s^{-1}$. The same situation is observed with empty liposomes, albeit with a much slope for the increase in T_1 relaxation due to the absence of the superparamagnetic nanoparticle.

Table 3.3. T_2 values of different preparations of liposomes with and without Nanotex (0.5mg/mL and solutions diluted to 50% and 25% of its initial concentration).

Suspension type / concentration	T_2 (ms)[a)]		
	0.5 mg/mL	0.25 mg/mL	0.125 mg/mL
Magnetoliposomes without nanoparticles	1138.3 ± 34.6	1034.3 ± 6.1	2228.2 ± 0.14
Magnetoliposomes whit nanoparticles	1.717 ± 0.006	3.48 ± 0.006	6.637 ± 0.015

[a)] T_2 values were determined at 1.5 Tesla (22 ^{0}C, Bruker Minispec, Rheinstetten, DE) using the inversion recovery sequence.

Table 3.3 shows T_2 relaxation results of the different samples. T_2 values for the original sample with Nanotex shows approximately 1000 times faster relaxation than the empty liposomes (Table 3.2). It can be observed that the T_2 relaxation value is shortest for the highest Nanotex concentration and increases approximately linearly when suspensions are diluted, giving a relaxivity value r_2 of 64.6 $mM^{-1}.s^{-1}$. The same situation is observed with empty liposomes, albeit with a much lower increase of T_2 relaxation upon dilution.

3.3.4. Fluorescence *in vitro* and *in vivo*

The capacity of liposomes as optical biomarkers was tested using *in vitro* and *in vivo* fluorescence approach. Figure 3.6 summarizes the results obtained *in vitro* and *in vivo* with liposomes containing or not Nanotex, and labeled fluorescently with rhodamine-100.

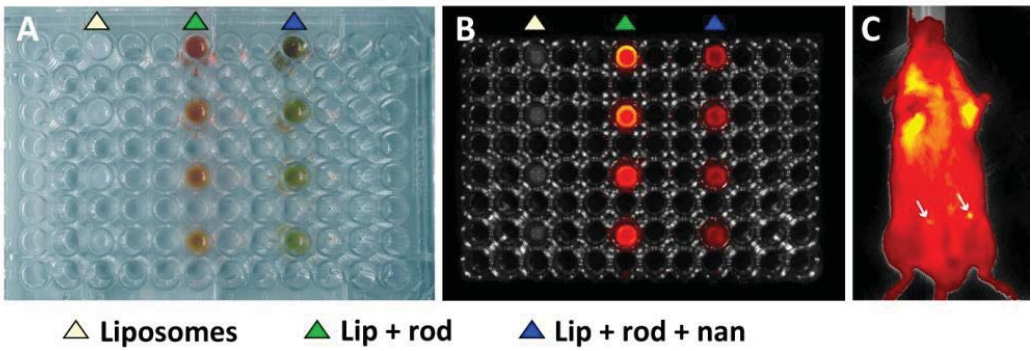

Figure 3.6. Fluorescence imaging of liposomes. *In vitro* (A, B) and *in vivo* (C) fluorescence images of liposomes loaded with nanoparticles and rhodamine-100 as acquired with the IVIS-Lumina camera. A: Visible picture of the 96 well plate used as phantom, showing the columns of wells loaded with decreasing (top to bottom) concentrations of empty liposomes (left column), liposomes loaded with rhodamine-100 (central column) and liposomes loaded with rhodamine-100 and Nanotex (right column). B: Fluorescence image. Note the larger fluorescence of the liposomes containing rhodamine-100 only as compared to those containing rhodamine-100 and Nanotex. C: *In vivo* images reveal the presence of the liposomal preparations injected i.p., arrow left: liposomes containing rhodamine-100 and Nanotex, arrow right: empty liposomes.

Figure 3.6A–B shows results obtained in the *in vitro* fluorescence experiment, comparing the fluorescence of empty liposomes (left track), liposomes containing rhodamine-100 (central track) and liposome containing rhodamine-100 and Nanotex (right track). Liposomes containing only rhodamine-100 present more fluorescence than liposomes containing both rhodamine-100 and nanoparticles. This may be due to either or both of two circumstances. First, liposomes with Nanotex have to share their lumen space with rhodamine-100 and one or more nanoparticles, resulting in a smaller intraluminal volume for rhodamine-100 accumulation and thus decreased rhodamine-100 concentration. Second, Nanotex could partially quench the fluorescence of rhodamine-100.

Figure 3.6C shows the results of a representative *in vivo* experiment in a mouse receiving an i.p. injection of liposomes labeled with rhodamine-100 containing (left side) or not (right side) Nanotex. As in the *in vitro* experiments, liposomes with Nanotex and rhodamine-100 depict less quantum efficiency than liposomes with only rhodamine-100, but they still become observable by *in vivo* fluorescence (Figure 3.6C). In this respect, the *in vivo* detection of magnetoliposomes with rhodamine-100 in their lumen may open new ways in theragnostic methods using multimodal imaging detection combining MRI and fluorescence imaging.

3.3.5. Anti-Inflammatory Effects *in vivo* in a Mouse Model of Colonic Inflammation

We investigated the anti-inflammatory effects of liposomal preparations containing or not ω-3 PUFA-EE using a well-established model of colonic inflammation induced by dextran sulfate (sodium salt, DSS) administration.

Figure 3.7 shows representative results of the administration of magnetoliposomes with and without ω-3 PUFA-EE in mice with rectal inflammation induced by DSS. Untreated mice (3.7A) or those treated with magnetoliposomes without ω-3 PUFA-EE (3.7B) showed clearly increased colonic wall thickness, easily observable in T_1w images after Gd(III)DTPA enhancement. However, mice treated with magnetoliposomes containing ω-3 PUFA-EE (3.7C) depicted a significant reduction in colonic wall thickness, revealing an important anti-inflammatory effect of the theragnostic preparation in the DSS model.

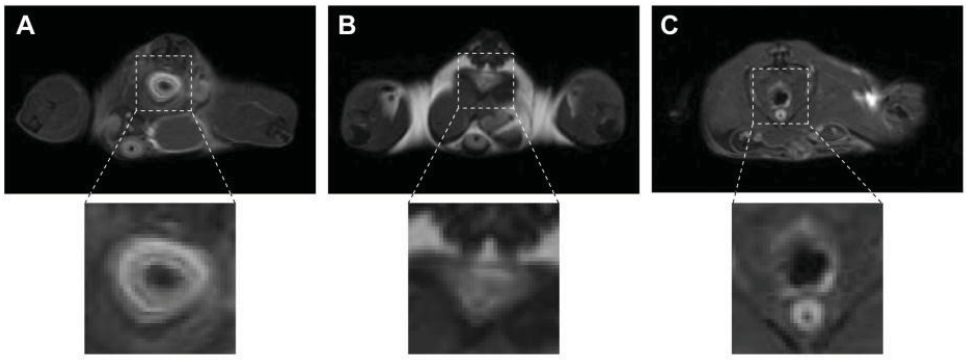

Figure 3.7. T_{1w} MR Images of colonic inflammation in the rectal region of mice subjected to DSS administration for five days. A: untreated, B: treated with liposomes containing Nanotex and C: treated with liposomes loaded with Nanotex and ω-3 PUFA-EE.

These results are summarized in Table 3.4. The therapeutic effects of ω-3 PUFA-EE became even detectable in the DSS model by measuring the weight of the animals along the DSS treatment and several days later.

Table 3.4. Rectal wall thickness of different groups treated with DSS.

Condition	Wall width (mm)[a)]
PBS	0.69±0.13
Magnetoliposomes without fatty acids SOLUTEX	0.43±0.17
Magnetoliposomes with fatty acids SOLUTEX	0.27±0.05[b)]

[a)] The width of the rectal of CD1 mice was measured with ImageJ in T_{1w} images obtained in a 7T magnet.
[b)] $p<0.05$

Notably, untreated mice or mice treated with magnetoliposomes without ω-3 PUFA-EE showed significant decreases in body weight, while mice treated with magnetoliposomes containing ω-3 PUFA-EE maintained their initial body weight along the treatment period, revealing a potent anti-inflammatory effect of the formulation.

We further investigated the effects of our liposomal preparations in the DSS model of colonic inflammation, using ^{18}F FDG and PET-CT techniques. Figure 3.8 shows representative results of four different animal groups including a control without any treatment, an animal receiving a saline placebo treatment, and animals receiving magnetoliposomal preparations containing Nanotex with or without PUFA-EE. Colonic ^{18}FDG uptake is observed in all animals. This uptake appears to be, however, higher in animals without liposomal treatment than in animals treated with magnetoliposomes either with or without PUFA-EE.

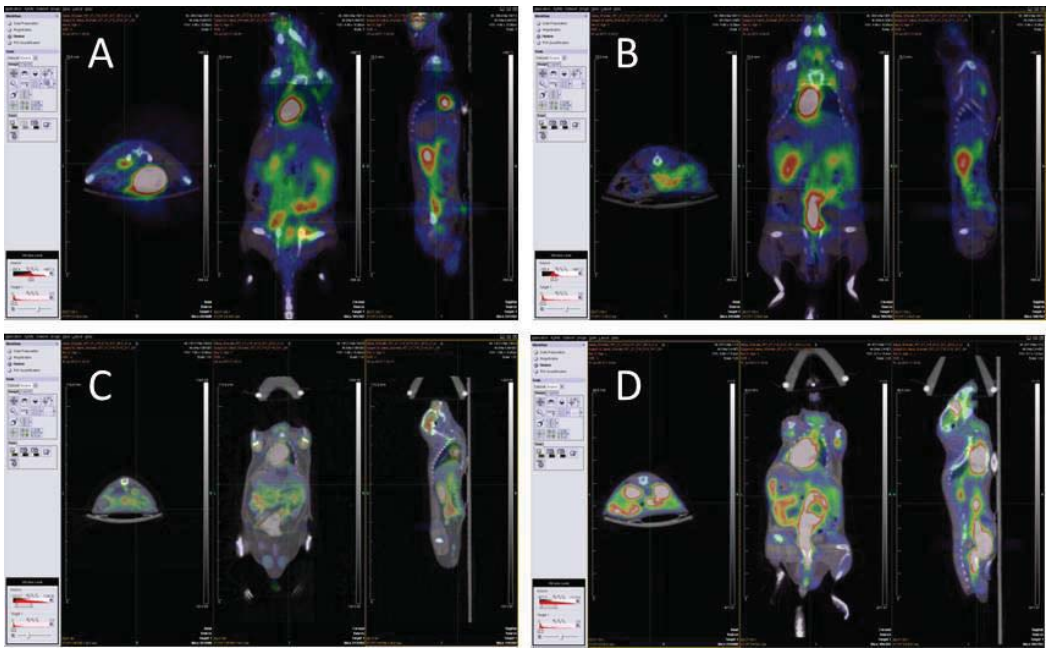

Figure 3.8. PET-CT/FDG images of mice subjected to five days of DSS administration untreated (A), treated with placebo (B) or liposomal suspensions containing Nanotex (C) with or without ω-3 PUFA-EE (D).

Increased ^{18}F-FDG uptake may be associated to increased inflammation, because macrophages and neutrophils are known to consume large amounts of glucose or FDG. However, a statistical analysis failed to reveal significant differences between the different groups. This could be due to

the heterogeneous behavior of the colonic inflammation which affects different regions in the different animals making it difficult to compare the results of different subjects in the same region. Taken together, our results indicate that measurements of rectal wall thickness provide a more robust indicator to follow colonic inflammation and the effects of different therapies against colon inflammation.

3.3.6. Anti-inflammatory Effects *in vivo* in a Glioma Mouse Model

We then examined the effects of magnetoliposomes containing or not ω-3 PUFA-EE in the inflammation associated to glioma growth, using the C6 glioma models.

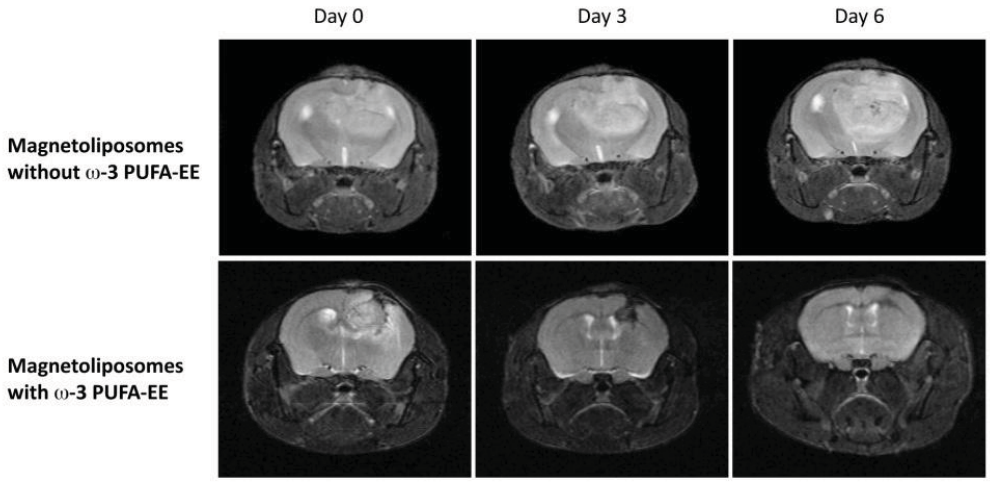

Figure 3.9. Effect of magnetoliposomal preparations containing (bottom) or not (top) ω-3 PUFA-EE on the time course of glioma development after implantation of C6 cells in the mouse brain. Left panels (day 0), central panels (day 3), right panels (day 6).

Figure 3.9 shows representative MRI T_2w images of glioma evolution in a mouse treated with magnetoliposomes containing (bottom panels) or not (upper panels) ω-3 PUFA-EE. Mice receiving magnetoliposomes

without ω-3 PUFA-EE developed tumors to the same extent than controls receiving no treatment (not shown). However, mice receiving magnetoliposomes containing ω-3 PUFA-EE decreased notably the rate of glioma growth, and even increased the regression rate of the implanted glioma.

Table 3.5. Assesment of tumor growth in mice receiving magnetoliposomes containing or not ω-3 PUFA-EE.

Type of magneto liposomes administered	Mouse	Initial size (mm^2)[a)]	Final size (mm^2)	% increase (+red) or decrease (-blue)
With ω-3 PUFA-EE	Mouse 1	12.624	2.825	-77.62%
	Mouse 2	6.07	0.396	-93.48%
	Mouse 3	8.952	0.347	-96.12%
	Mouse 4	24.377	10.179	-58.24%
Without ω-3 PUFA-EE	Mouse 5	15.756	27.5	+74.54%
	Mouse 6	14.473	20.212	+39.65%
	Mouse 7	8.298	13.787	+66.15%
None	Mouse 8	12.72	18.87	+48.35
	Mouse 9	38.89	131.82	+238.96

[a)] Tumor area reflects the area including the tumor and surrounding inflammation as detected in coronal cross sections T_{1w} images of acquired as indicated in Methods.

In addition to the MRI results, it is important to comment in this model, the aspect and behavior of the mice. Mice with no treatment depicted

piloerection, decrease in motor activity and eventually hemiplegia and hemiparesis, becoming necessary to sacrifice them after two or three weeks to comply with bioethical criteria. However, mice treated with liposomes with fatty acids ester SOLUTEX did not present such symptoms, revealing significantly better physiopathological state and regression of the disease. Table 3.5 summarizes the results in an experiment including two different treatments, mice treated with magnetoliposomes containing or not ω-3 PUFA-EE, as well as control group with no treatment. The study of the T_1 images revealed an intense anti-inflammatory effect in the mice treated with ω-3 PUFA-EE, inducing a reduction in the volume of glioma (and the edema) and eventually regression of the tumor.

3.4. Discussion

I have presented a novel liposomal formulation combining the therapeutic properties of ω-3 PUFA-EE with the non-invasive imaging capabilities of Nanotex or Rhodamine, or the combination of both. The preparation depicts potent anti-inflammatory effects against colonic inflammation and is endowed with spectacular and unexpected antitumoral effects against C6 glioma, providing a valuable illustration of a novel and successful theragnostic strategy

Interestingly, the encapsulation of a superparamagnetic nanoparticle in a liposome results in different relaxivity properties as compared to those of the free nanoparticle in suspension. The relaxivity value r_1 increases from 0.55 s^{-1} mM^{-1} for free Nanotex in suspension to 6.26 s^{-1} mM^{-1} for

Nanotex encapsulated in liposomes. In the case of r_2, the value of 88.97 s^{-1} mM^{-1} for free Nanotex in solution decreases to 64.61 mM^{-1} s^{-1} for encapsulated Nanotex. These changes reflect certainly modifications in the dynamics of the nanoparticle-water interaction induced by the encapsulation process. Indeed it would be expected that the encapsulation would decrease the interaction of the nanoparticle with the surrounding water, because of the insulating effects of the liposomal membrane barrier. These reduction effects are expected to occur mainly in the "outer sphere" relaxivity component, representing approximately 50% of the total relaxivity [12, 108]. The "inner sphere" relaxivity component, reflecting mainly the direct interaction of the nanoparticle with water would be expected to be very similar in the free and encapsulated states, since it is determined by the magnetic properties of the nanoparticle and its size, two aspects that are not expected to change appreciably during the encapsulation process. The approximately 30% decrease observed in r_2 follows closely enough this interpretation. However, a similar decrease would also be expected to occur in r_1. This is not observed, indicating that the "outer sphere" effect is not the only determinant of the changes in relaxivity occurring after liposomal encapsulation. The r_1 value shows, in contrast, an important increase, larger than an order of magnitude. The most probable cause of this increase is a restriction in the rotational movement of the nanoparticle in the encapsulated environment. This may be imposed by, either an association to the liposomal membrane, an increase in intraluminal microviscosity, or binding or interaction with neighboring nanoparticles, resulting in a slower tumbling time (τ_r in [108]), reflected predominantly in r_1. Indeed r_1 and r_2 have different determinants and behavior, as

explained from the different Solomon-Bloembergen-Morgan equations [108-111], and it is not surprising that they respond differently to encapsulation. Moreover, r_1 and r_2, reflect the different time scales of T_1 (s) and T_2(ms), making easier to understand that the events occurring in the ms range of T_2, may be too fast to be detected in the second range time-scale of T_1. In conclusion, the encapsulation of Nanotex in liposomes appears to decrease the contribution of the "outer sphere" contribution, reflecting diffusional limitations imposed by the liposomal membrane, and decrease the tumbling time of the nanoparticle, revealing associations to the liposomal membrane or to other nanoparticles.

The liposomal encapsulation ω-3 PUFA-EE merits also further comments [112, 113]. Our results show that it is possible to encapsulate significant amounts of the lipid soluble ω-3 PUFA-EE in the lumen of liposomes. This can be observed by the prominent ^{1}H HRMAS resonances of liposomal suspensions containing the encapsulated fatty acids. The fact that these resonances are observed reveals that the ω-3 PUFA-EE are present as small, fast tumbling goticules inside the liposomes. This is because the similar ω-3 PUFA-EE goticules present in water suspensions, pass easily through 300 kD filters, while encapsulated ω-3 PUFA goticules, do not pass through the same filters, indicating that they are sequestered in the liposomal interior. This finding is further confirmed by the fact that liposomal preparations containing encapsulated ω-3 PUFA EE show the same ADC as the empty liposomal preparations, revealing that the obstructions contributed by the ω-3 PUFA-EE goticules do not contribute appreciably to the ADC of the suspension, dominated mainly by the extraliposomal compartment.

We have shown also that the magnetoliposomal preparations containing Nanotex and ω-3 PUFA-EE present important anti-inflammatory activity against colonic inflammation and spectacular antitumoral effects against glioma.

Colonic inflammation is a disease associated to ulcerative colitis and Chron´s disease, two incurable pathologies at present. These are treated currently with conventional anti-inflammatory therapies [84], mostly free steroidal (budesonide) drugs, and eventually colonic resection by surgery. The formulation proposed here has been shown to become therapeutically useful in animal models of DSS intoxication, adding a new, non-toxic formulation to the arsenal of therapeutic methods against these two morbid and prevalent diseases.

Finally, our liposomal formulation encapsulating ω-3 PUFA-EE and Nanotex has demonstrated spectacular effects against glioma, slowing down proliferation and even inducing remission. These effects are due to the combination of Nanotex and the ω-3 PUFAA-EE since they are not induced by empty liposomes or liposomes containing ω-3 PUFA-EE only. The precise mechanism remains to be elucidated but could probably involve a decrease in the inflammatory component and cytokines required for glioma proliferation and invasion.

In summary our results illustrate the properties and use of a new nanotechnological formulation including one or more imaging agents and a therapeutic molecule, useful in the treatment of the inflammatory component of colonic inflammation and glioma. A patent has been filed protecting the preparation, properties and use of this formulation [114].

Chapter 4

Carbon Nanotubes as novel anisotropic contrast agents for MRI

Chapter 4 provides a systematic study of the magnetic anisotropy properties of Carbon Nanotubes, their molecular determinants and their potential use in Magnetic Resonance Imaging studies of molecular orientation.

4.1. Introduction

Carbon Nanotubes have reached considerable interest in Physics, Chemistry and Biomedicine because of their outstanding physicochemical properties including; electrical conductance, magnetic character, optical activity, thermal capacity, elasticity and chemical versatility [115-122]. These properties are thought to arise from their unique graphene structure as organized in a nanotubular arrangement, in which the asymmetric molecular organization determines the anisotropic physico-chemical properties [123-125]. The magnetic properties and their anisotropic behavior, entail particular interest in this respect, since amorphous graphite is known not to be magnetic, while carbon nanotubes are known to depict non zero magnetic moments, probably reflecting electron flow through π-orbitals surrounding the hexagonal or pentagonal ring constituents [126, 127]. Indeed, a number of studies have addressed the magnetic properties of carbon nanotubes, either theoretically [119, 125-129] or experimentally [130-133].

The use of carbon nanotubes as anisotropic contrast agents in Magnetic Resonance Imaging entails particular relevance, since virtually all currently available contrast agents depict an isotropic behavior. Indeed the use of an anisotropic contrast agent would allow to obtain the three dimensional spatial orientation of molecular assemblies to which it binds, including potentially receptors, microvascular perfusion arrangements and specific cellular populations, in a very similar manner to that afforded by the Diffusion Tensor Imaging with anisotropic water diffusion [134, 135]. However, the origin of their magnetism, their precise magnetic properties and their dependence on molecular orientation in

suspensions of carbon nanotubes, remain still poorly characterized. To progress in this respect, we investigated here the magnetic and optical anisotropies of Single Walled Carbon Nanotubes (SWCNTs) and Multi Walled Carbon Nanotubes (MWCNTs), assessing the possibilities to use these preparations as advanced anisotropic contrast agents in multimodal imaging and particularly in MRI.

4.2. Materials and methods

4.2.1. Single Wall Carbon Nanotubes

Preparation

Three different samples of Single Walled Carbon Nanotubes (SWCNTs) were investigated. Starting from commercial SWCNTs (Sigma-Aldrich, 40-60%, prepared by chemical vapour deposition, CVD) with initial diameters of 2-10nm and lengths of 1-5µm, contaminated with residual Ni (17%) and Y (4%) catalysts, we prepared samples of SWCNTs oxidized for increasing times of 24 and 48h [136]. The original sample (200 mg) was suspended in HNO_3 (65%, 25 ml) and heated to 100 ^{0}C under reflux during either 24 or 48 h [137]. The reaction mixture was cooled down and diluted with deionized water (100 ml). The resulting suspension was centrifuged at 3000 rpm for 10 min and the precipitate was resuspended in deionized water, placed inside a dialysis membrane (Spectra/Por® 3 Dialysis Membrane, MWCO 3500 Da, SpectrumLabs, Rancho Dominguez CA, USA) and dialyzed against water until pH 5.5. The dialyzed suspension was centrifuged to isolate the SWCNTs which were then dried by rotary evaporation.

Characterization

Water soluble SWCNTs were characterized using atomic force microscopy (AFM), high resolution transmission electron microscopy with energy dispersive spectrometry (HRTEM-EDAX), thermogravimetric analysis (TGA) and X-Ray fluorescence (XRF).

AFM Microscopy

The Atomic Force Microscopy (AFM) images were obtained with a commercial AFM (Nanotec Electronica, Cervantes FullMode AFM System, Tres Cantos, Madrid, ES) and monocrystalline silicon cantilevers (Nanosensors PointProbe Plus, Neuchatel, SW) of force constant 2.8 N/m and resonance frequency 75 kHz,. The nanotubes were dispersed in water by ultrasonic agitation (ultrasound bath, 15 min) at a concentration of about 1 mg/ml. The supernatant (2µL) were deposited onto a cleaved muscovite mica substrate and let air-dry for subsequent AFM observation.

HRTEM with EDAX

High Resolution Transmission Electron Microscopy (200 and 400 kV, JEOL, JEM-2000 FX and JEM-4000 EX, Alcobendas, Madrid, ES) in combination with Energy Dispersive X-Ray Analysis (EDAX) was used to determine the metal composition of the contaminant nanogranules. For this study, a few drops of an aqueous and methanol dispersion of the material were placed on a copper grid and evaporated prior to observation.

Termogravimetric Analyses (TGA)

We used TGA to assess the effect of the oxidation time on the total amount of metal catalyst present. Thermogravimetric analyses were performed on a thermobalance TGA Q500 (TA Instruments, Barcelona, ES) using the following conditions. Nitrogen atmosphere: Temperature ramp-rate: 50 °C/min, heating: 20-900 °C. Air atmosphere: Flow rate of 90 ml/min, Temperature ramp-rate of 50 °C/min, heating from 20 to 1000 °C.

X Ray Total Reflection Fluorescence (TXRF)

TXRF spectra were acquired with a TXRF Extra-II (Rich&Seifert, DE) spectrometer.

Superconducting Quantum Interference Device (SQUID)

To measure the hysteresis loops by SQUID we used the different SWNTs samples (commercial, 24h and 48h) dissolved in Fetal Bovine Serum (2mg/ml) and ultrasonicated 15 minutes. The sample was put inside de SQUID magnetometer (Quantum Design MPMS XL-5, San Diego, California, USA) in a liquid state. We applied a 5T field to orientate the nanotubes and then frozen the sample to maintain orientation. We measured the hysteresis loop at 5K in two directions, in the parallel and perpendicular axes of the nanotube with respect to the external magnetic field.

Magnetic Resonance Imaging (MRI)

For the Magnetic Resonance Imaging measurements, we mixed the SWCNTs suspension with melted agarose (0.5%, low melting 370C, Sigma-Aldrich, St. Louis, Mo, USA), and cooled down (22^0C) to form a

solid gel inside a 7T magnet. This protocol was able to maintain oriented the SWCNTs in the B_0 direction while gelling, keeping thereafter this orientation in the solid agarose matrix. The SWCNTs oriented sample was placed in an Eppendorf tube accommodated to a home-made goniometer, allowing the manual rotation of the sample inside the magnet (Figure 4.1).

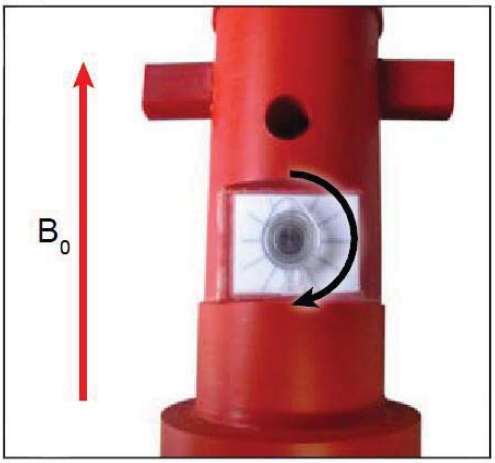

Figure 4.1. Home-made goniometer for directional MRI measurements. This device makes it possible to rotate the sample in multiple directions inside the magnet, including the parallel and perpendicular orientations to the magnetic field.

We measured T_2 values varying the orientation of the sample with respect to B_0. We used a spin echo sequences (TR=5000ms, TE=12ms) as implemented in a Bruker Pharmascan 7 Tesla scanner (Bruker Daltonics, Ettlingen, DE), employing a 38 mm volume coil. The Magnetic Resonance Imaging measurements were analysed pixel by pixel with the home made MyMap Analyzer software based in MatLab (MathWorks, Natick, Massachusetts, USA) to obtain the corresponding T_2 map.

Cytotoxicity

We investigated cellular toxicity of SWCNTs oxidized for 24h using two different methods, either assessing mitochondrial function (MTT assay) or plasma membrane integrity (LDH assay), respectively. C6 cells were grown to confluence in Dulbecco's Modified Eagle Medium (DMEM) using 96 well plates. SWCNTs suspensions prepared on Fetal Bovine Serum (FBS) (Gibco, Life Technologies, Alcobendas, Madrid, ES), were added to each well in final concentrations of 1, 10, 100 and 1000 µg mL^{-1}, using three cell replicas for every SWCNTs concentration. The viability of the cellular preparations was determined spectrophotometrically (570nm, Spectramax, Molecular Devices, Downington, PA, USA) 1h and 24h after the addition of the different SWCNTs suspensions, using commercial kits to determine mitochondrial performance as the reduction of tetrazolium salts (MTT, Millipore, Billerica, MA, USA). As blank we used the medium from cells incubated in the absence of SWCNTs while cell death was induced by adding the toxic hydrazine (5 mM) to the incubation medium.

4.2.2. Multiwall Carbon Nanotubes

Preparation

We used commercial Multi-Walled Carbon Nanotubes (MWNTs < 10 nm outer diameter, 1-2 µm length) synthesized by chemical vapor deposition (CVD) (SES Research Houston TX USA). To prepare the nanotube treated samples, the first step was the fragmentation of MWCNTs consisting in an oxidation under sulfonitric conditions during 24 hours in an ultrasonic bath at room temperature. This step is necessary to obtain shorter carbon nanotubes that were subsequently derivatized by π-π stacking

forming adducts with aminopyrene, which are significantly more soluble than the commercial and oxidized MWCNTs. Pristine MWCNTs (330 mg) were sonicated in a water bath for 24 h in 48 mL of sulfuric acid / nitric acid (3:1 v/v, 98% and 65% respectively) at room temperature [138-140]. The preparation followed then a sequence of rehydration with deionized water and filtration (0.45 µm, Omnipore membrane filtration, Millipore, US) until pH became neutral. Finally the sample was dried, obtaining an 84% of nanotubes oxidized (MWNTsCOOH). To stack the aminopyrene adduct, 25 mg of MWCNTsCOOH were suspended in 65 mL of DMF, ultrasonicating the suspension at 25 ^{0}C during 48 hours [141]. After that, when the suspension appeared homogenous, 160 mg of aminopyrene were added and then the mixture was stirred 3 hours. The π-π stacking adducts formation was confirmed by TLC (Thin Layer Cromatography). The residue was washed with Et_2O and filtered (0.45 µm, Omnipore membrane filtration, Millipore, US).

Characterization

The samples of MWCNTs (commercial, oxidized and oxidized containing aminopirene) were characterized by Transmission Electron Microscopy (TEM). Transmission Electron Microscopy experiments were performed using JEOL JEM 2100 microscope (JEOL Ltd., Tokyo, JAP) operating at 200 kV. For TEM visualization, samples were prepared by dropping a solution of the compounds on a carbon copper grid (300 mesh).

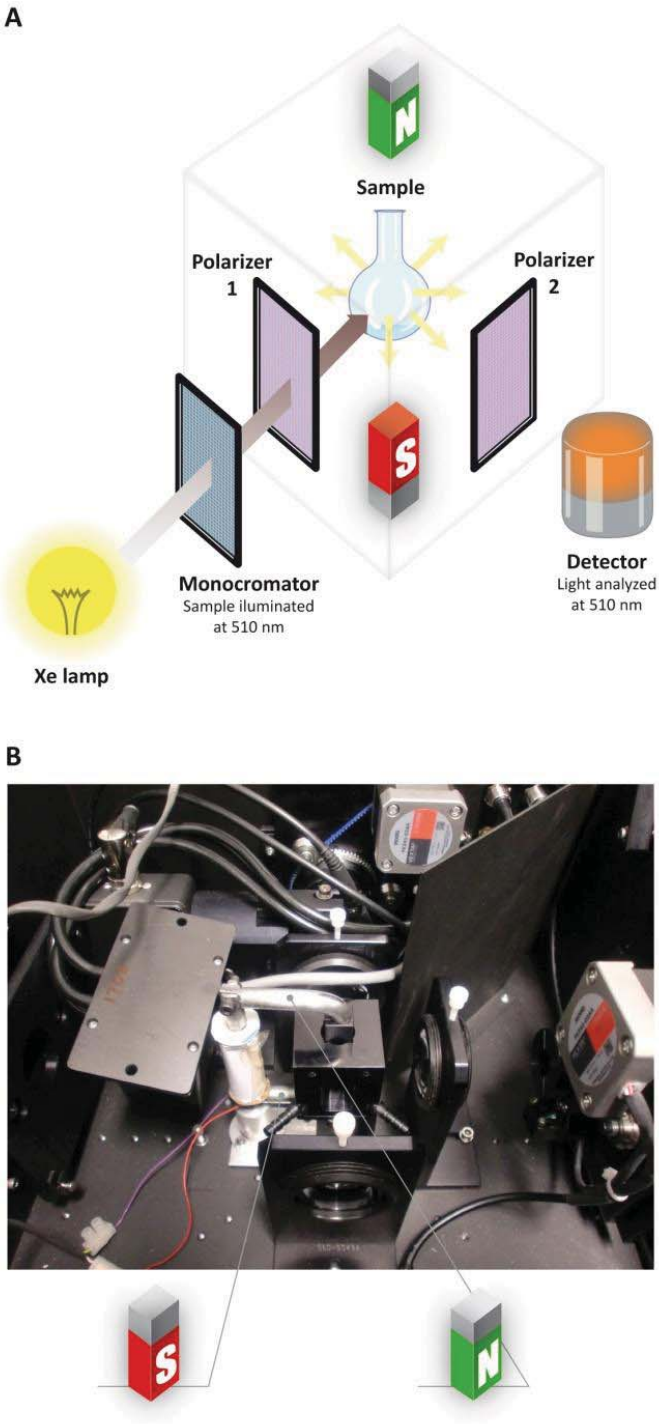

Figure 4.2. Experimental set-up of the magnetic aligment experiment detected with the fluorimeter. Scheme A: Light produced in a Xe Lamp goes through a monocromator to illuminate the sample at 510 nm, the same wavelength detected. Before and after the sample path, there are two polarizing lenses used to measure the anisotropy. An electromagnet allows to apply magnetic field transiently or continuously. B: Photograph of the device.

Magnetooptical studies of nanotube alignment

Light Dispersion

To investigate the alignment of the nanotubes in suspension (N,N dimethyilformamide, DMF, 3mg/mL) we used a QuantaMaster fluorimeter (PTI, Birmingham, NJ, USA) allowing for the measurements of light dispersion and anisotropy in the samples.

For the magnetic alignment of the preparations we used a home-made arrangement placed inside the fluorimeter, consisting of an electromagnet with its poles applied to the top and bottom of the fluorescence cuvette, leaving free the optical path. The field intensity of this magnet is 50 Gauss ($5 \cdot 10^{-3}$ T). The experimental set-up is shown in Figure 4.2.

Light Absorption

The orientation of the nanotubes was further investigated by following spectrophotometrically (LAMDA 1050 UV/Vis/NIR, PerkinElmer, Waltham, MA, USA) the changes in absorbance with sample orientation in the nanotube suspensions. Two types of MWCNTs samples were used, either MWCNTs in solution (Dimethylformamide, DMF, 3 mg/mL) or MWCNTs magnetically oriented and fixed in a solid block of agarose (Sigma-Aldrich, St. Louis, Missouri, USA, 0.5%). In the solution study we used the same home-made magnet described in the light dispersion studies (Figure 4.2.B).

For the study in the solid block of agarose, MWCNTs were dissolved in at high temperature (60 ^{0}C) in liquid agarose and accommodated overnight inside a 7T Bruker Pharmascan magnet (16 cm bore) to orient the

nanotubes while liquid and keep them fixed along B_o direction while gelling. This experimental set-up is described in Figure 4.3.

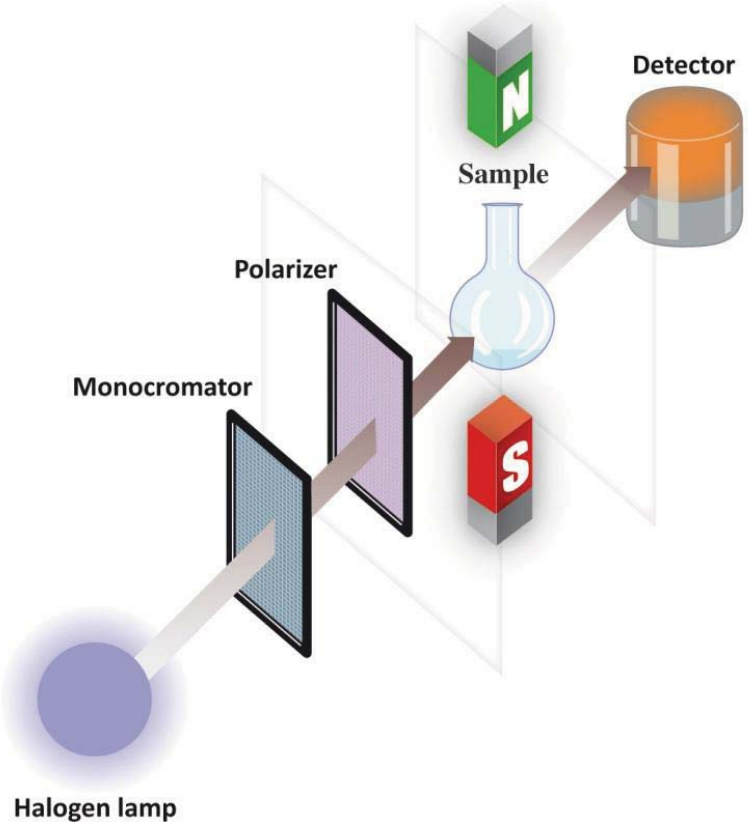

Figure 4.3. Experimental set-up of magnetic aligment detected through the absorption of polarized light. Light produced by an halogen lamp passes through a monochromator to illuminate the sample at 340 nm. A polarizing lens is located between the monochromator and the sample to allow rotation of the polarizing plane of light.

Magnetic Resonance Imaging

MRI techniques were used in the study of the alignment of the carbon nanotubes. T_2 maps were obtained from a solid block of agarose with nanotubes fixed in a known direction. The sample was manually rotated inside a 7T Bruker Pharmascan and T_2 maps (spin-echo sequence, TR=5000 ms, TE=12 ms) were acquired in two orthogonal directions, parallel and perpendicular (Figure 4.1). The T_2 maps were analysed using

MyMap Analizer, an in a home written software for image analysis based in MatLab libraries.

4.3. Results

4.3.1. Determinants of Magnetic Anisotropy in SWCNTs Suspensions

Oxidation of the nanotubes modifies their length as detected by Atomic Force Microscopy (AFM). Figure 4.4 shows representative Atomic Force Microscopy (AFM) images of either commercial preparations of SWCNTs (Figure 4.4 A) or those obtained after nitric acid treatment for 24h (Figure 4.4 B) or 48h (Figure 4.4 C). These panels illustrate the classical nanotubular structures containing characteristic metal catalyst granules as detected with AFM [136]. The nitric acid oxidation treatment (24h-48h), reduced notably the SWCNTs length from 1-5 μm in the commercial preparation to 200-700 nm in the 48h oxidized preparation, reducing also the number of observable metallic granules. The oxidation process increased concomitantly the width of the shortened tubes, roughly from 1 nm in the commercial preparations to approximately 5-15 nm after 24h or 48h oxidation (Figure 4.4 D). Reduction in length is derived from oxidative breakdown of the nanofilaments while the increase in diameter may be caused by the longitudinal folding and stacking of two or more nanotube fragments, containing or not some residual Ni covering.

Thermogravimetric analysis (TGA) showed a decrease in the total metal content from 33% in the commercial preparations of SWCNTs to 20% and

8% in the preparations oxidized for 24 or 48h, respectively (Figure 4.4 E) [137].

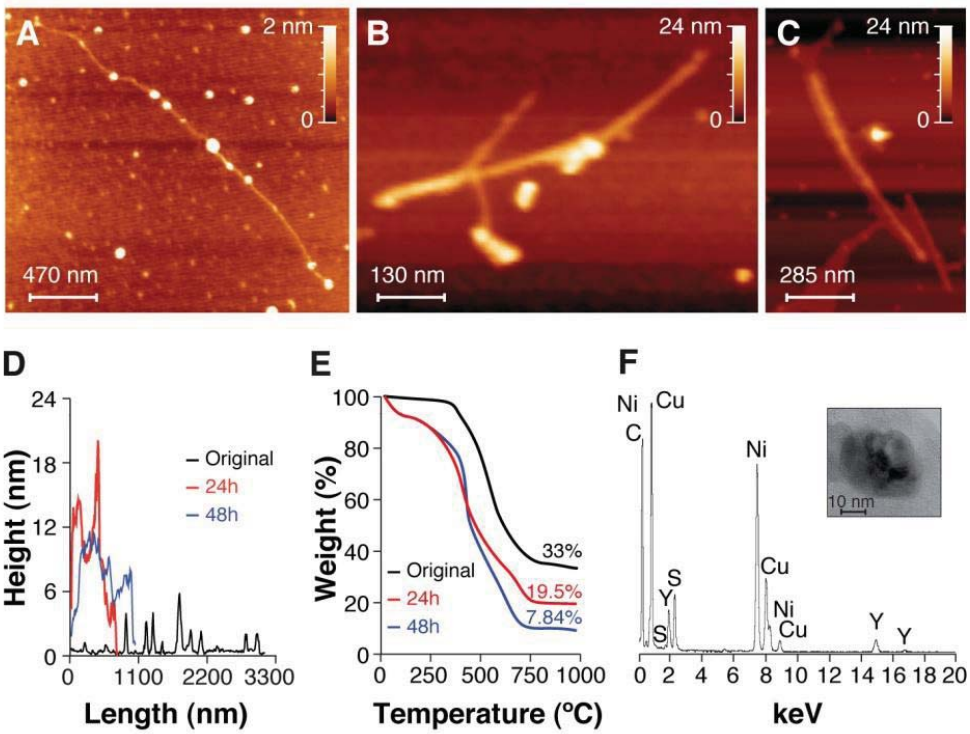

Figure 4.4. Characterization of Single Walled Carbon Nanotubes. Representative AFM images of SWCNTs preparations before (A) and after oxidation during 24 (B) and 48 h (C). The metal granules of the samples are easily observed. Height-Length plots obtained by AFM during shortening of SWCNTs before and after oxidation during 24 and 48 hours (D). Nanotubes become shorter upon oxidation and their height increases. TGA analysis shows a decrease in the content of metal contaminants with the oxidation time of the SWCNTs preparations (E). Metal content decreases with oxidation time. HRTEM with EDAX microanalysis shows that the catalytic nanoparticle is composed of Ni (insert) and Y (F). The peaks of Carbon, C, and Copper, Cu, correspond to SWCNTs and the grid, respectively.

To investigate the metal composition in the preparations we implemented High Resolution Transmission Electron Microscopy with Energy Dispersive X-Ray Analysis (HRTEM-EDAX), as indicated in the Materials and Methods section. Figure 4.4 F shows the results obtained which revealed Ni and Y as the principal paramagnetic metal

contaminants of the metallic nanogranules (Figure 4.4 F, insert), the Cu signals being derived mainly from the grid [137]. Roughly, Ni and Y content of the commercial preparations (17.6 % and 4.3 %), decreased after 24h oxidation (5.1 % and 0.9%) and even further after 48h oxidation (3.3 % and 0.6 %), as detected by Total X Ray Fluorescence Reflection spectrometry (TXRF) respectively [136].

We next explored, the magnetic properties of the SWCNTs preparations oxidized for increasing times using SQUID (Figure 4.5).

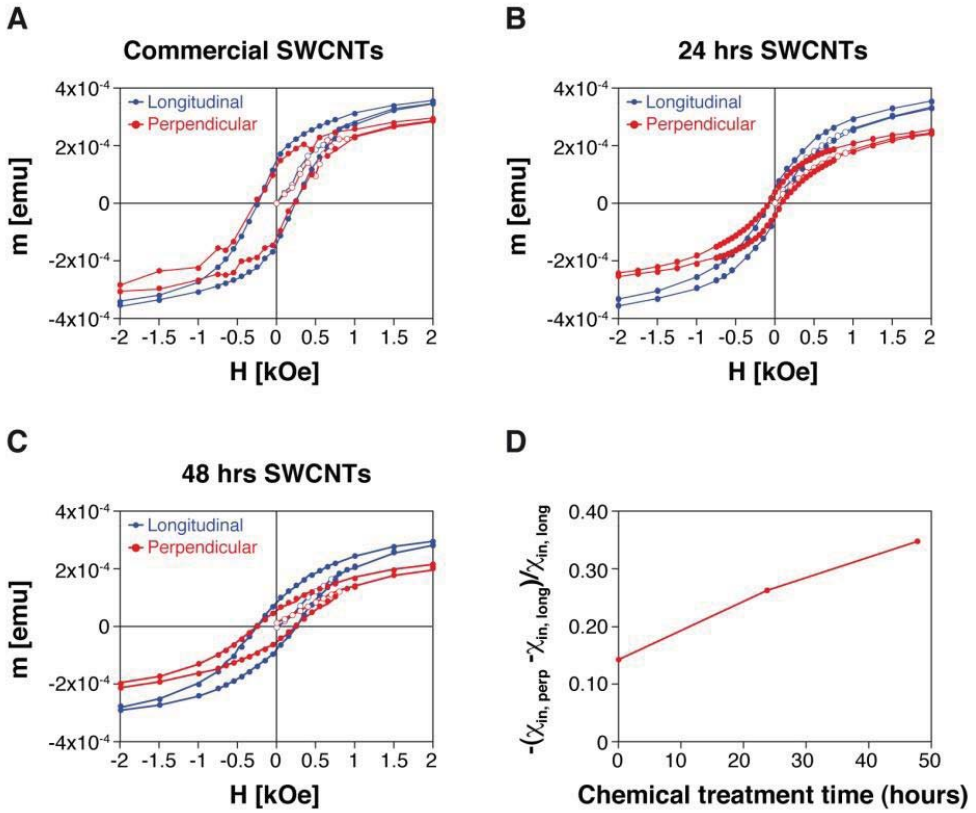

Figure 4.5. Magnetic properties of SWCNTs. Magnetic hysteresis Loops (full dots, continuous lines) and virgin curves (empty dots, dotted lines) of SWCNT preparations oxidized with nitric acid for 0h (A), 24h (B) and 48h (C). Evolution of magnetic anisotropy along chemical treatment time (D). Note the increase in the magnetic anisotropy value with increasing oxidation time.

To measure hysteresis loops and virgin curves by SQUID we used the SWCNTs samples (commercial, 24h and 48h) dissolved in Fetal Bovine Serum (2mg/ml) and ultrasonicated 15 minutes. Magnetic hysteresis loops were measured at 5 K and angles of θ = 0 degrees and θ = 90 degrees, with respect to the direction of the applied magnetic field, for oriented nanotube suspensions. Briefly, the nanotube suspensions were introduced in the magnet in the liquid state for orientation, and frozen to 5K where they remained oriented and fixed within the ice matrix. We measured then, virgin curves and hysteresis loops under these conditions and after 90 degrees rotation of the frozen sample. These measurements revealed clearly a paramagnetic behavior [142]. When the commercial SWCNTs preparation was oriented parallel to the external magnetic field (blue circles and lines), the magnetizations detected were larger than those measured in the perpendicular direction (red circles and red lines) (Figure 4.5 A). The same behavior was observed in SWCNTs preparations oxidized for 24h (Figure 4.5 B) and 48h (Figure 4.5 C), although the magnitudes of total magnetization and magnetic susceptibility were different in each case. In addition, the virgin curves (empty circles) revealed that magnetic susceptibility of SWCNTs is larger when measured in the parallel than in the perpendicular orientations. Notably the magnitude of the magnetic anisotropy ($-\chi_{perp} - \chi_{paral} \cdot \chi_{perp}^{-1}$) increased from 0.14 in the commercial preparation, to 0.26 and 0.35 after 24h and 48h oxidation, respectively (Figure 4.5 D).

Considering that the 24 and 48h nitric acid oxidations decrease the length, increase the diameter and decrease the metal content (Figure 4.4 D and E), these results suggest that the increase in magnetic anisotropy

of the SWCNTs preparations (Figure 4.5) is caused by the changes in these properties. Increased magnetic anisotropy of SWCNTs preparations oxidized for 24 or 48h, may thus reflect an easier alignment in the magnetic field of the shorter nanotubes than of the commercial nanofilaments, including also the formation of longitudinal aggregates with larger diameter (c.f. Figure 4.4 D).

We further investigated then the determinants of magnetic anisotropy in SWCNTs preparations using Magnetic Resonance Imaging. We prepared first an oriented sample of commercial SWCNTs in solid agarose (0.5% w/v) by suspending the SWCNTs in melted agarose (60 ^{0}C) and allowing the mixture to cool down to room temperature until the agarose became a solid gel, entrapping the SWCNTs [136]. We investigated then the anisotropy contributed by soluble Ni ions and by superparamagnetic Ni nanoparticles in the SWCNT suspension. To achieve this, we begun by entrapping a 10 mM NiCl solution (Sigma Aldrich, Alcobendas, Madrid, ES) in solid agarose (0.5% w/v). We entrapped also in agarose suspensions commercially available Nickel nanoparticles (577995, Sigma Aldrich, MO, USA).

Note that a significant difference of average T_2 values is observed in the SWCNTs gel between the two orthogonal orientations, while no difference is detected in the gels with $NiCl_2$ or Ni nanoparticles.

We obtained then MR images at room temperature, weighted in the transversal relaxation time (T_{2w}), of the SWCNTs preparations (Figure 4.9 upper left panels), of the Ni gel (Figure 4.9, middle left panels) and of the superparamagnetic nanoparticles gel (Figure 4.9, lower left panels) in the

parallel and perpendicular directions to the external magnetic field using a home-made goniometer (Figure 4.1).

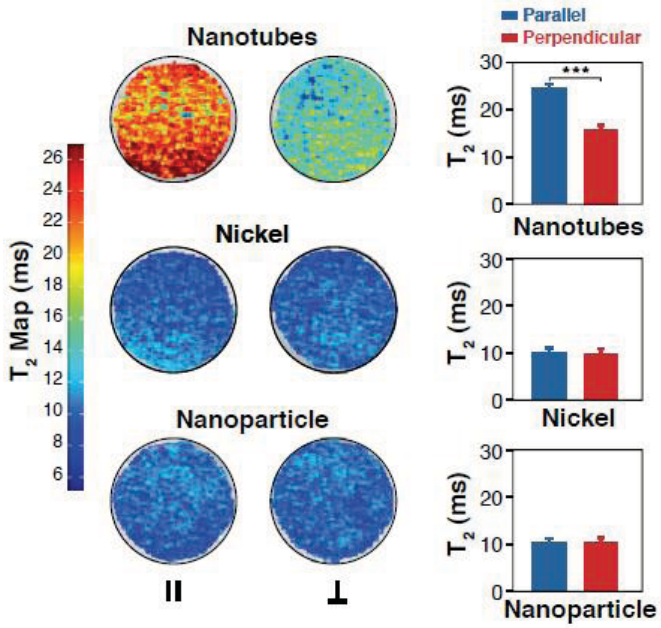

Figure 4.6. T_2 imaging of SWCNTs suspensions oriented in agarose gels at room temperature (22 ^{0}C). Water T_2 maps (left panels) for Single Walled Carbon Nanotube preparations (top), a $NiCl_2$ solution (center) and superparamagnetic nanoparticles (bottom), as embedded in solid agarose gels (0.5%) oriented parallel (II) or perpendicular (⊥) to the static magnetic field B_0. Average T_2 values for the three preparations (right panels).

T_2 maps were then calculated pixel by pixel from the collection of images as indicated in Supplementary Information. The bargraphs (Figure 4.9, right panels) summarize the average T_2 values of the pixels from SWCNTs (upper right panel), oriented Ni gels (middle right panel) and oriented Ni nanoparticle gels (lower right panel), when the solid agarose gel was oriented parallel (blue) or perpendicular (red) to the static magnetic field. As control we obtained the same T_2 maps from agarose gels devoid of SWCNTs, Ni ions or Ni nanoparticles.

Note that the SWCNTs preparations depict significantly larger T_2 water values when oriented in the parallel (blue) than in the perpendicular (red) directions, as revealed by the shift to the green in Figure 4.9 (upper left panels) and the values shown in the corresponding bar graphs (right panels). Notably, the pure agarose gel, and the Ni ion and Ni nanoparticle gels showed the same T_2 values in the parallel and in the perpendicular directions. Taken together, these observations indicate that soluble Ni ions, spherical superparamagnetic nanoparticle suspensions or the agarose gel itself, do not present an intrinsic anisotropic behavior.

4.3.2. SWNCNTs Cytotoxicity

For its potential use as a contrast agent in MRI, it was necessary to measure the toxicity of SWCNTs (Figure 4.11). We observed approximately 100 % cell viability in the absence of SWCNTs and roughly null viability in cells exposed to the toxic. A decrease in formazan production was detected at the highest SWCNTs concentrations, a finding that has been described previously to be due to a direct reaction of the nanotubes with the MTT molecule, rather to a cytotoxic effect on the cells [143]. To further investigate cytotoxicity, we performed additional tests using the same SWCNTs preparation but measuring the release of lactate dehydrogenase (LDH) from the cell suspensions as an indicator of plasma membrane integrity and cell viability (Figure 4.11, B, D).

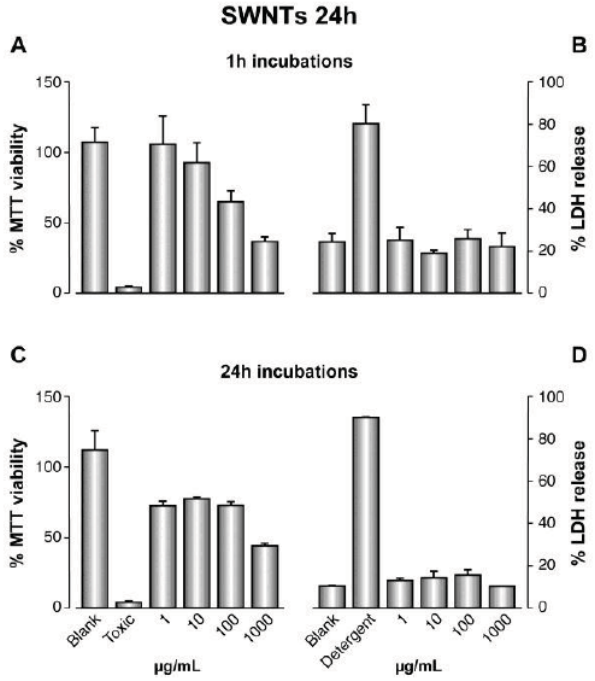

Figure 4.7. Study of citotoxicity of SWCNTs. MTT assays (A,C) and fractional LDH release assays (B, D) of cellular viability for increasing concentrations of SWCNTs oxidized with nitric acid for 24h, either 1h (A, B) or 24h (C, D) after the addition of the SWCNTs suspensions (1-1000 µg mL^{-1}) in Fetal Bovine Serum to the cells.

Briefly, SWCNTs were added to each well to final concentrations in the 1-1000 µg.mL^{-1} range. LDH activity was determined spectrophotometrically (340 nm, Spectramax, Molecular Devices, Downington, PA, USA) following the linear decrease in NADH absorbance in mixtures containing 50 mM HEPES pH: 7.0, 5 mM pyruvate and 0.6 mM NADH. We initiated the reaction with the addition of either aliquots from the incubation medium or from the cell lysate obtained after four cycles of freezing and thawing. We used as blanks, aliquots of the incubation medium containing no SWCNTs and as a maximum LDH release, that induced by adding the detergent sodium dodecylsulfate (2%) to the cell suspensions. We determined then the fractional LDH released (LDH medium/(LDH medium+LDH lysate) either after 1h or 24h incubations. While we

observed no significant fractional LDH release in the blanks or close to 90 % after detergent treatment as expected, we detected no significant increase in fractional LDH release with increasing concentrations of SWCNTs either after 1h or 24h incubations. Taken together, our results revealed no significant cytotoxic effects of our SWCNTs preparations in the concentrations required for observable magnetic anisotropy effects.

4.3.3. Characterization of Different Preparations of MWCNTs

We began by characterizing the MWCNTs preparation using Transmission Electron microcopy (TEM). Figure 4.8 shows representative results of commercial preparations and those obtained after the shortening treatment. The commercial sample shows important heterogeneity with the presence of abundant impurities and random bundles of nanofilaments (Figure 4.8 A and B).

It became then necessary to shorten them by oxidation and sonication to obtain a more homogenous sample prior to further studies. After the oxidation treatment, the bundles began to disentangle and the shorter nanotubes generated become freer, with some aggregates produced by electrostatic forces still present (Figure 4.8 C and D).

Adsorption of aminopyrene to the nanotubes resulted in a more homogenous sample with fewer nanotubes forming bundles (Figure 4.8 E and F). We obtained a histogram of the treated sample to determine a median value for the length of oxidized MWCNTs with aminopyrene in this preparation (Figure 4.9).

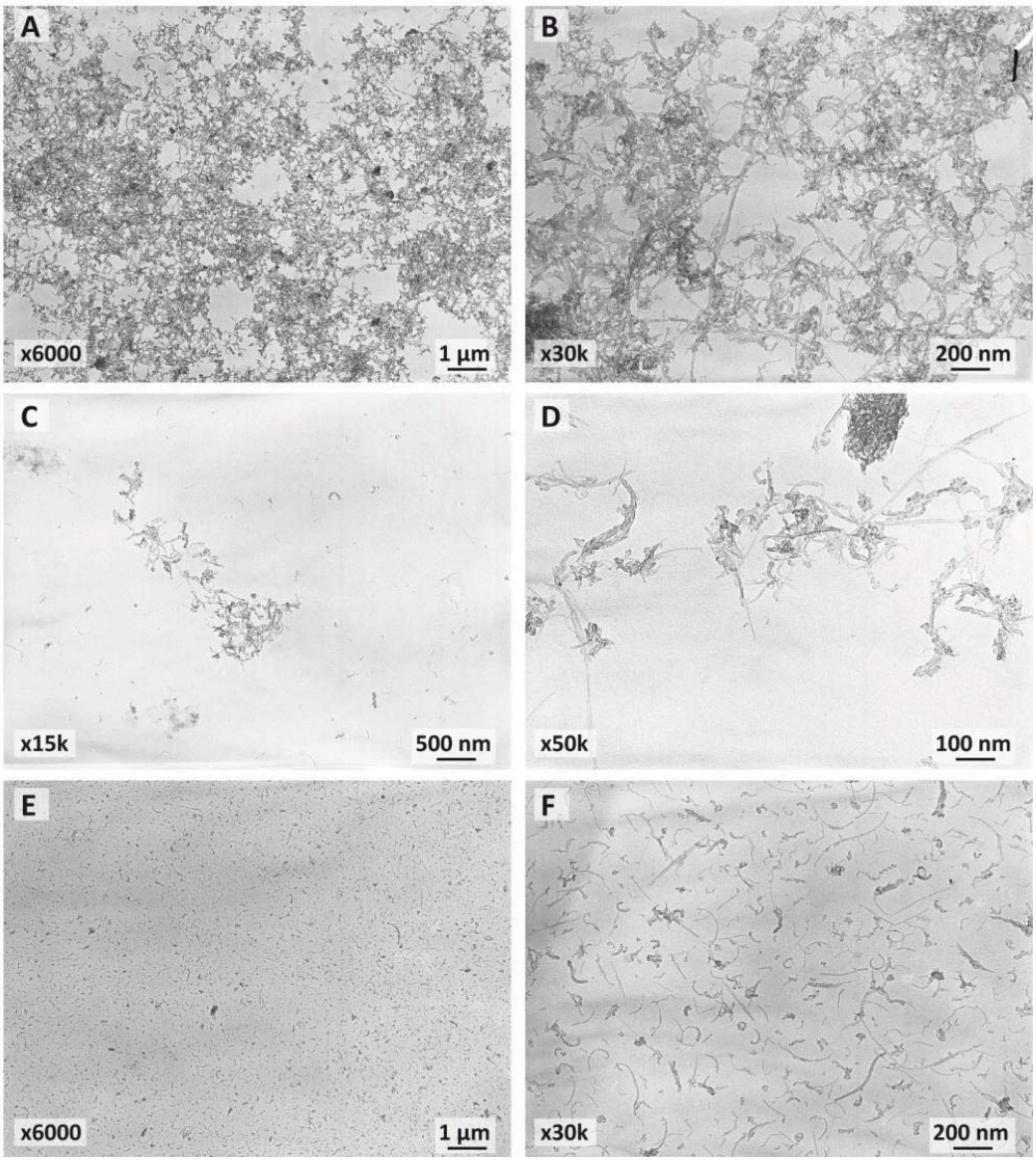

Figure 4.8. TEM images of MWCNTs preparations. Top panels: Commercial nanotubes form abundant bundles as shown at different magnifications (A: 6k, B: 30k). Central panels: Oxidized MWCNTs show some free nanotubes but also abundant nanotube bundles at different magnifications (C: 15k, D: 50k). Bottom panels: Treatment of oxidized MWCNTs with aminopyrene reveals that almost every bundle has been broken to free nanotubes at different magnifications (E: 6k, F: 30k).

The histogram showed an average length of 170 nm for the most populated group. These results show that the nanotubes oxidized and with amynopirene bound, constitute a homogenous dispersion which can be suspended in water for further magneto-optical experiments.

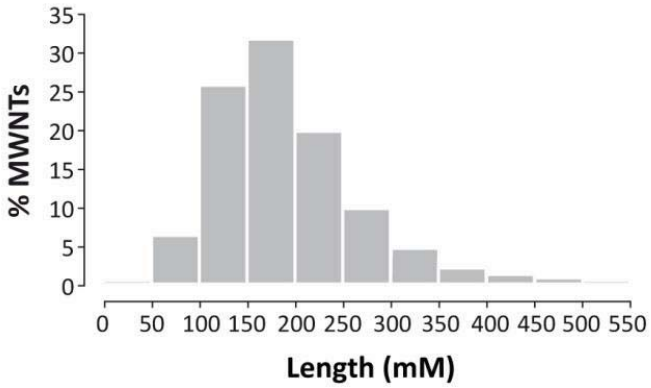

Figure 4.9. Histogram of MWCNTs length after treatment. The most populated size is around 170nm.

4.3.4. Magneto-Optical Evidences of MWCTs Alignment with External Magnetic Fields

We investigated magnetic alignment and anisotropy using these preparations. To this end, it was necessary first, to confirm that our MWCNTs present sufficient magnetism and are able to orient in a magnetic field at room temperature. A light dispersion experiment was designed to investigate the magnetic behavior of MWCNTs. A stable solution of nanotubes suspended in dimethylformamide (DMF) was placed inside a fluorimeter which permited us to collect the dispersed light of the sample at a perpendicular direction to the illumination direction, using crossed polarizers (see Figure 4.2 for the experimental set-up). We prepared an electromagnet with poles on the top and bottom of the quartz cuvette, able to induce a transient or continuous magnetic field through the nanotube suspension, while leaving unperturbed the optical path. We made then successive light dispersion measurements in which the photons dispersed by the sample were collected successively in the detector with the magnetic field turned “on” or “off” (Figure 4.10). We observed that the presence of the magnetic

field induced significant increases in the dispersion while present, revealing magnetic field orientation of the MWCNTs sample.

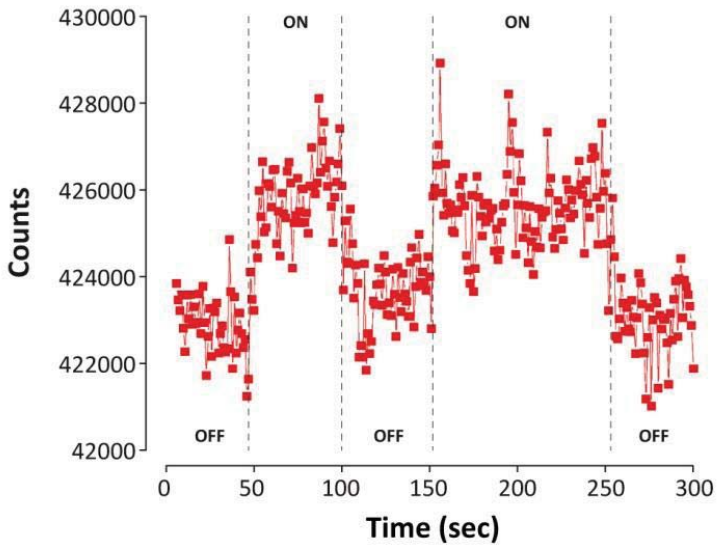

Figure 4.10. Photon counts of dispersed light collected successively in the fluorimeter when switching the magnetic field "on" or "off". The number of counts detected is higher when the magnetic field is switched "on" and decreases if the magnet field is switched "off", in a reproducible manner.

We did one further experiment by switching "on" continuously the magnetic field. In this case, the collected counts increased with time, suggesting that the nanotube orientation of the sample is not instantaneous and that the number of nanotubes oriented parallel to the magnetic field may increase progressively with the time of exposure (Figure 4.11).

When the magnetic field was switched on the number of counts recollected increased linearly with time, suggesting a reorganization of the nanotubes suspended in the sample parallel to the magnetic field so that the photons dispersed more light in the direction of the detector. (Figure 4.12).

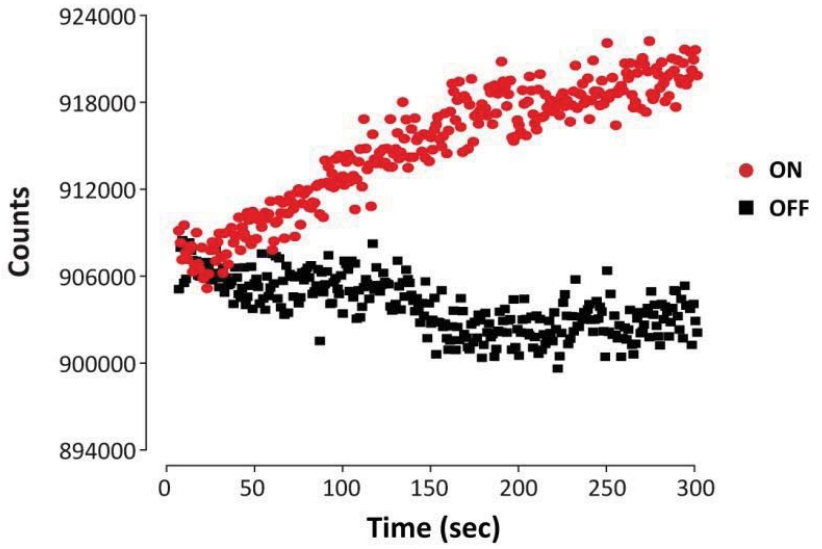

Figure 4.11. Photon counts collected in the fluorimeter with time while switching the magnetic field "on" or "off" continuously. With the magnetic field turned "on" from the beginning, the number of counts detected increases linearly with time.

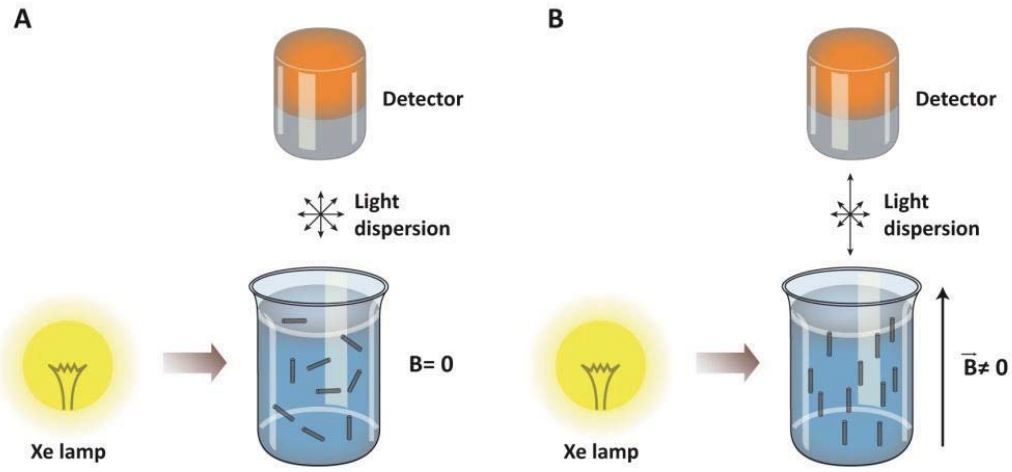

Figure 4.12. Light dispersion in the fluorimeter. With the field "on" the nanotubes reorient parallel to the magnetic field dispersing more photons to the detector than when the field is off.

Anisotropy measurements were also done with the fluorimeter using polarized light. For this experiment two polarizers were accommodated at the exit of the Xe Lamp and in the center of the detector. The

orientations of the polarizers were automatically set by the fluorimeter controls. The fluorimeter calculates the anisotropy of a sample by illuminating the sample with light polarized vertically and horizontally and analyzing the intensity of the light in the detector. The anisotropy is calculated using the equation:

$$A = \frac{I_{VV} - G \cdot I_{VH}}{I_{VV} + 2 \cdot G \cdot I_{VH}} \qquad \text{Eq. 4.1}$$

where I_{VV} is the intensity of the light when both polarizers were in vertical position, I_{VH} with the lamp polarizer vertically and the detector polarizer horizontally and G is the G-factor is just a correction for the polarization given by

$$G = \frac{I_{HV}}{I_{HH}} \qquad \text{Eq. 4.2}$$

where I_{VH} is the intensity of the light when the lamp polarizer is oriented horizontally and the detector polarizer is vertically and I_{HH} when both are horizontally.

The anisotropy was measured along time in two different conditions, with the magnetic field switched “on” and switched “off” (Figure 4.13). When the magnetic field is switch “on” the sample becomes more anisotropic, suggesting that the nanotubes orient parallel to the magnetic field reaching an anisotropic structure.

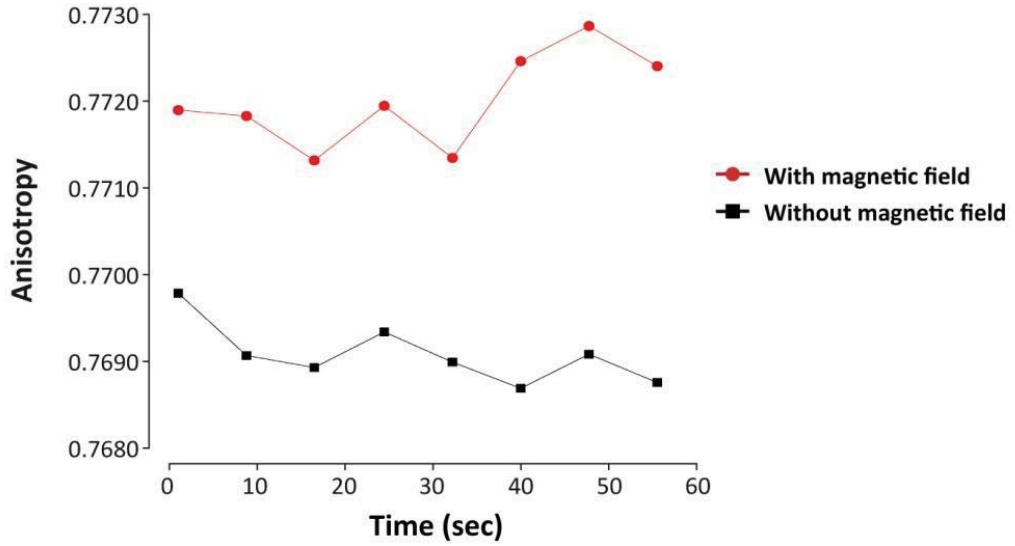

Figure 4.13. Light dispersion anisotropy values along time in the presence and absence of external magnetic field. Note that the nanotube sample becomes more anisotropic with the magnet field switch on.

A similar experiment was performed using spectrophotometric detection with the nanotube suspension containing bound aminopyrene in DMF (Figure 4.3). First of all, we measured the absorption spectra of the sample, finding a maximum at 340 nm, corresponding to the aminopyrene ring [144]. The sample was then illuminated with polarized light (340 nm). When the magnet field was switched "on" and the nanotubes were perpendicular to the polarized light, the absorbance of the sample increased until the magnet field was switched "off" (Figure 4.14).

The next step was to fix the MWCNTs with a known direction in a matrix which permits us to measure the sample in two different directions in MRI. An agarose gel was chosen again for this purpose, keeping it inside a 7 Tesla magnet to fix the nanotubes parallel to the magnetic field direction. To prove that the nanotubes were fixed in that direction we made measurements using the same spectrophotometric set up used to

study the nanotubes suspension. In this experiment we accommodated the matrix gel with nanotubes fixed in a known direction and the polarized light was rotated 360^0 (Figure 4.15).

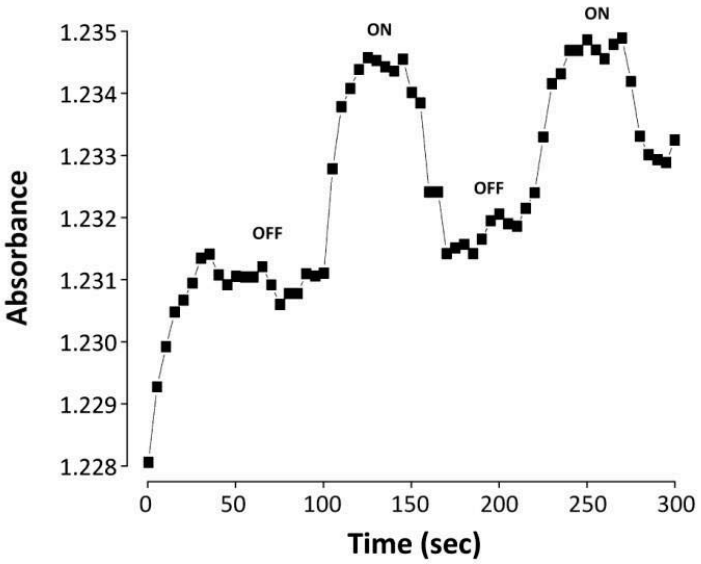

Figure 4.14. Absorbance (340 nm) vs time curve of MWCNTs suspension in DMF, in the presence (ON) and absence (OFF) of magnetic field orientation. The absorbance increased when the magnet field was switched on.

The transmittance of light was maximum when the polarization of the light was perpendicular to the nanotubes (Figure 4.15 A). The transmittance reaches a minimum when the light is parallel (around 90^0) and goes to maximum after a rotation of 180^0. When the sample was rotated 90^0 we obtained a specular figure (Figure 4.15 B). This is due to the π-π absorption of the aminopyrene molecule over the nanotube wall which results in different absorption properties depending on the orientation of the molecule [144]. The aminopyrene is coupled to the nanotube with its 340 nm absorption axis parallel to the nanotube[145].

These results reveal that when the nanotube is parallel to the light polarization plane the absorption is maximum.

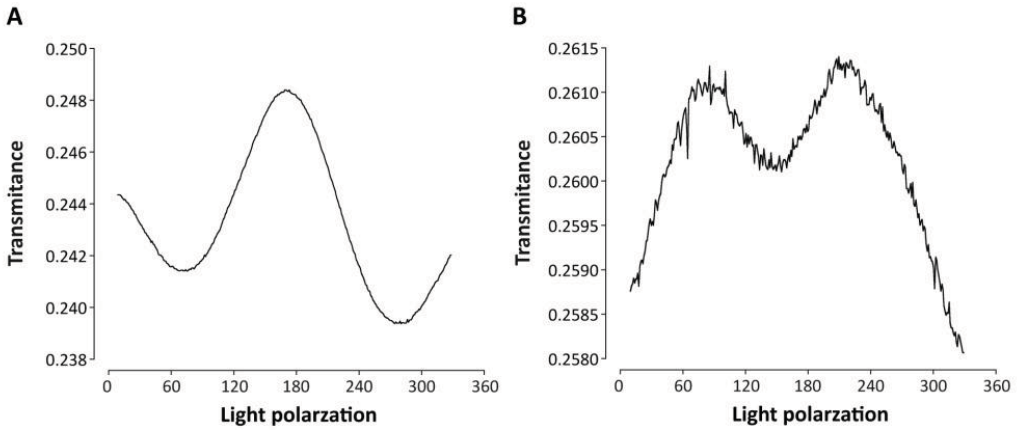

Figure 4.15. Transmittance of a fixed MWCNTs suspension in a solid agarose support for different orientations of the light polarization plane. A: MWCNTs fixed agarose gels are oriented perpendicular to the initial polarization plane (0 degrees). The transmittance reaches maximum values (minimal absorption) when the polarization plane is perpendicular to the longest nanotube axis. B: MWCNTs fixed agarose gels are oriented parallel to the initial polarization plane (0 degrees). The transmittance reaches minimal values (maximal absorption) when the polarization plane is parallel to the longest nanotube axis. The noise in A and B is different because of the different orientation and inclination of the agarose gel during the spectrophotometric measurement.

4.3.5. Magnetic Measurements of Relaxation Times for Oriented MWCNTs

Magnetic anisotropies have been also studied using the solid agarose model to fix the nanotubes. It was measured the transversal relaxivity (T_2) of MWCNTs with MRI techniques. T_2 maps of a solid gel of agarose with nanotubes oriented were measured in two different directions, parallel and perpendicular to the magnetic field (Figure 4.16).

In summary, our magneto-optical measurements confirm that MWCNTs suspensions align with external magnetic fields at room temperature.

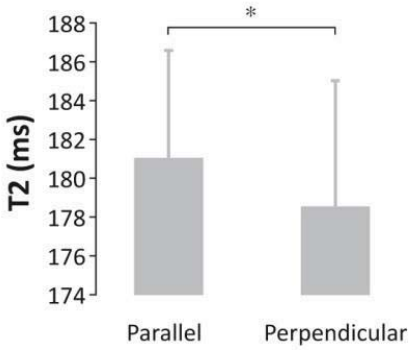

Figure 4.16. T_2 values of MWCNTs fixed in agarose at different directions. Significant differences ($p<0.05$) of T_2 values of MWCNTs fixed in agarose in two different directions.

We obtained similar results than the experiments with SWCNTs, with significant differences between the two measurements of the sample, parallel and perpendicular to the magnetic field.

4.4. Discussion

Using SWCNTs or MWCNTs preparations, I have shown that magnetic and optical anisotropy are macromolecular properties which are conserved in these materials even at room temperature. In this sense, magnetopoptical anisotropy of SWCNTs and MWCNTs add to the large collection of outstanding properties of carbon nanotubes as electrical conductance, thermal capacity or elasticity [115-122]. This is particularly relevant in the MRI contrast agent field since the most widely used gadolinium chelates and superparamagnetic nanoparticles depict isotropic magnetic relaxation properties. Indeed the free energy barriers

for molecular reorientation are very low for subnanometric structures as the gadolinium chelates, or even for spherical nanoparticles and thermally driven molecular reorientation averages the magnetic moment in isotropic manner, at room temperature [146]. The behaviour of tubular nanometric structures is different and the energy barriers required for thermal reorientation at room temperature are sufficiently large to preclude nanotube reorientation at room temperature, thus providing the thermodynamic basis for alignment phenomenon. We believe this is an outstanding finding since it may allow the non-invasive determination of the three dimensional orientation of the nanotube from magnetic resonance measurements of the relaxation properties of the surrounding water in different directions or the diffusional behaviour of water as obtained from Diffusion Tensor Imaging [135]. This would potentially allow to unravel non-invasively and in vivo the three dimensional orientation of molecular assemblies, microvascular trajectories and cellular arrangements by labelling them selectively with SWCNTs or MWCNTs.

In this context, research on the molecular determinants of nanotube anisotropy acquires a fundamental relevance. Our results obtained by SQUID, become particularly enlightening to account for the magnetic anisotropy properties observed in water T_2 by MRI. SQUID measurements reveal that the magnetic susceptibility anisotropy increases with shortening of the nanotubular structures and is not due to the contaminant Ni nanogranules. This indicates that the nanotubes themselves, and their association with the Ni nanogranules, constitute the main determinants of magnetic anisotropy in these preparations.

Moreover, the larger magnetic susceptibilities in the parallel than in the perpendicular directions detected by SQUID provide the physical basis to interpret the longer water T_2 in the parallel than in perpendicular orientations detected by MRI. In MRI, longitudinal (T_1) and transversal (T_2) relaxation times are known to increase with the effective magnetic field B_{effec} [22]. The resulting effective magnetic field on the sample depends then on the static magnetic field provided by the magnet (a constant value) and on the local magnetic field B_{local} originated by the SWCNTs or MWCNTs ($B_{effec} = B_0 + B_{local}$). Thus the local magnetic field depends directly on the magnetic susceptibility of the nanotubes ($B_{local} = \chi \cdot B_0$). Since $\chi_{\parallel} > \chi_{\perp}$ in SWCNTs preparations, $B_{local\,\chi_{\parallel}} > B_{local\,\chi_{\perp}}$ $\vec{B}_{local\,\chi_{\parallel}} > \vec{B}_{local\,\chi_{\perp}}$ and consequently, the water T_2 values observed by MRI are higher in the parallel than in the perpendicular orientation.

The advance in generating a water soluble nanotube preparation merits also further comments. Previous preparations of pristine SWCNTs or MWCNts were highly water-insoluble and useless in medicinal chemistry applications and contrast agent development [115-122]. We have shown here that MWCNTs can be adequately solubilized in water, after size reduction by sonication and aminopyrene π-π binding. The preparations obtained remain soluble and stable for several months, allowing for the development of therapeutic derivatives, imaging probes or both. Furthermore, we also show that the nanotube preparations are non-toxic, as revealed by the MTT and LDH release tests, in contrast with previous reports that showed toxicity in nanotubes preparations

solubilized by detergents. Our results indicate that the nanotubular structures are non-toxic by themselves, at the concentration range required for MRI or therapeutic interventions and that previous toxicity results may have derived from the detergent used, rather than from the nanotubes [147].

In summary, we investigated the determinants of magnetic anisotropy in carbon nanotube preparations and showed that the anisotropic behavior depends on the length and diameter of the nanotubular structures and may involve additional contributions from Ni nanoparticles fixed or adsorbed over the nanotube surface. Our results indicate, however, that the relative content of paramagnetic metals or superparamagnetic nanoparticles, decreases significantly with the oxidation time, suggesting a concomitant reduction in the proportion of bound metals to SWCNTs structures. Thus, the maximal anisotropy is observed in preparations containing the largest proportion of SWCNTs and the smallest content of paramagnetic metals and superparamagnetic nanoparticles. Together, present results suggest that the magnetic anisotropy of SWCNTs suspensions is dominated by the length and diameter of the carbon nanotubular structures, rather than by the contribution of free Ni or Ni nanoparticles, with a non-negligible contribution of Ni+ or Ni nanoparticles bound to or interacting with, the nanotubular structures.

We believe these results open new avenues for the use of carbon nanotubes as directional contrast agents in MRI, as advanced probes to determine the three dimensional orientation of molecular assemblies in vivo and potentially to combine over the same nanoplatform, imaging

agents and therapeutic molecules. A patent covering these aspects has been filed [148].

Conclusions

1. I reviewed the contrast agents currently available for multimodal imaging applications, their advantages and limitations. This review disclosed that the use of innovative strategies provided by Nanotechnology could improve the physicochemical and pharmacological properties of these molecules. On these grounds, I pursued the development of a novel superparamagnetic nanoparticle, its formulation as magnetoliposome and the implementation of carbon nanotubes as anisotropic contrast agents for MRI.
2. I developed and characterized Nanotex, a novel superparamagnetic nanoparticle containing an Fe_3O_4 core, with polyacrylic acid coating. Nanotex, has shown comparable magnetic relaxivity properties, improved pharmacokinetics, reduced vascular retention and tissue accumulation and excellent results when used in "bolus tracking" experiments of perfusion imaging with MRI. Taken together, these results support further development of the particle, as a contrast agent for Magnetic Resonance Imaging.
3. I implemented a new anti-inflammatory nanoformulation based in magnetoliposomes containing Nanotex and ω-3 PUFA-EE, with advantageous properties as a theragnostic contrast agent. The particle may be combined with a fluorescent probe to yield a multimodal theragnostic agent detectable in vivo by MRI, fluorescence or both. This preparation demonstrated considerable antiinflamatory properties in a model of colonic inflammation and a previously unpredicted, outstanding antitumoral activity in a glioma model.

4. I investigated the magnetic properties of Carbon Nanotubes, both Single Walled and Multi Walled. I characterized the magnetic anisotropy observed in Single Walled Carbon Nanotubes as derived from the nanotubular grapheme structure and its interaction with contaminant paramagnetic nanoparticles. Magnetooptical techniques demonstrate also magnetic anisotropy of Multi Walled Carbon Nanotubes, even at room temperature. Magnetic Resonance Imaging confirms T_2 relaxation anisotropy for both types of Carbon Nanotubes at room temperature.
5. In summary, I investigated, developed and proposed novel generations of nanotechnological contrast agents suitable for further development in the multimodal imaging market.

Bibliography

1. Lauterbur, P.C., *Image formation by induced local interactions: examples employing nuclear magnetic resonance.* Nature, 1973. **242**(5394): p. 190-191.
2. Farrell, C., J.D. Wallace, and C.M. Mansfield, *The use of thermography in detection of metastatic breast cancer.* American Journal of Roentgenology, 1971. **111**(1): p. 148-152.
3. Rontgen, W.C., *On a New Kind of Rays.* Science, 1896. **3**(59): p. 227-31.
4. Brownell, G.L. and W.H. Sweet, *Localization of brain tumors with positron emitters.* Nucleonics, 1953. **11**(11): p. 40-5.
5. Rudin, M. and R. Weissleder, *Molecular imaging in drug discovery and development.* Nat Rev Drug Discov, 2003. **2**(2): p. 123-31.
6. Bushberg, J.T. and J.M. Boone, *The essential physics of medical imaging*. 2011: Lippincott Williams & Wilkins.
7. Weissleder, R. and U. Mahmood, *Molecular imaging.* Radiology, 2001. **219**(2): p. 316-33.
8. Hounsfield, G.N., *Computerized transverse axial scanning (tomography): Part 1. Description of system.* British Journal of Radiology, 1973. **46**(552): p. 1016-1022.
9. Hutton, B.F., *Recent advances in iterative reconstruction for clinical SPECT/PET and CT.* Acta Oncologica, 2011. **50**(6): p. 851-858.
10. Antoch, G., et al., *To enhance or not to enhance? 18F-FDG and CT contrast agents in dual-modality 18F-FDG PET/CT.* J Nucl Med, 2004. **45 Suppl 1**: p. 56S-65S.
11. Caravan, P., et al., *Gadolinium (III) chelates as MRI contrast agents: structure, dynamics, and applications.* Chemical Reviews, 1999. **99**(9): p. 2293-2352.
12. Pacheco-Torres, J., et al., *Environmentally Sensitive Paramagnetic and Diamagnetic Contrast Agents for Nuclear Magnetic Resonance Imaging and Spectroscopy.* Current Topics in Medicinal Chemistry. **11**(1): p. 115-130.
13. Elsinga, P.H. and R.A. Dierckx, *Small Molecule PET-Radiopharmaceuticals.* Curr Pharm Des, 2013.
14. Cai, J. and F. Li, *Single-photon emission computed tomography tracers for predicting and monitoring cancer therapy.* Curr Pharm Biotechnol, 2013. **14**(7): p. 693-707.
15. Thomsen, H.S. and S.K. Morcos, *Radiographic contrast media.* BJU Int, 2000. **86 Suppl 1**: p. 1-10.

16. Pavel, D.G., M. Zimmer, and V.N. Patterson, *In vivo labeling of red blood cells with 99mTc: a new approach to blood pool visualization.* J Nucl Med, 1977. **18**(3): p. 305-8.
17. Hahn, M.A., et al., *Nanoparticles as contrast agents for in-vivo bioimaging: current status and future perspectives.* Analytical and bioanalytical chemistry, 2011. **399**(1): p. 3-27.
18. Lee, S.H., et al., *Paramagnetic inorganic nanoparticles as T MRI contrast agents.* Wiley Interdiscip Rev Nanomed Nanobiotechnol, 2013.
19. Gautier, J., et al., *Design strategies of hybrid metallic nanoparticles for theragnostic applications.* Nanotechnology, 2013. **24**(43): p. 432002.
20. Bloch, F., *Nuclear induction.* Physical review, 1946. **70**(7-8): p. 460.
21. Purcell, E.M., H. Torrey, and R.V. Pound, *Resonance absorption by nuclear magnetic moments in a solid.* Physical review, 1946. **69**(1-2): p. 37.
22. Morris, P.G., *Nuclear Magnetic Resonance Imaging in Medicine and Biology*. 1986: Oxford Science Publications.
23. Stark, D. and W. Bradley, *Magnetic Resonance Imaging*. Inc., Nova Iorque, ed. Mosby. Vol. 1. 1999.
24. Gross, S., et al., *Bioluminescence imaging of myeloperoxidase activity in vivo.* Nat Med, 2009. **15**(4): p. 455-61.
25. Ntziachristos, V., et al., *Looking and listening to light: the evolution of whole-body photonic imaging.* Nat Biotechnol, 2005. **23**(3): p. 313-20.
26. DeChatelet, L.R., et al., *Mechanism of the luminol-dependent chemiluminescence of human neutrophils.* J Immunol, 1982. **129**(4): p. 1589-93.
27. Rose, A.L. and T.D. Waite, *Chemiluminescence of luminol in the presence of iron (II) and oxygen: oxidation mechanism and implications for its analytical use.* Analytical chemistry, 2001. **73**(24): p. 5909-5920.
28. Luker, K.E. and G.D. Luker, *Bioluminescence imaging of reporter mice for studies of infection and inflammation.* Antiviral Res, 2010. **86**(1): p. 93-100.
29. Mauro, C., et al., *The NF-κB transcription factor pathway as a therapeutic target in cancer: methods for detection of NF-κB activity*, in *Inflammation and Cancer*. 2009, Springer. p. 169-207.

30. Carlsen, H., et al., *In vivo imaging of NF-kappa B activity.* J Immunol, 2002. **168**(3): p. 1441-6.
31. Natterer, F., *Computerized tomography*, in *The Mathematics of Computerized Tomography*. 1986, Springer. p. 1-8.
32. Boice Jr, J.D., et al., *Frequent chest X-ray fluoroscopy and breast cancer incidence among tuberculosis patients in Massachusetts.* Radiation research, 1991. **125**(2): p. 214-222.
33. Kubota, K., et al., *Advantage of delayed whole-body FDG-PET imaging for tumour detection.* Eur J Nucl Med, 2001. **28**(6): p. 696-703.
34. Srinivas, M., et al., *Cell tracking using multimodal imaging.* Contrast media & molecular imaging, 2013. **8**(6): p. 432-438.
35. Pimlott, S.L. and A. Sutherland, *Molecular tracers for the PET and SPECT imaging of disease.* Chem Soc Rev, 2011. **40**(1): p. 149-62.
36. Heinle, S.K., et al., *Assessment of myocardial perfusion by harmonic power doppler imaging at rest and during adenosine stress comparison with 99mTc-Sestamibi SPECT imaging.* Circulation, 2000. **102**(1): p. 55-60.
37. Urtasun, R.C., et al., *Measurement of hypoxia in human tumours by non-invasive spect imaging of iodoazomycin arabinoside.* Br J Cancer Suppl, 1996. **27**: p. S209-12.
38. Leitha, T., et al., *Technetium-99m-MIBI in primary and recurrent head and neck tumors: contribution of bone SPECT image fusion.* J Nucl Med, 1998. **39**(7): p. 1166-71.
39. Tharp, K., et al., *Impact of 131I-SPECT/CT images obtained with an integrated system in the follow-up of patients with thyroid carcinoma.* European journal of nuclear medicine and molecular imaging, 2004. **31**(10): p. 1435-1442.
40. Fukuyama, H., et al., *Brain functional activity during gait in normal subjects: a SPECT study.* Neurosci Lett, 1997. **228**(3): p. 183-6.
41. Strauss, L.G., *Fluorine-18 deoxyglucose and false-positive results: a major problem in the diagnostics of oncological patients.* Eur J Nucl Med, 1996. **23**(10): p. 1409-15.
42. Aime, S., et al., *Paramagnetic lanthanide (III) complexes as pH-sensitive chemical exchange saturation transfer (CEST) contrast agents for MRI applications.* Magnetic Resonance in Medicine, 2002. **47**(4): p. 639-648.
43. Hancu, I., et al., *CEST and PARACEST MR contrast agents.* Acta Radiol, 2010. **51**(8): p. 910-23.

44. Sun, P.Z. and A.G. Sorensen, *Imaging pH using the chemical exchange saturation transfer (CEST) MRI: correction of concomitant RF irradiation effects to quantify CEST MRI for chemical exchange rate and pH.* Magnetic Resonance in Medicine, 2008. **60**(2): p. 390-397.
45. McRae, R., et al., *In situ imaging of metals in cells and tissues.* Chem Rev, 2009. **109**(10): p. 4780-827.
46. Zhang, S., C.R. Malloy, and A.D. Sherry, *MRI thermometry based on PARACEST agents.* J Am Chem Soc, 2005. **127**(50): p. 17572-3.
47. Na, H.B., I.C. Song, and T. Hyeon, *Inorganic nanoparticles for MRI contrast agents.* Advanced Materials, 2009. **21**(21): p. 2133-2148.
48. Bonnemain, B., *Superparamagnetic agents in magnetic resonance imaging: physicochemical characteristics and clinical applications. A review.* J Drug Target, 1998. **6**(3): p. 167-74.
49. Liu, F., et al., *Superparamagnetic nanosystems based on iron oxide nanoparticles for biomedical imaging.* Nanomedicine (Lond), 2011. **6**(3): p. 519-28.
50. Frangioni, J.V., *In vivo near-infrared fluorescence imaging.* Curr Opin Chem Biol, 2003. **7**(5): p. 626-34.
51. Weissleder, R., et al., *In vivo imaging of tumors with protease-activated near-infrared fluorescent probes.* Nat Biotechnol, 1999. **17**(4): p. 375-8.
52. Chan, W.C., et al., *Luminescent quantum dots for multiplexed biological detection and imaging.* Curr Opin Biotechnol, 2002. **13**(1): p. 40-6.
53. Yang, M., et al., *Whole-body and intravital optical imaging of angiogenesis in orthotopically implanted tumors.* Proc Natl Acad Sci U S A, 2001. **98**(5): p. 2616-21.
54. Sedghi, S., et al., *Increased production of luminol enhanced chemiluminescence by the inflamed colonic mucosa in patients with ulcerative colitis.* Gut, 1993. **34**(9): p. 1191-7.
55. Barichello, J.M., et al., *Encapsulation of hydrophilic and lipophilic drugs in PLGA nanoparticles by the nanoprecipitation method.* Drug Dev Ind Pharm, 1999. **25**(4): p. 471-6.
56. Grant, C.W., S. Karlik, and E. Florio, *A liposomal MRI contrast agent: Phosphatid ylethanolamine-DTPA.* Magnetic resonance in medicine, 1989. **11**(2): p. 236-243.
57. Mukundan, S., Jr., et al., *A liposomal nanoscale contrast agent for preclinical CT in mice.* AJR Am J Roentgenol, 2006. **186**(2): p. 300-7.

58. Torchilin, V.P., *PEG-based micelles as carriers of contrast agents for different imaging modalities.* Advanced Drug Delivery Reviews, 2002. **54**(2): p. 235-252.
59. Runge, V.M., et al., *Work in progress: potential oral and intravenous paramagnetic NMR contrast agents.* Radiology, 1983. **147**(3): p. 789-91.
60. Comblin, V., et al., *Designing new MRI contrast agents: a coordination chemistry challenge.* Coordination chemistry reviews, 1999. **185**: p. 451-470.
61. Perazella, M.A., *Current status of gadolinium toxicity in patients with kidney disease.* Clin J Am Soc Nephrol, 2009. **4**(2): p. 461-9.
62. Laniado, M. and A. Chachuat, *[The endorem tolerance profile].* Radiologe, 1995. **35**(11 Suppl 2): p. S266-70.
63. Kopp, A.F., et al., *MR imaging of the liver with Resovist: safety, efficacy, and pharmacodynamic properties.* Radiology, 1997. **204**(3): p. 749-56.
64. Okon, E., et al., *Biodegradation of magnetite dextran nanoparticles in the rat. A histologic and biophysical study.* Lab Invest, 1994. **71**(6): p. 895-903.
65. Tartaj, P., et al., *The preparation of magnetic nanoparticles for applications in biomedicine.* Journal of Physics D: Applied Physics, 2003. **36**(13): p. R182.
66. Gupta, A.K. and M. Gupta, *Synthesis and surface engineering of iron oxide nanoparticles for biomedical applications.* Biomaterials, 2005. **26**(18): p. 3995-4021.
67. Rodríguez, E., et al., *In vitro characterization of an Fe8 cluster as potential MRI contrast agent.* NMR in Biomedicine, 2005. **18**(5): p. 300-307.
68. Braun, S., H.-O. Kalinowski, and S. Berger, *100 and more basic NMR experiments*. 1996: VCH Weinheim.
69. Mosmann, T., *Rapid colorimetric assay for cellular growth and survival: application to proliferation and cytotoxicity assays.* J Immunol Methods, 1983. **65**(1-2): p. 55-63.
70. Weissleder, R., et al., *Superparamagnetic iron oxide: pharmacokinetics and toxicity.* AJR Am J Roentgenol, 1989. **152**(1): p. 167-73.
71. Pouliquen, D., et al., *Iron oxide nanoparticles for use as an MRI contrast agent: pharmacokinetics and metabolism.* Magnetic resonance imaging, 1991. **9**(3): p. 275-283.

72. Villringer, A., et al., *Dynamic imaging with lanthanide chelates in normal brain: contrast due to magnetic susceptibility effects.* Magnetic resonance in medicine, 1988. **6**(2): p. 164-174.
73. Rosen, B.R., J.W. Belliveau, and D. Chien, *Perfusion imaging by nuclear magnetic resonance.* Magn Reson Q, 1989. **5**(4): p. 263-81.
74. Rosen, B.R., et al., *Perfusion imaging with NMR contrast agents.* Magnetic Resonance in Medicine, 1990. **14**(2): p. 249-265.
75. Barth, R.F., *Rat brain tumor models in experimental neuro-oncology: the 9L, C6, T9, F98, RG2 (D74), RT-2 and CNS-1 gliomas.* J Neurooncol, 1998. **36**(1): p. 91-102.
76. Wang, Y.X., *Superparamagnetic iron oxide based MRI contrast agents: Current status of clinical application.* Quant Imaging Med Surg, 2011. **1**(1): p. 35-40.
77. Wang, Y.X., S.M. Hussain, and G.P. Krestin, *Superparamagnetic iron oxide contrast agents: physicochemical characteristics and applications in MR imaging.* Eur Radiol, 2001. **11**(11): p. 2319-31.
78. Calle, D., S. Cerdán, and F. Moreno, *Superparamagnetic Nanoparticles as a Contrast Agent for Magnetic Resonance Imaging (MRI) of Magnetic Susceptibility (T2*)*. 2013, PCT/ES2012/070044, WO 2013/110828.
79. Libby, P., P.M. Ridker, and A. Maseri, *Inflammation and atherosclerosis.* Circulation, 2002. **105**(9): p. 1135-43.
80. McGeer, P.L. and E.G. McGeer, *The inflammatory response system of brain: implications for therapy of Alzheimer and other neurodegenerative diseases.* Brain Res Brain Res Rev, 1995. **21**(2): p. 195-218.
81. Wellen, K.E. and G.S. Hotamisligil, *Inflammation, stress, and diabetes.* J Clin Invest, 2005. **115**(5): p. 1111-9.
82. Williams, C.S., M. Mann, and R.N. DuBois, *The role of cyclooxygenases in inflammation, cancer, and development.* Oncogene, 1999. **18**(55): p. 7908-16.
83. Brambilla, R., et al., *Inhibition of astroglial nuclear factor kappaB reduces inflammation and improves functional recovery after spinal cord injury.* J Exp Med, 2005. **202**(1): p. 145-56.
84. Meade, E.A., W.L. Smith, and D.L. DeWitt, *Differential inhibition of prostaglandin endoperoxide synthase (cyclooxygenase) isozymes by aspirin and other non-steroidal anti-inflammatory drugs.* J Biol Chem, 1993. **268**(9): p. 6610-4.

85. Henry, D., et al., *Variability in risk of gastrointestinal complications with individual non-steroidal anti-inflammatory drugs: results of a collaborative meta-analysis.* BMJ, 1996. **312**(7046): p. 1563-6.
86. Lian, T. and R.J. Ho, *Trends and developments in liposome drug delivery systems.* J Pharm Sci, 2001. **90**(6): p. 667-80.
87. Torchilin, V.P., *Recent advances with liposomes as pharmaceutical carriers.* Nature Reviews Drug Discovery, 2005. **4**(2): p. 145-160.
88. Hilgenbrink, A.R. and P.S. Low, *Folate receptor-mediated drug targeting: from therapeutics to diagnostics.* J Pharm Sci, 2005. **94**(10): p. 2135-46.
89. Danhier, F., O. Feron, and V. Preat, *To exploit the tumor microenvironment: Passive and active tumor targeting of nanocarriers for anti-cancer drug delivery.* J Control Release, 2010. **148**(2): p. 135-46.
90. Lammers, T., et al., *Nanotheranostics and image-guided drug delivery: current concepts and future directions.* Mol Pharm, 2010. **7**(6): p. 1899-912.
91. Simopoulos, A.P., *Omega-3 fatty acids in health and disease and in growth and development.* Am J Clin Nutr, 1991. **54**(3): p. 438-63.
92. Calder, P.C., *n-3 polyunsaturated fatty acids, inflammation, and inflammatory diseases.* Am J Clin Nutr, 2006. **83**(6 Suppl): p. 1505S-1519S.
93. Mori, T.A. and L.J. Beilin, *Omega-3 fatty acids and inflammation.* Curr Atheroscler Rep, 2004. **6**(6): p. 461-7.
94. Simopoulos, A.P., *Omega-3 fatty acids in inflammation and autoimmune diseases.* Journal of the American College of Nutrition, 2002. **21**(6): p. 495-505.
95. Langman, M.J., et al., *Risks of bleeding peptic ulcer associated with individual non-steroidal anti-inflammatory drugs.* Lancet, 1994. **343**(8905): p. 1075-8.
96. Torchilin, V.P. and V. Weissig, *Liposomes: a practical approach*. Vol. 264. 2003: Oxford University Press.
97. Bibi, S., et al., *Microscopy imaging of liposomes: from coverslips to environmental SEM.* Int J Pharm. **417**(1-2): p. 138-50.
98. Berne, B.J., *Dynamic light scattering: with applications to chemistry, biology and physics*. 1976: DoverPublications. com.

99. Hallett, F.R., J. Watton, and P. Krygsman, *Vesicle sizing: Number distributions by dynamic light scattering.* Biophys J, 1991. **59**(2): p. 357-62.
100. Lee, H., et al., *Synthesis, characterization, and in vivo diagnostic applications of hyaluronic acid immobilized gold nanoprobes.* Biomaterials, 2008. **29**(35): p. 4709-18.
101. Camuesco, D., et al., *Dietary olive oil supplemented with fish oil, rich in EPA and DHA (n-3) polyunsaturated fatty acids, attenuates colonic inflammation in rats with DSS-induced colitis.* J Nutr, 2005. **135**(4): p. 687-94.
102. Winking, M., et al., *Boswellic acids inhibit glioma growth: a new treatment option?* J Neurooncol, 2000. **46**(2): p. 97-103.
103. Willker, W. and D. Leibfritz, *Assignment of mono-and polyunsaturated fatty acids in lipids of tissues and body fluids.* Magnetic resonance in chemistry, 1998. **36**(S79): p. S84.
104. Griffin, J.L., et al., *Assignment of 1H nuclear magnetic resonance visible polyunsaturated fatty acids in BT4C gliomas undergoing ganciclovir-thymidine kinase gene therapy-induced programmed cell death.* Cancer Res, 2003. **63**(12): p. 3195-201.
105. Grelard, A., et al., *NMR spectroscopy of lipid bilayers.* Methods Mol Biol, 2010. **654**: p. 341-59.
106. Pelta, M.D., et al., *Pulse sequences for high-resolution diffusion-ordered spectroscopy (HR-DOSY).* Magnetic resonance in chemistry, 1998. **36**(10): p. 706-714.
107. Einstein, A., *Über die von der molekularkinetischen Theorie der Wärme geforderte Bewegung von in ruhenden Flüssigkeiten suspendierten Teilchen.* Annalen der physik, 1905. **322**(8): p. 549-560.
108. Merbach, A.E., L. Helm, and É. Tóth, *The Chemistry of Contrast Agents in Medical Magnetic Resonance Imaging*. 2013: Wiley Online Library.
109. Solomon, I., *Relaxation processes in a system of two spins.* Physical Review, 1955. **99**(2): p. 559.
110. Bloembergen, N., *Proton relaxation times in paramagnetic solutions.* The Journal of Chemical Physics, 1957. **27**: p. 572.
111. Bloembergen, N. and L. Morgan, *Proton relaxation times in paramagnetic solutions. Effects of electron spin relaxation.* The Journal of Chemical Physics, 1961. **34**: p. 842.

112. Schrooyen, P.M., R. van der Meer, and C.G. De Kruif, *Microencapsulation: its application in nutrition.* Proc Nutr Soc, 2001. **60**(4): p. 475-9.
113. Holser, R., *Encapsulation of Polyunsaturated Fatty Acid Esters with Solid Lipid Particles.* Lipid Insights, 2011. **5**(LPI-Encapsulation-of-Polyunsaturated-Fatty-Acid-Esters-with-Solid-Lipid2): p. 1-5.
114. Calle, D., S. Cerdán , and F. Moreno, *Composiciones que contienen liposomas, ácidos grasos poliinsaturados omega-3 de cadena larga y nanopartículas superparamagnéticas y su uso en el tratamiento de tumores malignos*. 2014, P201430035.
115. Iijima, S., *Helical microtubules of graphitic carbon.* Nature, 1991. **354**(6348): p. 56-58.
116. O'connell, M.J., *Carbon nanotubes: properties and applications*. 2006: CRC press.
117. Jorio, A., G. Dresselhaus, and M.S. Dresselhaus, *Carbon nanotubes: advanced topics in the synthesis, structure, properties and applications*. Vol. 111. 2008: Springer.
118. Ebbesen, T., et al., *Electrical conductivity of individual carbon nanotubes.* Nature, 1996. **382**(6586): p. 54-56.
119. Ajiki, H. and T. Ando, *Aharonov-Bohm effect in carbon nanotubes.* Physica B: Condensed Matter, 1994. **201**: p. 349-352.
120. Damnjanović, M., et al., *Full symmetry, optical activity, and potentials of single-wall and multiwall nanotubes.* Physical Review B, 1999. **60**(4): p. 2728-2739.
121. Berber, S., Y.-K. Kwon, and D. Tomanek, *Unusually high thermal conductivity of carbon nanotubes.* Physical Review Letters, 2000. **84**(20): p. 4613-4616.
122. Iijima, S., et al., *Structural flexibility of carbon nanotubes.* The Journal of chemical physics, 1996. **104**: p. 2089.
123. Ruoff, R.S. and D.C. Lorents, *Mechanical and thermal properties of carbon nanotubes.* Carbon, 1995. **33**(7): p. 925-930.
124. Lu, J.P., *Elastic Properties of Carbon Nanotubes and Nanoropes.* Physical Review Letters, 1997. **79**(7): p. 1297-1300.
125. Searles, T., et al., *Large anisotropy in the magnetic susceptibility of metallic carbon nanotubes.* Physical Review Letters, 2010. **105**(1): p. 017403.
126. Tian, W. and S. Datta, *Aharonov-Bohm-type effect in graphene tubules: A Landauer approach.* Physical Review B, 1994. **49**(7): p. 5097.

127. Nemec, N. and G. Cuniberti, *Hofstadter butterflies of bilayer graphene.* Physical Review B, 2007. **75**(20): p. 201404.
128. Lu, J.P., *Novel magnetic properties of carbon nanotubes.* Physical Review Letters, 1995. **74**(7): p. 1123-1126.
129. Roche, S., et al., *Aharonov-Bohm spectral features and coherence lengths in carbon nanotubes.* Physical Review B, 2000. **62**(23): p. 16092.
130. Fujiwara, M., et al., *Magnetic orientation and magnetic properties of a single carbon nanotube.* The Journal of physical chemistry A, 2001. **105**(18): p. 4383-4386.
131. Marques, M.A., M. d'Avezac, and F. Mauri, *Magnetic response and NMR spectra of carbon nanotubes from ab initio calculations.* Physical Review B, 2006. **73**(12): p. 125433.
132. Patzke, G.R., F. Krumeich, and R. Nesper, *Oxidic nanotubes and nanorodsâ€"anisotropic modules for a future nanotechnology.* Angewandte Chemie International Edition, 2002. **41**(14): p. 2446-2461.
133. Zaric, S., et al., *Estimation of magnetic susceptibility anisotropy of carbon nanotubes using magnetophotoluminescence.* Nano Letters, 2004. **4**(11): p. 2219-2221.
134. Le Bihan, D., et al., *Diffusion tensor imaging: concepts and applications.* J Magn Reson Imaging, 2001. **13**(4): p. 534-46.
135. Negri, V., et al., *Nanotubular paramagnetic probes as contrast agents for magnetic resonance imaging based on the diffusion tensor.* Angewandte Chemie, 2010. **122**(10): p. 1857-1859.
136. Cerpa, A., et al., *Single-Walled Carbon Nanotubes as Anisotropic Relaxation Probes for Magnetic Resonance Imaging.* MedChemComm, 2013.
137. Wu, C., et al., *Removal of ferromagnetic metals for the large-scale purification of single-walled carbon nanotubes.* The Journal of Physical Chemistry C, 2009. **113**(9): p. 3612-3616.
138. Samorì, C., et al., *Potentiometric titration as a straightforward method to assess the number of functional groups on shortened carbon nanotubes.* Carbon, 2010. **48**(9): p. 2447-2454.
139. Liu, J., et al., *Fullerene pipes.* Science, 1998. **280**(5367): p. 1253-1256.
140. Li, S., et al., *Adsorption of carbon nanotubes on active carbon microparticles.* Carbon, 2008. **46**(7): p. 1091-1095.

141. Cosnier, S. and M. Holzinger, *Design of carbon nanotube-polymer frameworks by electropolymerization of SWCNT-pyrrole derivatives.* Electrochimica Acta, 2008. **53**(11): p. 3948-3954.
142. Peng, D.L., et al., *Magnetic properties of Fe clusters adhering to single-wall carbon nanotubes.* Journal of Magnetism and Magnetic Materials, 2005. **292**(0): p. 143-149.
143. Belyanskaya, L., et al., *The reliability and limits of the MTT reduction assay for carbon nanotubes–cell interaction.* Carbon, 2007. **45**(13): p. 2643-2648.
144. Saeva, F.D., *The optical properties of anisotropically ordered solutes in cholesteric liquid crystalline mesophases.* Pure and Applied Chemistry, 1974. **38**(1-2): p. 25-36.
145. Leyton, P., et al., *Carbon nanotube bundles as molecular assemblies for the detection of polycyclic aromatic hydrocarbons: surface-enhanced resonance Raman spectroscopy and theoretical studies.* J Phys Chem B, 2006. **110**(13): p. 6470-4.
146. Walker, M.M., et al., *Structure and function of the vertebrate magnetic sense.* Nature, 1997. **390**(6658): p. 371-6.
147. Worle-Knirsch, J.M., K. Pulskamp, and H.F. Krug, *Oops they did it again! Carbon nanotubes hoax scientists in viability assays.* Nano Lett, 2006. **6**(6): p. 1261-8.
148. Ballesteros García, P., V. Negri, and D. Calle, *Compuestos y composiciones que comprenden nanotubos de carbono y compuestos de fórmula (I) y su uso como agentes de contraste.* 2014, P201400058.